

# SPIDER - IV. Optical and NIR color gradients in Early-type galaxies: New Insights into Correlations with Galaxy Properties

La Barbera, F.<sup>1</sup>, de Carvalho, R.R.<sup>2</sup>, de la Rosa, I.G.<sup>3,4</sup>, Gal, R.R.<sup>5</sup>, Swindle, R.<sup>5</sup>, Lopes, P.A.A.<sup>6</sup>

<sup>(1)</sup>*INAF – Osservatorio Astronomico di Capodimonte, Napoli, Italy*

<sup>(2)</sup>*Instituto Nacional de Pesquisas Espaciais/MCT, S. J. dos Campos, Brazil*

<sup>(3)</sup>*Instituto de Astrofisica de Canarias (IAC), E-38200 La Laguna, Tenerife, Spain*

<sup>(4)</sup>*Depto. de Astrofisica, Universidad de La Laguna (ULL), E-38206 La Laguna, Tenerife, Spain*

<sup>(5)</sup>*University of Hawai'i, Institute for Astronomy, 2680 Woodlawn Drive, Honolulu, HI 96822, USA*

<sup>(6)</sup>*Observatório do Valongo/UFRJ, Rio de Janeiro, Brazil*

## ABSTRACT

We present an analysis of stellar population gradients in 4,546 Early-Type Galaxies (ETGs) with photometry in *grizYHJK* along with optical spectroscopy. ETGs were selected as bulge-dominated systems, displaying passive spectra within the SDSS fibers. A new approach is described which utilizes color information to constrain age and metallicity gradients. Defining an effective color gradient,  $\nabla_{\star}$ , which incorporates all of the available color indices, we investigate how  $\nabla_{\star}$  varies with galaxy mass proxies, i.e. velocity dispersion, stellar ( $M_{\star}$ ) and dynamical ( $M_{\text{dyn}}$ ) masses, as well as age, metallicity, and  $[\alpha/\text{Fe}]$ . ETGs with  $M_{\text{dyn}}$  larger than  $8.5 \times 10^{10} M_{\odot}$  have increasing age gradients and decreasing metallicity gradients *wrt* mass, metallicity, and enhancement. We find that velocity dispersion and  $[\alpha/\text{Fe}]$  are the main drivers of these correlations. ETGs with  $2.5 \times 10^{10} M_{\odot} \leq M_{\text{dyn}} \leq 8.5 \times 10^{10} M_{\odot}$ , show no correlation of age, metallicity, and color gradients *wrt* mass, although color gradients still correlate with stellar population parameters, and these correlations are independent of each other. In both mass regimes, the striking anti-correlation between color gradient and  $\alpha$ -enhancement is significant at  $\sim 5 \sigma$ , and results from the fact that metallicity gradient decreases with  $[\alpha/\text{Fe}]$ . This anti-correlation may reflect the fact that star formation and metallicity enrichment are regulated by the interplay between the energy input from supernovae, and the temperature and pressure of the hot X-ray gas in ETGs. For all mass ranges, positive age gradients are associated with old galaxies ( $> 5 - 7$  Gyr). For galaxies younger than  $\sim 5$  Gyr, mostly at low-mass, the age gradient tends to be anti-correlated with the Age parameter, with more positive gradients at younger ages.

*Subject headings:* Galaxies: formation – Galaxies: evolution – Galaxies: fundamental parameters

## 1. Introduction

The study of the stellar population in galaxies presents some unique challenges. First, the method used to characterize a stellar population is crucial as it provides constraints on theories of galaxy formation (e.g. De Lucia et al. 2006). Second, age and metallicity dominated indicators should minimize the age-metallicity degeneracy described in the 3/2 Worthey law (Worthey, Trager & Faber 1995). Finally, a galaxy’s environment may be the dominant influence on its star formation history, further reducing the adequacy of the Single Stellar Population (SSP) assumption. Monolithic collapse models predict early-type systems with a central region that is more metal rich, slightly younger, and less  $\alpha/F_e$  enhanced than the outer parts. Mergers may wash out any possible gradient present in the progenitors, although dissipation can trigger star formation in the cores of galaxies, creating age gradients. It is important to emphasize that we still lack firm quantitative estimates for many of these effects (White 1980). Considering the impact of such predictions, we need large and well characterized samples to tackle this issue. The nearby universe ( $z < 0.1$ ) provides a starting point, as we now have high quality data for large numbers of galaxies.

The study of color gradients is motivated by the possibility of discriminating between different models of galaxy formation, and points to the real need for systematic and accurate measurements for a large and well controlled sample of ETGs. These systems become gradually bluer in the outskirts (e.g. Peletier et al. 1990; Goudfrooij et al. 1994; Michard 1999; Wu et al. 2005; Cantiello et al. 2005; Suh et al. 2010). Although the age-metallicity degeneracy makes the interpretation of the color gradient troublesome, metallicity gradient seems to be main cause (e.g. Saglia et al. 2000; Tamura et al. 2000; Tamura & Ohta 2000; La Barbera et al. 2003). Small, positive age gradients are also consistent with observations (e.g. Saglia et al. 2000), and have been detected in the low-redshift population of ETGs (La Barbera & de Carvalho 2009; Clemens et al. 2009). Positive color gradients in high-redshift ETGs have been observed by Ferreras et al. (2005), who found that about one-third of field ETGs at  $z \sim 0.7$  have blue cores, in contrast to only 10% at lower redshift (see also Menanteau et al. 2001, 2004; Ferreras et al. 2009). The possibility that color gradients could be due merely to dust in a well mixed stellar population has been considered (e.g. Goudfrooij & de Jong 1995) but many ETGs exhibit radial gradients of metal absorption features, which cannot be attributed to dust (e.g. Gonzalez 1993; Mehlert et al. 2000). Furthermore, many ETGs are undetected by IRAS at 60  $\mu$  and 100  $\mu$ . Cosmological simulations do not yet have sufficient spatial resolution to provide reliable color gradients. However, chemo-dynamical simulations of ETGs are starting to yield meaningful results for metallicity gradients, reproducing some observed

population gradients (see Kobayashi 2004).

The last decade has witnessed the appearance of important observational studies using photometric and spectroscopic data to constrain age, metallicity and elemental abundances (Jørgensen 1999; Poggianti et al. 2001a; Terlevich & Forbes 2002; Trager et al. 2000). They conclude that age and metallicity are anti-correlated for galaxies of a given luminosity. Furthermore, Poggianti et al. (2001b) find that in high density regimes a large fraction of systems shows no signs of star formation in their centers. Another important finding relating star formation and environment comes from the work of Kuntschner et al. (2002) who analyzed a sample of early-type systems in the low density regime (field) showing that these galaxies are younger and more metal-rich than their counterparts in clusters. Most of these studies used samples of at most a few hundred galaxies. Since these works are the nearby counterparts of the studies of the evolution of early-type galaxies (ETGs) as a function of redshift in clusters (e.g. van Dokkum & Stanford 2003) and in low-density environments (Treu et al. 1999), it is necessary to establish large and well-defined samples covering a broad range of environments as we do here.

This is the fourth paper of a series studying the global properties of ETGs in the local Universe ( $z < 0.1$ ). We focus on stellar population gradients and how they depend on galaxy properties. We use optical data (*griz* photometry and spectra) from the Sloan Digital Sky Survey Data Release 6 (SDSS, Adelman-McCarthy et al. 2008) and near-infrared photometry from the UKIRT Infrared Deep Sky Survey Data Release Four (UKIDSS, Lawrence et al. 2007). The selection of ETGs is described in La Barbera et al. (2010a; hereafter Paper I), and we refer the reader to that paper for all the details on sample selection and the procedures used to derive the galaxy parameters. The results presented in this paper apply not only to ellipticals, but also to lenticular galaxies as well as those dominated by a red central bulge (but see Sec. 3.3 and Sec. 8.3).

This paper is organized as follows: Sec. 2 briefly describes the sample used while in Sec. 3 we present how stellar and dynamical masses were computed and stellar population properties measured. Measurement of color gradients are described in Sec. 4, while their distributions are discussed in Sec. 5. Sec 6 details how we derive stellar population gradients from color gradients. Sec. 7 presents our approach to constrain the variation of stellar population parameters, and discusses the systematics involved. Sec. 8 illustrates the dependence of the effective color gradient on galaxy parameters and Sec. 9 examines the age versus metallicity gradients in ETGs. Finally, in Sec. 10 we summarize our most important results. Throughout the paper, we adopt a cosmology with  $H_0 = 75 \text{ km s}^{-1} \text{ Mpc}^{-1}$ ,  $\Omega_m = 0.3$ , and  $\Omega_\Lambda = 0.7$ .

## 2. The sample

The sample of ETGs is selected from SDSS-DR6, following the procedure described in La Barbera et al. (2008b), La Barbera & de Carvalho (2009), and Paper I. We select galaxies in the redshift range of 0.05 to 0.095, with  $^{0.1}M_r < -20$ , where  $^{0.1}M_r$  is the k-corrected SDSS Petrosian magnitude in r-band. The k-correction is determined using the software *kcorrect* (version 4.1.4; Blanton et al. 2003a), through a restframe r-band filter blue-shifted by a factor  $(1 + z_0)$ . We adopt  $z_0 = 0.1$  as in (e.g.) Hogg et al. 2004. The lower redshift limit of the sample is chosen to minimize the aperture bias (Gómez et al. 2003), while the upper redshift limit guarantees not only a high level of completeness (according to Sorrentino et al. 2006), but also allows us to define a volume-limited sample of *bright* early-type systems. At the upper redshift limit of  $z = 0.095$ , the magnitude cut of  $-20$  also corresponds approximately to the magnitude limit to which the SDSS spectroscopy is complete (i.e. a Petrosian magnitude of  $m_r \sim 17.8$ ). Following Bernardi et al. (2003), we define ETGs using the SDSS spectroscopic parameter *eClass*, which indicates the spectral type of a galaxy on the basis of a principal component analysis, and the SDSS photometric parameter *fracDev<sub>r</sub>*, which measures the fraction of the galaxy light that is better fitted by a de Vaucouleurs (rather than an exponential) law. ETGs are those systems with *eClass* < 0 and *fracDev<sub>r</sub>* > 0.8. We select only galaxies with central velocity dispersion,  $\sigma_0$ , available from SDSS-DR6, in the range of 70 and 420 km s<sup>-1</sup>, and with no spectroscopic warning on (i.e. *zWarning* attribute set to zero). These constraints are chosen to select only reliable velocity dispersion measurements from SDSS. Applying the above criteria leads to a sample of 39,993 ETGs.

Out of the 39,993 ETGs defining the SPIDER sample, 5,080 also have photometry in the *YJHK* wavebands from the UKIDSS-Large Area Survey (see Paper I). All galaxies have two measures of the central velocity dispersion, one from SDSS-DR6 and an alternate estimate obtained by fitting SDSS spectra with the STARLIGHT software (Cid Fernandes et al. 2005). In all wavebands, the structural parameters including effective radius,  $r_e$ , the mean surface brightness within that radius,  $\langle \mu \rangle_e$ , and the Sersic index,  $n$ , have been homogeneously measured using 2DPHOT (La Barbera et al. 2008a). Total magnitudes are computed from the effective parameters in each filter.

For this work, we select ETGs from the SPIDER survey as follows. First, we exclude galaxies which are poorly fitted by a two-dimensional Sersic model. This is done by selecting only objects with  $\chi^2 < 2$  in all wavebands, where  $\chi^2$  is the rms of residuals between the galaxy image in a given band and the corresponding best-fitting two-dimensional Sersic model. The threshold  $\chi^2 = 2$  excludes those objects which are more than  $5\sigma$  above the peak of the  $\chi^2$  distribution in all passbands. As shown in Paper I, the distributions of  $\chi^2$  in *grizYJHK* are peaked around one, with a width of  $\sim 0.2$ . Second, since we estimate the internal color gradients from  $r_e$  and  $n$ , we exclude galaxies with large uncertainties on these parameters. As shown in Paper I, the errors on  $n$  are

nearly independent of  $S/N$  ratio, and are always less than  $\sim 0.2$  dex. On the other hand, the errors on  $r_e$  strongly depend on the  $S/N$ . To remove galaxies with large uncertainties without overly reducing the sample size, we select only those ETGs with a  $\log r_e$  uncertainty less than 0.5 dex in all wavebands. These restrictions yield a subsample of 37,068 galaxies with parameters in *griz*. Of these, 4,546 objects also have photometry in *YJHK*. Hereafter, we refer to these as the optical and optical+NIR samples of ETGs, respectively.

### 3. Galaxy parameters

We analyze the dependence of internal color gradients in ETGs on galaxy parameters, i.e. structural parameters, optical and NIR magnitudes, stellar and dynamical masses, and stellar population properties (age, metallicity, and  $\alpha$ -enhancement). The derivation of magnitudes and structural parameters is described in Paper I. Below, we describe the estimate of stellar and dynamical masses (Sec. 3.1 and 3.2), as well as that of the stellar population parameters (Sec. 3.3).

#### 3.1. Stellar masses from SED fitting

Galaxy stellar masses can be estimated by fitting their observed SEDs with stellar population synthesis models. Brinchmann & Ellis (2000) demonstrated that such techniques, combining optical and near-IR fluxes with spectroscopic redshifts, could be used to derive masses with a factor of two uncertainty to  $z \sim 1$ . Local studies by Bell et al. (2003) and Cole et al. (2001) examined the stellar mass function using similar methods. Salim et al. (2005, 2007) have shown that galaxy properties derived from SED fitting with broadband colors are consistent with those derived from spectroscopic data. Thus, we use SED fitting to derive galaxy stellar masses.

We employ the LePhare code (S. Arnouts & O. Ilbert) used by the COSMOS survey (Ilbert et al. 2009) to fit a suite of Bruzual & Charlot (2003, hereafter BC03) model SEDs to our observed 8-band photometry and the known spectroscopic redshift. LePhare performs a  $\chi^2$  minimization between the observed fluxes (and their associated errors) and those synthesized from the models. Because early-types are unlikely to have significant ongoing star formation, we use a simple set of Bruzual & Charlot (2003) SEDs, with 6 different star-formation e-folding times  $\tau$ , 5 internal reddenings  $E(B - V)$ , and four metallicities  $Z/Z_\odot$ , for a total of 120 possible models. The values of these parameters are given in Tab. 1. We assume a Calzetti et al. (2000) extinction law and Chabrier (2003) initial mass function. The reddening  $E(B-V)$  is limited to 0.5 magnitudes to avoid incorrect fitting of observationally red galaxies as highly reddened blue galaxies; such objects should be absent from our sample. Because each BC03 template is normalized to one solar mass, we use the

observed  $K$ -band flux to determine the normalization of the best-fit template which then gives the stellar mass. We use  $K$ -band for the mass scaling since it is only weakly affected by dust extinction and is quite insensitive to the presence of young, luminous stars (Kauffmann & Charlot 1998; Bundy et al. 2005).

Galaxy fluxes are estimated in an adaptive aperture of radius  $3 \times r_{K,i}$  in all wavebands, where  $r_{K,i}$  is the  $i$ -band Kron radius (see Paper I). We use these aperture fluxes as they have a better accuracy than those obtained from (2DPHOT) total magnitudes. In order to derive total stellar masses,  $M_*$ , we apply an aperture correction. We calculate the fraction of total to  $3 \times r_{K,i}$  aperture flux in  $K$ -band, and then multiply the estimated stellar mass by this fraction. This procedure assumes that stellar mass in a galaxy is distributed in the same way as the  $K$ -band light.

Rather than use an individual best-fitting SED (based on the  $\chi^2$ ), we use a mass computed from the model corresponding to the median  $e^{-\chi^2/2}$ . This reduces stochastic mass errors due to individual models which happen to have very low  $\chi^2$  values, since there remains some degeneracy in the SED fits even with 8 filters. A small number of galaxies (1465 of 39993 with optical data only, and 286 of 4546 with NIR data) are not well fit by any of the SEDs, resulting in  $e^{-\chi^2/2} = 0$  and thus no stellar mass estimate. These objects, comprising 3.6% and 6.3% of the optical and optical+NIR samples, respectively, are excluded from analyzes that require the stellar masses.

We tested our stellar masses by comparing to those derived by a group at Max Planck using SDSS photometry alone.<sup>1</sup> The overall agreement is excellent. We find a modest offset in  $M_{*,SPIDER} - M_{*,MPI}$  of 0.14 dex; this is because we use Kron magnitudes rather than fiber magnitudes; Kron magnitudes are  $\sim 0.5$  mag brighter, which translates into a difference  $\sim 0.2$  in  $\log(M)$ . The *rms* scatter between the two mass estimators is only 0.1 dex, a factor of  $\sim 2$  smaller than most systematic errors and biases introduced by different choices of IMF, extinction law, etc. More details of the SED fitting and potential sources of errors and biases in the stellar mass estimates will

---

<sup>1</sup>These mass estimates can be found at <http://www.mpa-garching.mpg.de/SDSS/DR7/Data/stellarmass.html>.

Table 1. BC03 Galaxy SED Parameters

$\tau$ (Gyr)	$E(B - V)$	$Z/Z_\odot$
1	0	0.2
2	0.1	0.4
3	0.2	1.0
5	0.3	3.0
10	0.4	
15	0.5	

be presented in an upcoming paper in this series devoted to this issue alone (Swindle et al. 2010, in preparation).

We note that both the SED fitting and the analysis of color gradients (Sec. 7) are performed with a different set of models (i.e. BC03) than that used for the spectral analysis (i.e. MILES, see Sec. 3.3). The BC03 models provide a high resolution of 1 Å in the wavelength range 3322 Å to 9300 Å (griz), with a median resolution of 10 Å in zYJHK. We do not use the MILES library here as we do for other tests in this paper due to its limited wavelength coverage (3525 Å to 7500 Å). With 7500 Å lying near the central wavelength of the i-band, ignoring the izYJHK data inevitably yields failures in SED identification, provided the range of model parameters given in Tab. 1. This uncertainty, coupled with the benefit of the K-band flux for mass-scaling, motivates this choice of models for the SED fitting. The technical justification for using the MILES library in analyzing spectra and color gradients is also detailed in Sec. 3.3.

### 3.2. Dynamical masses

Dynamical masses,  $M_{dyn}$ , are obtained from galaxy effective radii and velocity dispersions. Applying the virial theorem, we write

$$M_{dyn} = A \times \sigma_0^2 r_{e,K} \quad (1)$$

where  $r_{e,K}$  is the effective radius in K-band, and  $A$  is a scale factor that accounts for the internal structure of ETGs. Most previous works estimated  $A$  by assuming a single universal model for the light distribution in ETGs, such as the King model (Jørgensen et al. 1996). However, this does not account for the variety of ETG light profile shapes (e.g. Caon, Capaccioli, & D’Onofrio 1993), as parametrized by the Sersic index. To account for this, following a similar procedure to that of D’Onofrio et al. (2008), we estimate  $A$  using de-projected Sersic galaxy models. The models and the de-projection procedure are detailed in Coppola, La Barbera, Capaccioli (2009). The models describe spherical, non-rotating, isotropic galactic systems. We also assume that the spatial distribution of dark matter follows that of the stellar component. Under these assumptions, each model consists of a single Sersic component characterized by three parameters: the half-mass radius, the total mass, and the Sersic index (see Coppola, La Barbera, Capaccioli (2009) for details). The use of more complex models (i.e. those with two-components) is well beyond the scope of this paper, and we postpone it to a forthcoming contribution. For each ETG, we construct the corresponding Sersic model, using the effective radius and Sersic index of the galaxy in K-band. We estimate  $A$  by computing the ratio of the quantities  $M_{dyn}$  and  $\sigma_0^2 \times r_{e,K}$  for the given model. We compute  $\sigma_0$  by projecting the model in two-dimensions, within a circular aperture of radius 1.5'', i.e. the same aperture as the SDSS fibers. Since we do not have K-band structural

parameters for the optical sample of ETGs,  $M_{dyn}$  is only estimated for galaxies in the optical+NIR sample. Fig. 1 shows the dynamical masses versus the Petrosian magnitudes, from which we see that our limiting magnitude corresponds to a lower mass limit of  $\sim 3 \times 10^{10} M_{\odot}$ .

### 3.3. Stellar population properties

As described in Paper I, we have re-measured velocity dispersions for ETGs in the SPIDER sample using STARLIGHT (Cid Fernandes et al. 2005). This software determines the linear combination of Simple Stellar Population (SSP) models which, broadened with a given  $\sigma$ , best matches the observed galaxy spectrum. Hereafter, we refer to the set of SSP models provided as input to STARLIGHT as the *SSP basis*, and to the output linear combination of SSPs as the synthetic spectrum. For the purpose of remeasuring the  $\sigma_0$ 's, we run STARLIGHT with a *basis* of SSPs from the MILES galaxy spectral library (Vazdekis et al. 2010), covering a wide range of ages and metallicities, but with fixed solar abundance ratio ( $[\alpha/Fe]=0$ ).

Here we also use STARLIGHT to estimate the *Age*,  $[Z/H]$ , and  $[\alpha/Fe]$  of each ETG. In contrast to the more common practice of using index-index diagrams to estimate SSP-equivalent stellar population parameters <sup>2</sup>, STARLIGHT uses all of the information present in the data, by fitting a set of SSP models to the entire galaxy spectrum. A detailed comparison of stellar population parameter estimates from different techniques for the SPIDER sample is currently under way, and will be the subject of a forthcoming paper in this series. Here, we provide only the essential information on how we use STARLIGHT to derive *Age*,  $[Z/H]$ , and  $[\alpha/Fe]$ . For each galaxy, we run STARLIGHT using the alpha-enhanced MILES (hereafter  $\alpha$ -MILES) spectral library (Cervantes et. al. 2007). As detailed in App. A, the  $\alpha$ -MILES library extends the MILES galaxy spectral library to SSP models with non-solar abundance ratios, in the  $[\alpha/Fe]$  range of  $-0.2$  to  $+0.6$ , allowing the spectra of ETGs to be modeled with better accuracy than that achieved with solar-abundance MILES models. The  $\alpha$ -MILES SEDs cover the same spectral range ( $3525 - 7500 \text{ \AA}$ ), with the same spectral resolution ( $2.3 \text{ \AA}$ ), as the (solar abundance) MILES library. Hence, they are well suited to analyzing SDSS spectra, whose spectral resolution is  $\sim 2.36 \text{ \AA}$  FWHM, in the wavelength interval  $4800\text{--}5350 \text{ \AA}$ . To run STARLIGHT, we select a *basis* of 176  $\alpha$ -MILES SSPs, with ages ranging from 1 to  $\sim 14$  Gyr in eleven steps, metallicities of  $[Z/H] = -0.68, -0.38, 0., 0.2$ , and enhancements of  $[\alpha/Fe] = +0.0, +0.20, +0.40, +0.60$ . This grid in *Age*,  $[Z/H]$ , and  $[\alpha/Fe]$  allows us to cover a wide range of stellar population properties without overly increasing the execution

---

<sup>2</sup>We refer to *SSP-equivalent parameters* as those of the SSP model that best-matches the position of a given galaxy in the index-index diagrams.



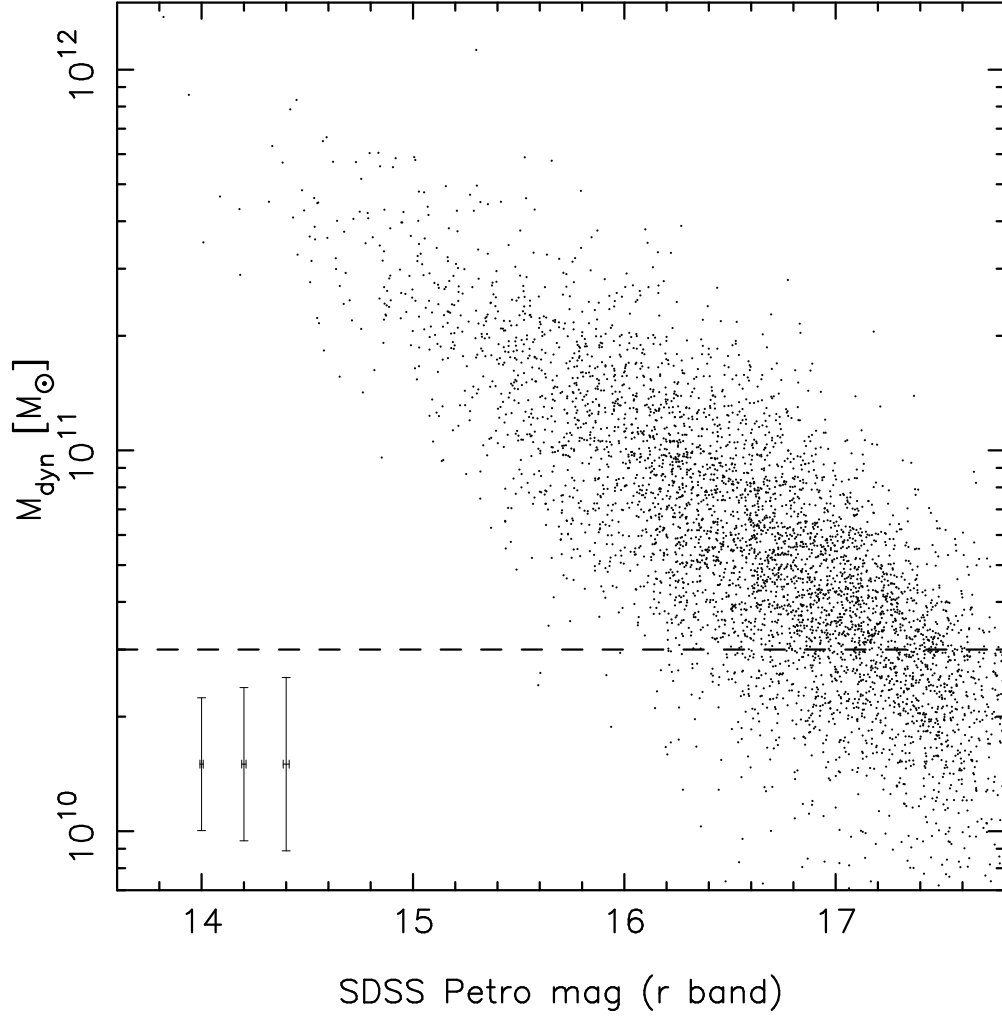


Fig. 1.— Dynamical mass, for ETGs in the optical+NIR sample, as a function of the r-band Petrosian apparent magnitude,  $m_p$ , from SDSS. Considering the scatter in the relation, and assuming the sample to be complete down to  $m_p \sim 17.8$ , we conclude that the ETG’s sample is complete, with respect to  $M_{\text{dyn}}$ , only above  $\sim 3 \times 10^{10} M_{\odot}$ . This mass limit is marked by the horizontal dashed line in the plot. The vertical and horizontal error bars in the lower-left of the Figure correspond (from left to right) to **25-, median, and 75-percentile** errors on  $M_{\text{dyn}}$  and  $m_p$ .

time required to run STARLIGHT<sup>3</sup>. For each galaxy, we first smooth the *basis* models to match the wavelength-dependent resolution of the SDSS spectrum (see Paper I for details). STARLIGHT outputs the light percentage,  $X$ , of each SSP *basis* model in the output synthetic spectrum. Hence, for a given property  $Y$  (e.g. *Age*), one can estimate its *luminosity-weighted* value,  $Y_L$ , as

$$Y_L = \frac{\sum Y \times X}{\sum X}, \quad (2)$$

where the summation is performed over all the SSP *basis* models. The *Age* is obtained directly from Eq. 2. Since metallicity and enhancement are logarithmic quantities, we first apply Eq. 2 by setting  $Y_L = 10^{[Z/H]}$  and  $Y_L = 10^{[\alpha/Fe]}$ , and then compute the logarithm of  $Y_L$  in both cases. The uncertainties on *Age*,  $[Z/H]$ , and  $[\alpha/Fe]$  are computed by comparing the estimates of these quantities for 2,313 galaxies with repeated observations in SDSS, following the same procedure described in Paper I to obtain the errors on  $\sigma_0$ . The average uncertainties are  $\sim 20\%$  on *Age*, and  $\sim 0.05$  for  $[Z/H]$  and  $[\alpha/Fe]$ .

An important potential bias when using the spectra from SDSS is the effect of a fixed spectroscopic fiber aperture on the *Age*,  $[Z/H]$ , and  $[\alpha/Fe]$  estimates. The fraction of galaxy light inside the fiber will vary with galaxy size and redshift. Because we select the SPIDER sample based on the *eClass* parameter, the galaxies are selected to have passive spectra in their centers. This means that, as discussed in Paper I, our putative early-type sample could be contaminated by early spiral systems, i.e. spiral galaxies with a prominent bulge component. Indeed, in Paper I we show that this contamination is about 15%, falling to 5% for a higher quality sample defined on the basis of visual image classification. As we discuss at the end of Sec. 8.3 (Fig. 16), the trends with stellar population properties remain unchanged when restricting the SPIDER sample to the lower contamination subsample. The converse might also hold, i.e. we might be missing ETGs with strong emission features localized to their cores. However, very few ETGs are expected to have spectra exhibiting such strong central emission.

In Fig. 2 we display how *Age*,  $[Z/H]$ , and  $[\alpha/Fe]$  vary with the fraction of light inside the fiber *wrt* the total light,  $L(r < r_{\text{fiber}})/L_{\text{tot}}$ , along with the distribution of this fraction, showing that  $\sim 65\%$  of the galaxies have a ratio between 0.2 and 0.6. The median trends, negligible compared to the scatter in *Age*,  $[Z/H]$ , and  $[\alpha/Fe]$ , show that the derived stellar population parameters are not affected by the aperture effect, reinforcing what we have presented in App. B, i.e. that the average  $r_e$  does not change much *wrt* the stellar population parameters, implying that the correlation of color gradients with stellar population properties has no dependence on  $r_e$ .

---

<sup>3</sup>For 1,600 (out of 39,993 SPIDER) ETGs, we found that all SSP models in the *basis*, but those with  $[\alpha/Fe] = +0.0$ , received zero-weight in the STARLIGHT synthetic spectra. For these objects, we enlarged the *basis* by including also  $\alpha$ -MILES SSPs with  $[\alpha/Fe] = -0.20$ , and re-ran STARLIGHT accordingly.

The values of  $Age$ ,  $[Z/H]$ , and  $[\alpha/Fe]$  used here are *not* SSP-equivalent parameters, as commonly used in the literature, but are luminosity-weighted quantities inferred from the galaxy spectra. As mentioned above, a detailed comparison of SSP-equivalent and luminosity-weighted parameters will be performed in a forthcoming contribution.

#### 4. Color gradient estimates

Internal color gradients are estimated using the same approach as La Barbera & de Carvalho (2009, hereafter LdC09), using the two-dimensional fits to the *grizYJHK* galaxy images with seeing-convolved Sersic models (Paper I). Color gradients are defined as the logarithmic slope of the galaxy radial color profile,  $\nabla_{W-X} = d(W - X)/d(\log \rho)$ , where  $X$  and  $W$  are any two wavebands, and  $\rho$  is the distance to the galaxy center. From *grizYJHK* data we can measure seven independent color gradients. As in LdC09, we calculate the color gradients between the  $g$  band and all other wavebands, in the form of  $\nabla_{g-X}$ . For each galaxy and for each band, we estimate the mean surface brightness of the de-convolved Sersic model on a set of concentric ellipses, whose ellipticities and position angles are fixed to those from the  $r$ -band Sersic fit. The ellipses are equally spaced in equivalent radius  $\rho$  by  $0.01r_{e,r}$ , where  $r_{e,r}$  is the  $r$ -band effective radius. The color index  $g - X$  at a given radius  $\rho$  is obtained by subtracting the mean surface brightnesses at the corresponding ellipse. Each color profile is fitted in the radial range of  $\rho_{min} = 0.1r_e$  to  $\rho_{max} = r_e$  (see e.g. Peletier et al. 1990) using an orthogonal least squares fitting procedure. The slope of the best-fitting profile gives the gradient  $\nabla_{g-X}$ . For the optical sample of ETGs, only the  $\nabla_{g-r}$ ,  $\nabla_{g-i}$ , and  $\nabla_{g-z}$  color gradients are estimated. As discussed in LdC09, small changes in the radial range used in this computation do not significantly change the color gradient estimates.

To estimate the uncertainties on  $\nabla_{g-X}$  we repeated the above procedure by shifting  $r_e$  and  $n$  in each band according to their measurement errors, taking into account the corresponding covariance term (Paper I). We repeat this using  $N = 1000$  shifts, and the errors on  $\nabla_{g-X}$  are then obtained from the widths of the distributions of  $\nabla_{g-X}$ .

#### 5. Distribution of color gradients

Fig. 3 plots the distributions of  $g - X$  color gradients for both the optical and optical+NIR samples of ETGs. For each distribution, we compute the corresponding peak and width ( $\mu$  and  $\sigma$ ) using bi-weight statistics (Beers et al. 1990). The values of  $\mu$  and  $\sigma$ , with the corresponding bootstrap uncertainties, are reported in Fig. 3, as well as in Tabs. 2 and 3 for the optical+NIR and the optical samples of ETGs, respectively. All the distributions are sharply peaked. The peak

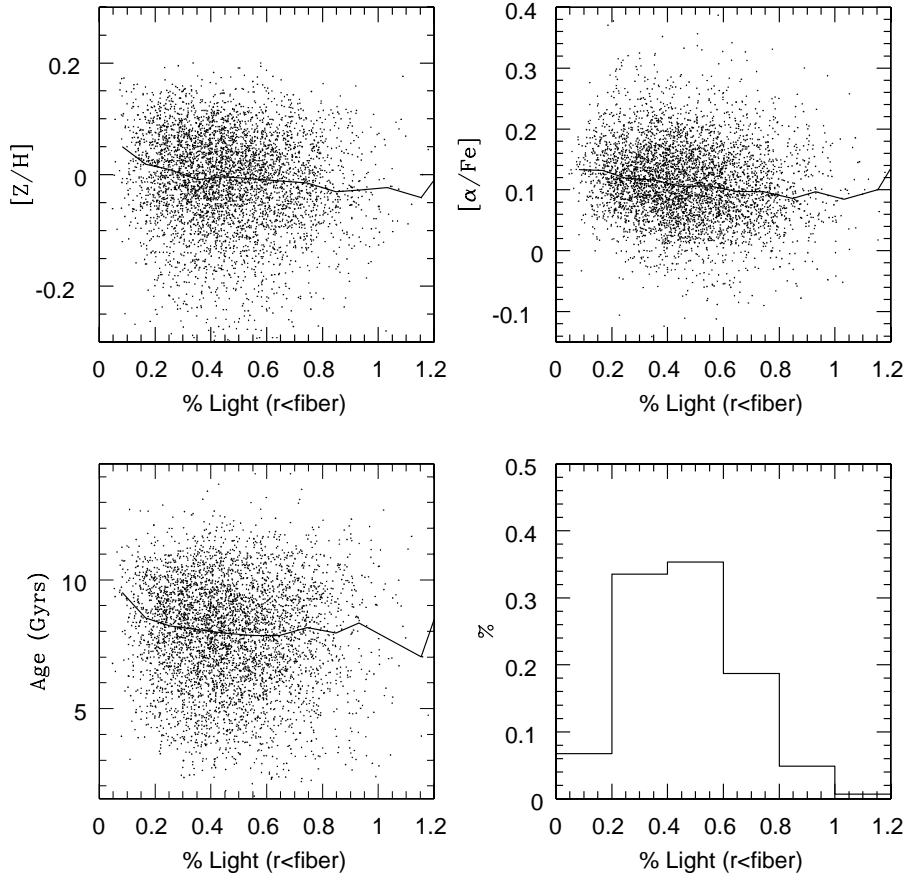


Fig. 2.— Correlation between *Age* (lower left),  $[Z/H]$  (upper left), and  $[\alpha/Fe]$  (upper right) and the fraction of light inside the fiber *wrt* the total light,  $L(r < r_{\text{fiber}})/L_{\text{tot}}$ . The histogram of the fraction is exhibited in the lower right panel. The solid line displayed in each panel corresponds to the median behavior.

value of  $\nabla_{g-X}$  smoothly decreases from about  $-0.07$  in  $g-r$  to  $-0.3$  in  $g-K$ , i.e. the typical color gradient of ETGs becomes increasingly negative as we enlarge the wavelength baseline over which it is computed. It is remarkable that the peak values of  $\nabla_{g-r}$ ,  $\nabla_{g-i}$ , and  $\nabla_{g-z}$ , as well as the corresponding widths, are consistent between the optical (i.e. Tab. 3) and optical+NIR (i.e. Tab. 2) samples of ETGs. Fig. 3 also shows that the distribution of  $g-r$  through  $g-z$  color gradients is consistent between the optical (solid curve in the Figure) and the optical+NIR samples. The width of the  $\nabla_{g-X}$  distributions smoothly increases from  $g-r$  through  $g-K$ . This trend might be due to larger errors on the near-infrared structural parameters than on the optical ones (Paper I), implying that the typical uncertainty on color gradients is larger for the optical–NIR rather than optical–optical  $\nabla_{g-X}$ . Tabs. 2 and 3 provide the median uncertainties on the color gradients,  $\sigma^{err}$ , obtained by propagating the errors on structural parameters (Sec. 4). We estimate the intrinsic width of the  $\nabla_{g-X}$  distributions,  $\sigma^i$ , by subtracting in quadrature  $\sigma^{err}$  from  $\sigma$ , i.e.  $\sigma^i = \left(\sigma^2 - (\sigma^{err})^2\right)^{1/2}$ , with the constraint that  $\sigma^i \geq 0$ . The corresponding intrinsic scatters are reported in Tabs. 2 and 3. It should be noted that this procedure is only a simplistic way of estimating the internal scatter, as it holds only for Gaussian distributions, which is not the case for the color gradient distributions (see Fig. 3). The  $\sigma^i$  increases from  $g-r$  through  $g-K$ , implying that the distribution of optical–NIR color gradients has a significant intrinsic dispersion. The origin of this dispersion is analyzed in Sec. 8, where we study the dependence of stellar population gradients in ETGs on photometric and spectroscopic properties. We also note that the fraction of galaxies having inverted (positive) color gradients becomes less and less pronounced when we move from optical–optical to optical–NIR wavebands. For  $\nabla_{g-K}$ , we find that only a small fraction of ETGs ( $\sim 8\%$ ) exhibit positive color gradients ( $\nabla_{g-K} > 0$ ). From the peak value of  $\nabla_{g-K}$  ( $-0.304$ ) and the intrinsic width of the  $\nabla_{g-K}$  distribution ( $0.187$ , see Tab. 2), we estimate that only  $\sim 5\%$  of galaxies in the optical+NIR sample are expected to have positive  $g-K$  gradients. Hence, the presence of a (small) fraction of objects with positive gradients is a real feature, and not merely explained by galaxies with negative gradients being scattered into the positive region by the measurement errors.

The peak values of  $\nabla_{g-X}$  are consistent, within the uncertainties, with those estimated by La Barbera & de Carvalho (2009) (hereafter LdC09) for the entire SPIDER sample of 5,080 ETGs with optical+NIR data available. A discrepancy is found for  $\nabla_{g-z}$ , for which LdC09 measured a peak value of  $0.089 \pm 0.006$ , while we measure  $-0.111 \pm 0.006$ . This difference does not affect the results of LdC09, since our value of  $-0.111$  is fully consistent with those expected from the best-fitting stellar population models of color gradients in LdC09 (see their Fig. 1). The main differences between the sample of optical+NIR color gradients in this work and that of LdC09 are that (i) we select only the ETGs with better  $\chi^2$  and more accurate structural parameters, and (ii) the computation of color gradients in LdC09 was slightly different than that performed here. We derive the color profiles using, for each band, the two-dimensional Sersic model whose axis ratio and position angle parameters are those measured in that band. In LdC09, we assumed the two

dimensional Sersic models in all bands to have the same axis ratios and position angles as those in the  $r$ -band. This also explains why the color gradient distributions are broader than those measured in LdC09 (see their Tab. 1).

## 6. From color to stellar population gradients

The color gradient reflects the radial variation of stellar populations in a galaxy. We can combine different estimates of color gradients from various pairs of available wavebands to infer the underlying stellar population gradient in an ETG. The approach we follow is presented, in general terms, in Sec. 6.1. In Sec. 6.2 we describe how this approach can be applied when the variation of stellar population properties is mainly due to age and metallicity. We discuss the role of the filters available to SPIDER in reducing the age–metallicity degeneracy. The results of this section are then applied to the color gradient estimates in Sec. 7 to constrain radial variations of age and metallicity within ETGs.

### 6.1. Measuring variations of stellar population parameters

We consider two stellar populations characterized by different physical parameters, such as age, metallicity,  $\alpha$ -enhancement, etc. In general, the problem is how one can use the difference between the color indices of the two stellar populations to infer the corresponding difference(s) in physical parameters. The color index difference may be: (i) radial - the internal color gradient; (ii) between galaxies with different masses - the Fundamental Plane coefficients in different wavebands (see La Barbera et al. 2010b; hereafter Paper II); (iii) in luminosity - the slope of the color-magnitude relation; or (iv) in the residuals in luminosity about a given scaling relation. We first describe the general approach we adopt, and then, in Sec. 7, we focus on its application to

Table 2. Statistics of color gradients for the optical+NIR sample.

color gradient	$\mu$	$\sigma$	$\sigma^{err}$	$\sigma^i$
$\nabla_{g-r}$	$-0.071 \pm 0.004$	$0.189 \pm 0.003$	0.209	0.000
$\nabla_{g-i}$	$-0.093 \pm 0.005$	$0.211 \pm 0.003$	0.192	0.087
$\nabla_{g-z}$	$-0.111 \pm 0.006$	$0.259 \pm 0.004$	0.220	0.136
$\nabla_{g-Y}$	$-0.225 \pm 0.006$	$0.262 \pm 0.004$	0.228	0.128
$\nabla_{g-J}$	$-0.282 \pm 0.007$	$0.306 \pm 0.005$	0.268	0.147
$\nabla_{g-H}$	$-0.286 \pm 0.007$	$0.293 \pm 0.004$	0.277	0.094
$\nabla_{g-K}$	$-0.304 \pm 0.007$	$0.323 \pm 0.005$	0.264	0.187

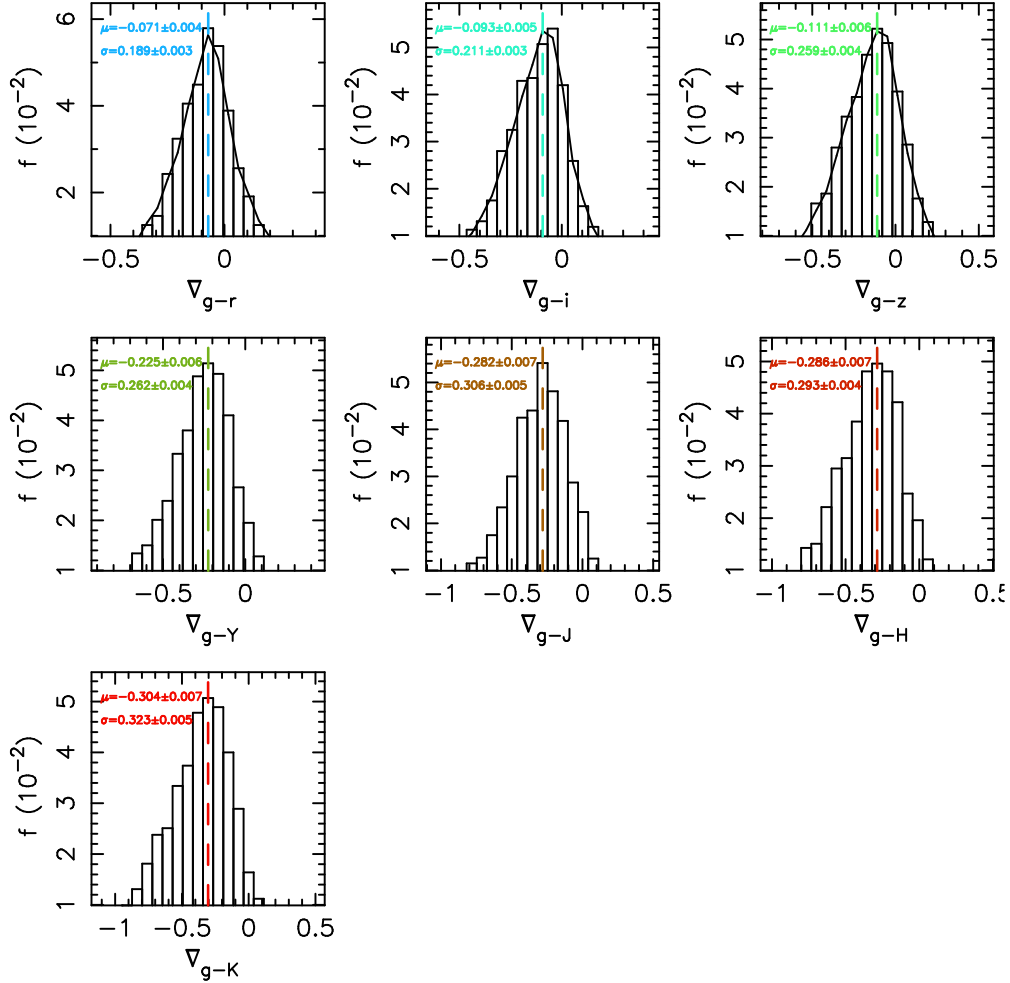


Fig. 3.— Distribution of optical+NIR color gradients of the SPIDER ETGs. From left to right and top to bottom, the histograms show the distributions of  $\nabla_{g-X}$  color gradients, with  $X = rizYJHK$ , for the optical+NIR sample of ETGs. On the y-axis, we report the fraction  $f$  of galaxies in the different  $\nabla_{g-X}$  bins. The peak and width of each distribution are reported in the upper-left corner of each panel, together with the corresponding  $1\sigma$  uncertainties. The vertical dashed lines mark the position of the peaks. The solid black curves in the three top panels show the distributions of  $\nabla_{g-r}$ ,  $\nabla_{g-i}$ , and  $\nabla_{g-z}$  color gradients, for the optical sample of ETGs.

point (i).

We indicate as  $\Delta_i$  the variation of a given physical property between the two stellar populations, where the index  $i$  runs over the considered set of properties. The two stellar populations have differences in colors  $\delta_j$ , where  $j$  spans the set of colors defined by the available wavebands. One can introduce the following approximations:

$$\delta_j = \sum_i A_{ij} \cdot \Delta_i \quad (3)$$

where  $A_{ij}$  is the partial derivative of the  $j$ -th color index with respect to the  $i$ -th stellar population parameter. The above equation holds if (a) the color indices are well behaved functions of the stellar population parameters and either (b1) the  $\Delta_i$  are small enough to assume a linear approximation or (b2) the color indices are linear functions of the stellar population parameters. The quantities  $A_{ij}$  have to be evaluated at the average values of the stellar population parameters of the two stellar populations. Eqs. 3 can be solved in a  $\chi^2$  sense, by minimizing the expression:

$$\chi^2 = \sum_i \left( \delta_i - \sum_k A_{ki} \cdot \Delta_k \right)^2. \quad (4)$$

Requiring that the derivatives of  $\chi^2$  with respect to  $\Delta_j$  vanish, one obtains the following system of equations:

$$\sum_k \left( \sum_i A_{ki} A_{ji} \right) \Delta_k = \sum_i A_{ji} \delta_i. \quad (5)$$

Setting  $M_{jk} = \left( \sum_i A_{ki} A_{ji} \right) \cdot \left( \sum_i A_{ji} \delta_i \right)^{-1}$ , we obtain a new system of  $N$  linear equations in the  $N$  unknown stellar population quantities  $\Delta_j$ :

$$\sum_j M_{ij} \cdot \Delta_j = 1 \quad (6)$$

where the quantities  $M_{ij}$  are completely defined by the partial derivatives  $A_{ij}$  and the measured color differences  $\delta_i$ . If the matrix  $M_{ij}$  is non-degenerate, we can invert the linear system of Eqs. 6 and derive a unique solution for the unknown quantities  $\Delta_i$  (e.g. differences in age, metallicity, ...) from the measured color differences  $\delta_j$ .

Table 3. Statistics of color gradients for the optical sample.

color gradient	$\mu$	$\sigma$	$\sigma^{err}$	$\sigma^j$
$\nabla_{g-r}$	$-0.074 \pm 0.001$	$0.195 \pm 0.001$	0.210	0.000
$\nabla_{g-i}$	$-0.093 \pm 0.001$	$0.213 \pm 0.001$	0.195	0.087
$\nabla_{g-z}$	$-0.112 \pm 0.002$	$0.261 \pm 0.002$	0.222	0.137



## 6.2. Constraining age and metallicity variations

In this section, we investigate how the color indices in SPIDER can be used to constrain variations of stellar population properties in ETGs, specifically the effects of age and metallicity. Since we analyze color gradients in the form  $\nabla_{g-X}$  (Sec. 4), we consider here color indices of the form  $g - X$ , where  $X$  is one of  $rizYJHK$ . The  $g$ -band includes the 4000 Å break at the median redshift of the SPIDER samples, making the  $g - X$  colors most sensitive to the effects of stellar population variations.

For the optical sample, each ETG is characterized by three independent colors,  $g - r$ ,  $g - i$ , and  $g - z$ . Assuming that the relevant stellar population parameters are the age  $t$  and metallicity  $Z$ , equations 3 can be re-written as

$$\delta_{g-r} = \frac{\partial(g-r)}{\partial \log t} \cdot \Delta_t + \frac{\partial(g-r)}{\partial \log Z} \cdot \Delta_Z \quad (7)$$

$$\delta_{g-i} = \frac{\partial(g-i)}{\partial \log t} \cdot \Delta_t + \frac{\partial(g-i)}{\partial \log Z} \cdot \Delta_Z \quad (8)$$

$$\delta_{g-z} = \frac{\partial(g-z)}{\partial \log t} \cdot \Delta_t + \frac{\partial(g-z)}{\partial \log Z} \cdot \Delta_Z. \quad (9)$$

where  $\Delta_t$  and  $\Delta_Z$  are the logarithmic differences of age and metallicity between two stellar populations. As noted above (see beginning of Sec. 6.1), the quantities  $\delta_{g-r}$ ,  $\delta_{g-i}$ , and  $\delta_{g-z}$  could be the differences of color indices between galaxies having different parameters (e.g mass), although here we focus on the case where  $\delta_{g-X}$  is the difference in color index per radial decade in a galaxy, i.e. the internal color gradient ( $\delta_{g-X} \equiv \nabla_{g-X}$ ). In this case, the quantities  $\Delta_t$  and  $\Delta_Z$  provide the difference in age and metallicity per radial decade (i.e.  $\Delta_t \equiv \nabla_t$  and  $\Delta_Z \equiv \nabla_Z$ , see Sec. 7.1). Using the formalism of Sec. 6.1,  $\Delta_t$  and  $\Delta_Z$  are derived by solving the linear system:

$$M_{t,t}\Delta_t + M_{t,Z}\Delta_Z = 1 \quad (10)$$

$$M_{Z,t}\Delta_t + M_{Z,Z}\Delta_Z = 1 \quad (11)$$

where the matrix  $M$  is computed directly from the partial derivative of color indices with respect to  $\log t$  and  $\log Z$ , and the measured color differences  $\delta_{g-r}$ ,  $\delta_{g-i}$ , and  $\delta_{g-z}$ . For the optical+NIR sample of ETGs, the system of Eqs. 7–9 includes four extra equations, corresponding to the  $g - Y$ ,  $g - J$ ,  $g - H$ , and  $g - K$  color indices. The quantities  $\Delta_t$  and  $\Delta_Z$  are still obtained by solving the system of Eqs. 10–11, where the matrix  $M$  is defined by using the color differences in all available wavebands.

Since the NIR light is far less sensitive to metallicity (through line-blanketing) than the optical, and is also less sensitive to age, we expect that including the NIR wavebands helps to (partly) break the age-metallicity degeneracy, i.e. the degeneracy of the matrix  $M$  is reduced when including

all the  $g - X$  color indices. To examine this, we set  $\delta_i = 0.01$  as a typical uncertainty in color differences. We adopt this value of  $\delta_i$  as it is an upper bound for the typical uncertainty on the mean value of color gradients. In fact, the typical error on the color gradient of a given galaxy is  $\sim 0.2\text{--}0.3$  (Tab. 2). For the optical+NIR sample of ETGs, this implies a typical uncertainty on the mean color gradient of  $\sim 0.003\text{--}0.005$ <sup>4</sup>. In order to estimate the derivatives of color indices with respect to age and metallicity, we adopt a polynomial approximation of the magnitude of a given stellar population model with respect to  $t$  and  $Z$ . Details of this approximation are provided in App. C. Here, we consider SSP models from the Bruzual & Charlot (2003) synthesis code (hereafter BC03) with a Scalo IMF. We compute the matrix  $M$  for different values of  $t$  and  $Z$  of these SSP models, in the range where the polynomial approximation holds, i.e.  $5 < t(\text{Gyr}) < 13.5$  and  $0.2 < Z/Z_\odot < 2.5$ . Fig. 4 plots the determinant of the matrix  $M$ ,  $q = \det(M)$ , as a function of  $\log t$  for different metallicities. The case where only optical colors are used is shown by the dashed curves.  $q$  is close to one for non-solar metallicity, while it is always smaller than one (by almost an order of magnitude) in the case of  $Z = Z_\odot$ . This implies that for solar metallicity the matrix  $M$  is nearly degenerate and hence, as expected, optical colors alone are not able to effectively constrain age–metallicity variations. The solid curves show the cases where all the optical+NIR colors are used.  $q$  is then always greater than  $\sim 10$ . In particular, for solar metallicity,  $q$  is two orders of magnitude greater than with optical colors alone, implying that using all of the *grizYJHK* wavebands places much better constraints on age and metallicity variations.

To illustrate this point more quantitatively, we perform Monte-Carlo simulations, setting  $\Delta_t = 0.05$  and  $\Delta_Z = -0.3$ , which correspond to two stellar populations with a difference in age of  $\sim 11\%$  and a factor of two difference in metallicity. These values of  $\Delta_t$  and  $\Delta_Z$  are close to those of the mean age and metallicity internal gradient of ETGs measured by LdC09. Using Eqs. 3, we compute the color differences,  $\delta_i$ , between the two stellar populations for all the seven  $g - X$  colors. The quantities  $A_{ij}$  are computed for  $t = 10\text{Gyr}$  and  $Z = Z_\odot$ . For each iteration, the color indices are shifted according to a normal distribution with a width of  $\sigma_\delta$ , and then we estimate  $\Delta_t$  and  $\Delta_Z$  with the procedure outlined above. The procedure is repeated twice, adopting (i)  $\sigma_\delta = 0.002$  and using only the *griz* colors, and (ii) with  $\sigma_\delta = 0.005$  and all the *grizYJHK* bands. The above  $\sigma_\delta$ ’s represent the typical uncertainties on the mean internal color gradients in the optical and optical+NIR SPIDER samples of ETGs ( see the errors on  $\mu$  reported in Tab. 3 and Tab. 2, respectively). Fig. 5 shows the distributions of inferred  $\Delta_t$  and  $\Delta_Z$ . In both cases, there is a strong correlation between  $\Delta_t$  and  $\Delta_Z$ , implying that even with the full *grizYJHK* filter

---

<sup>4</sup> These values are obtained by dividing the typical errors on color gradients ( $\sim 0.2\text{--}0.3$ ), by the root square of the size of the optical+NIR sample of ETGs. Notice that the resulting expected errors on color gradients are slightly smaller than those on the peak values of  $\nabla_{g-X}$  ( $\sim 0.004\text{--}0.007$ , see Tab. 2), as the peak values are estimated by the bi-weight (rather than the mean) statistics.

set, one cannot completely break the age-metallicity degeneracy. However, the amplitude of the correlated variation is much smaller in the case where the optical and NIR bands are adopted. In fact, although for case (ii)  $\sigma_\delta$  is larger than in case (i), the corresponding error bars on  $\Delta_t$  and  $\Delta_Z$  are much smaller, only  $\sim 0.01$  for both  $t$  and  $Z$ . In other terms, optical+NIR colors constrain the size of the age and metallicity differences more effectively. From Fig.5, we conclude that even a small age gradient of  $\sim 11\%$  can be detected at  $\sim 2.5\sigma$  with the optical+NIR dataset.

## 7. Stellar population gradients

In this section, we present our approach to constraining the variation of stellar population parameters with distance from the ETG center. We consider only the effects of age and metallicity for simplicity, as the proper characterization of a given stellar population may require other quantities (e.g. the shape of the IMF). In App. D, we describe the role of dust extinction gradients in ETGs, discussing their possible impact on our results. We first describe how we estimate the internal age and metallicity gradients (Sec. 7.1). In Sec. 7.2, we show how our approach allows us to define an *effective* color gradient,  $\nabla_\star$ , that results from a combination of all the available color gradients. The systematics in  $\nabla_\star$  estimates are then discussed in Sec. 7.3.

### 7.1. Inferring the age and metallicity gradients

We adopt the procedure described in Sec. 6.2 to infer the radial gradients in age ( $\nabla_t$ ) and metallicity ( $\nabla_Z$ ). Setting  $\delta_{g-X} = \nabla_{g-X}$  in Eqs. 7–9, the quantities  $\Delta_t$  and  $\Delta_Z$  become the logarithmic differences in age and metallicity per radial decade inside a galaxy, i.e.  $\Delta_t \equiv \nabla_t$  and  $\Delta_Z \equiv \nabla_Z$ . Eqs. 7–9 are then rewritten as follows:

$$\nabla_{g-X} = \frac{\partial(g-X)}{\partial \log t} \cdot \nabla_t + \frac{\partial(g-X)}{\partial \log Z} \cdot \nabla_Z, \quad (12)$$

with  $X = r_{iZ}YJHK$ . As shown in Sec. 6.2, in order to derive  $\nabla_t$  and  $\nabla_Z$ , one has to solve the linear system:

$$M_{t,t}\nabla_t + M_{t,Z}\nabla_Z = 1 \quad (13)$$

$$M_{Z,t}\nabla_t + M_{Z,Z}\nabla_Z = 1 \quad (14)$$

where the matrix  $M$  is defined as in Sec. 6.1, setting  $\delta_j = \nabla_{g-X}$ . The computation of  $M$  is performed using different stellar population models. For each model, we use Eqs. 13 and 14 to derive the corresponding  $\nabla_t$  and  $\nabla_Z$ . This procedure, as presented in Sec. 6, minimizes the age-metallicity

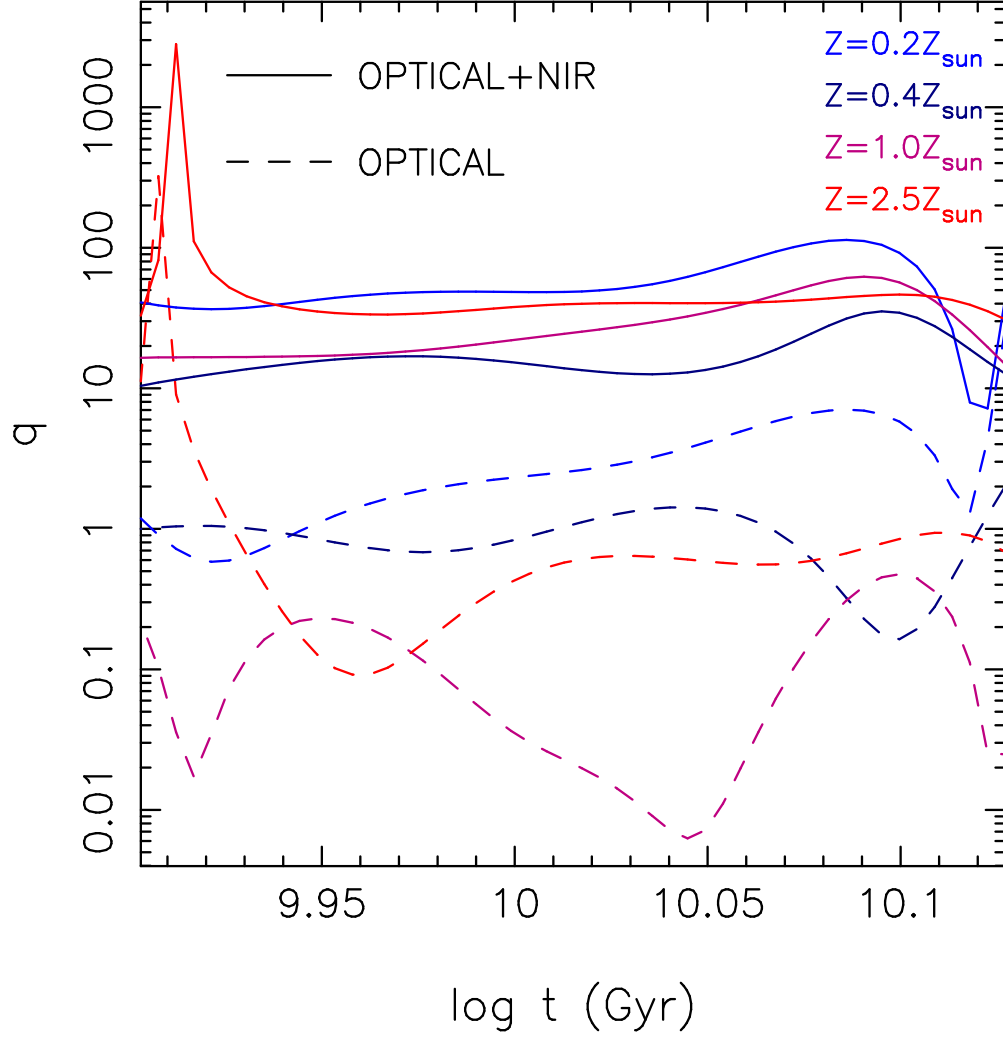


Fig. 4.— Degeneracy,  $q$ , in deriving age and metallicity variations from color indices as a function of the logarithmic age of SSP models from the BC03 synthesis code. Different colors correspond to different metallicities  $Z$ , as shown in the upper-right corner of the plot. Dashed and solid curves correspond to the cases where optical and optical+NIR colors are used, respectively.

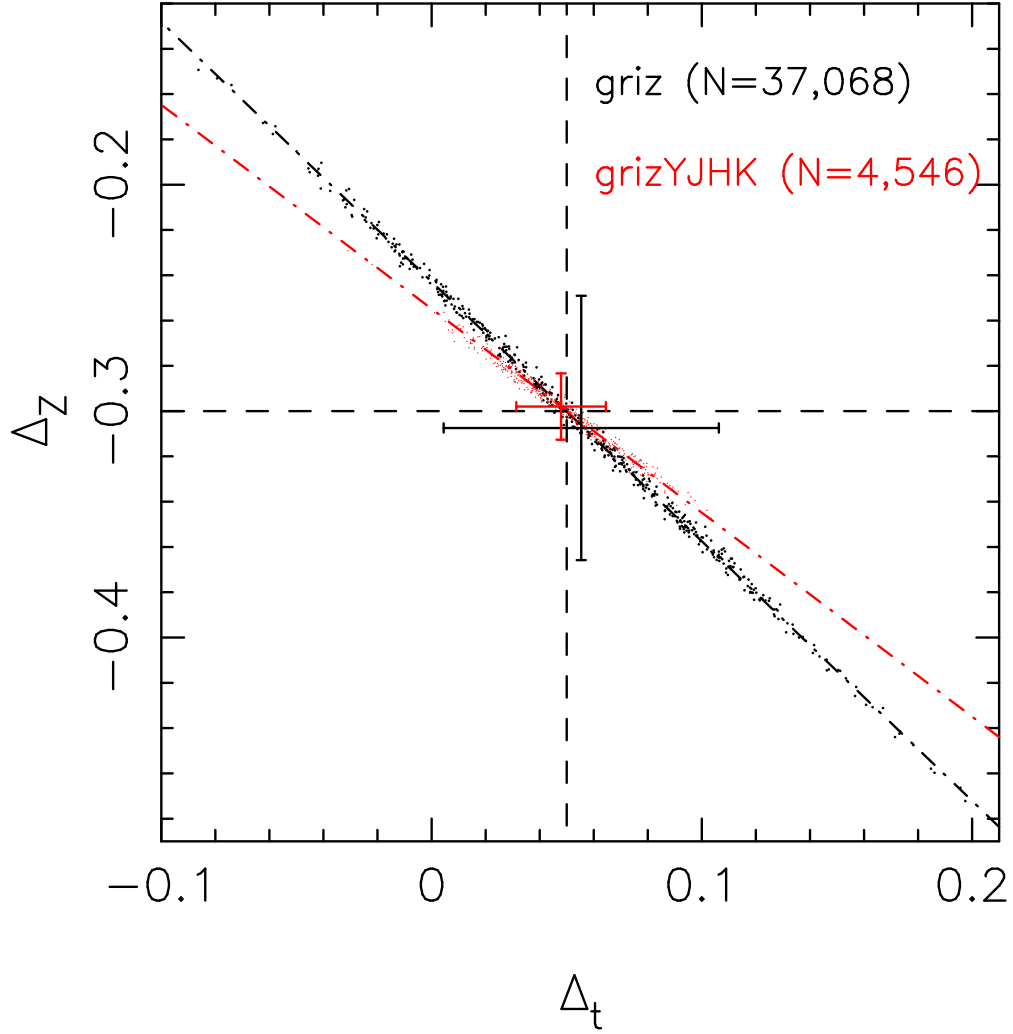


Fig. 5.— Measured  $\Delta_t$  and  $\Delta_z$  from Monte-Carlo simulations, where one shifts color indices according to the typical uncertainties on color gradient estimates, and recovers the true  $\Delta_t$  and  $\Delta_z$  via the approach described in Sec. 6.2. Different colors correspond to cases where optical (black) and optical+NIR (red) color indices are considered. The error bars mark the  $1\sigma$  standard errors for the means of  $\Delta_t$  and  $\Delta_z$  recovered from the Monte-Carlo realizations. The horizontal and vertical dashed lines mark the true values of  $\Delta_t$  and  $\Delta_z$ . The dash-dotted lines are obtained from least-squares orthogonal fitting of  $\Delta_z$  vs.  $\Delta_t$ .

degeneracy depending on how many color terms are available and how they track the most conspicuous spectral features (e.g.  $g - r$  probes the 4000 Å break, yielding important information on the age of the underlying stellar population).

We consider SSP models from three different sources: BC03, Maraston (2005) (M05), and Charlot and Bruzual (2009, in preparation; CB10). These models are based on different synthesis techniques and have different IMFs. The M05 model uses the fuel consumption approach instead of the isochrone synthesis of BC03 and CB10. The CB10 code implements a new AGB phase treatment (Marigo and Girardi 2007). The IMFs are: Scalo (BC03), Chabrier (M05), and Salpeter (CB10). Moreover, we also use a composite stellar population model from BC03 having exponential star formation rate (SFR) with an e-folding time of  $\tau = 1$  Gyr (hereafter  $BC03_{\tau=1\text{Gyr}}$ ). The models are convolved with the *grizYJHK* throughput curves, and the polynomial approximation described in App. C is used to calculate the partial derivatives entering in  $M$ . The derivatives are computed assuming an age of  $t = 9.27$  Gyr, corresponding to a formation redshift of  $z = 2.5$  at the median redshift of the SPIDER sample ( $\langle z \rangle_{\text{median}} \sim 0.07$ ), and solar metallicity ( $Z = Z_{\odot}$ ). For each stellar population model and each galaxy, we perform  $N = 1000$  iterations where in each of them we perturb the observed color gradients according to the corresponding uncertainties. The errors on  $\nabla_t$  and  $\nabla_Z$  are then the widths of their distributions resulting from all iterations. Note that in the above procedure all of the models are computed at the median redshift of our sample ( $z = 0.0725$ ), neglecting the (small) redshift range of the sample. In App. D, we show that this approximation does not affect our results.

## 7.2. The effective color gradient $\nabla_{\star}$

As discussed in Sec. 6.2, even using the entire *grizYJHK* set of wavebands we cannot break the age–metallicity degeneracy. This is further shown in Fig. 6, where we plot the age versus metallicity gradients obtained with the above procedure, for the optical+NIR sample, with the BC03 SSP models. The  $\nabla_Z$  and  $\nabla_t$  estimates are strongly correlated. As shown from the blue dashed line in Fig. 6, obtained from an orthogonal least-squares fit of  $\nabla_Z$  versus  $\nabla_t$ , the correlation is well described by a linear relation:

$$\nabla_Z \propto \alpha \cdot \nabla_t. \quad (15)$$

The correlation is very similar to that between  $\Delta_Z$  and  $\Delta_t$  in Fig. 5. This is shown by the red dotted line in Fig. 6, which is obtained by a linear fit of  $\nabla_Z$  versus  $\nabla_t$  with slope fixed to that of the red dot-dashed line in Fig. 5. The slopes of the blue dashed and red dotted lines differ by only 4%, implying that the strong correlation of  $\nabla_t$  and  $\nabla_Z$  is due mainly to correlated errors on differences in age and metallicity, such as the one between  $\Delta_Z$  and  $\Delta_t$  shown in Fig. 5. In other terms, individual  $\nabla_Z$  and  $\nabla_t$  estimates are affected by large, correlated statistical uncertainties because of the age–

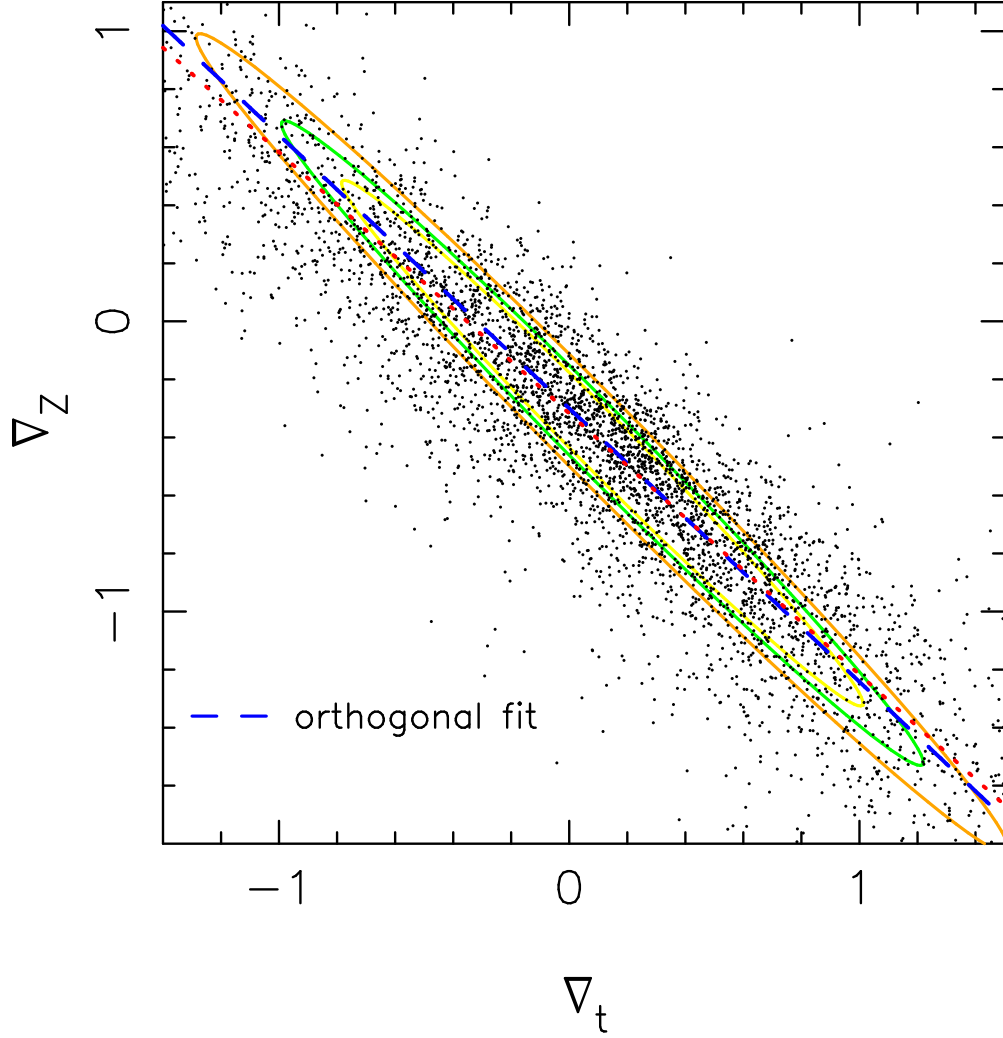


Fig. 6.— Correlation of metallicity and age gradients as estimated for the optical+NIR sample of ETGs, with the BC03 SSP models. The correlation results from the age–metallicity degeneracy of color indices. The dashed line is obtained from a least-squares orthogonal fit of the data, with its slope,  $\alpha$ , being used to define the *effective* color gradient  $\nabla_\star$ . The dotted red line is obtained by fixing the slope of the best-fit line to that of the red line in Fig. 5. The ellipses plot the typical measurement error contours that correspond to the median, 25- and 75-percentile uncertainties on  $\nabla_Z$ .

metallicity degeneracy (see the error ellipses in Fig. 6). However, as shown in Sec. 6.2, using optical+NIR data allows *unbiased estimates of the mean  $\nabla_Z$  and  $\nabla_t$  to be obtained, provided that the number of galaxies is large enough to make statistical uncertainties on the means small enough relative to the absolute values of the differences in age and metallicity (i.e.  $\nabla_t$  and  $\nabla_Z$ )*. This allows us to bin galaxies according to different properties and perform a meaningful comparison of the mean  $\nabla_t$  and  $\nabla_Z$  among different bins (see Sec. 9).

In order to avoid the correlated uncertainties on individual  $\nabla_t$  and  $\nabla_Z$  estimates, we can define an *effective* color gradient:

$$\nabla_\star = \nabla_Z - \alpha \cdot \nabla_t. \quad (16)$$

From a geometrical viewpoint,  $\nabla_\star$  measures the distance of a given point in the  $(\nabla_Z, \nabla_t)$  plane along the  $\nabla_Z$  direction to the line defining the age–metallicity degeneracy. By definition, the correlated variation of  $\nabla_Z$  and  $\nabla_t$ , which is described by Eq. 15, does not change the  $\nabla_\star$ . Hence, the effective color gradient is not affected by the age–metallicity degeneracy. For galaxies having no age gradients,  $\nabla_\star$  reduces to the galaxy metallicity gradient. Moreover, since  $\alpha$  is negative (see below), Eq. 16 can be rewritten as

$$\nabla_\star = \nabla_Z + |\alpha| \cdot \nabla_t. \quad (17)$$

This shows that when  $\nabla_Z = 0$ ,  $\nabla_\star$  is directly proportional to the age gradient. More generally, Eq. 17 shows that  $\nabla_\star$  behaves like a color gradient. A bluer outer stellar population relative to the inner one in a galaxy (because of either a metallicity or age gradient) yields a lower  $\nabla_\star$ . This is further shown in Fig. 7, where we plot  $\nabla_\star$  as a function of all the color gradients (see Sec. 4) for the optical+NIR sample of ETGs. On average,  $\nabla_\star$  monotonically increases as a function of each  $\nabla_{g-X}$ . In essence,  $\nabla_\star$  can be seen as a color gradient that takes into account all of the colors.

Using  $\nabla_\star$  provides three important advantages over traditional color gradients. First, because  $\nabla_\star$  combines all of the color gradient, its statistical uncertainty is significantly smaller than that on any color gradient using one pair of passbands. Second, different samples (bins) of galaxies can be compared using just one quantity ( $\nabla_\star$ ), rather than separately for each color gradient. Finally, as we prove below (Sec. 7.3), the effective color gradient is a completely model-independent quantity (in the same way as the observed color gradients), which is not the case for  $\nabla_Z$  and  $\nabla_t$ .

For each stellar population model, we derive  $\alpha$  via an orthogonal least-square fit of  $\nabla_Z$  vs.  $\nabla_t$  for all galaxies. Then we calculate  $\nabla_\star$  for each galaxy, using Eq. 16. The value of  $\alpha$  changes between different models, as well as for a given model when using a different set of wavebands (i.e. optical vs. optical+NIR). For the optical+NIR wavebands, we obtain  $\alpha = -0.943$  (BC03),  $-0.663$  (CB10),  $-1.341$  ( $BC03_{\tau=1Gyr}$ ), and  $-0.713$  (M05). For the optical wavebands, we obtain  $\alpha = -1.280$ ,  $-1.186$ ,  $-1.756$ , and  $-1.007$ , respectively.



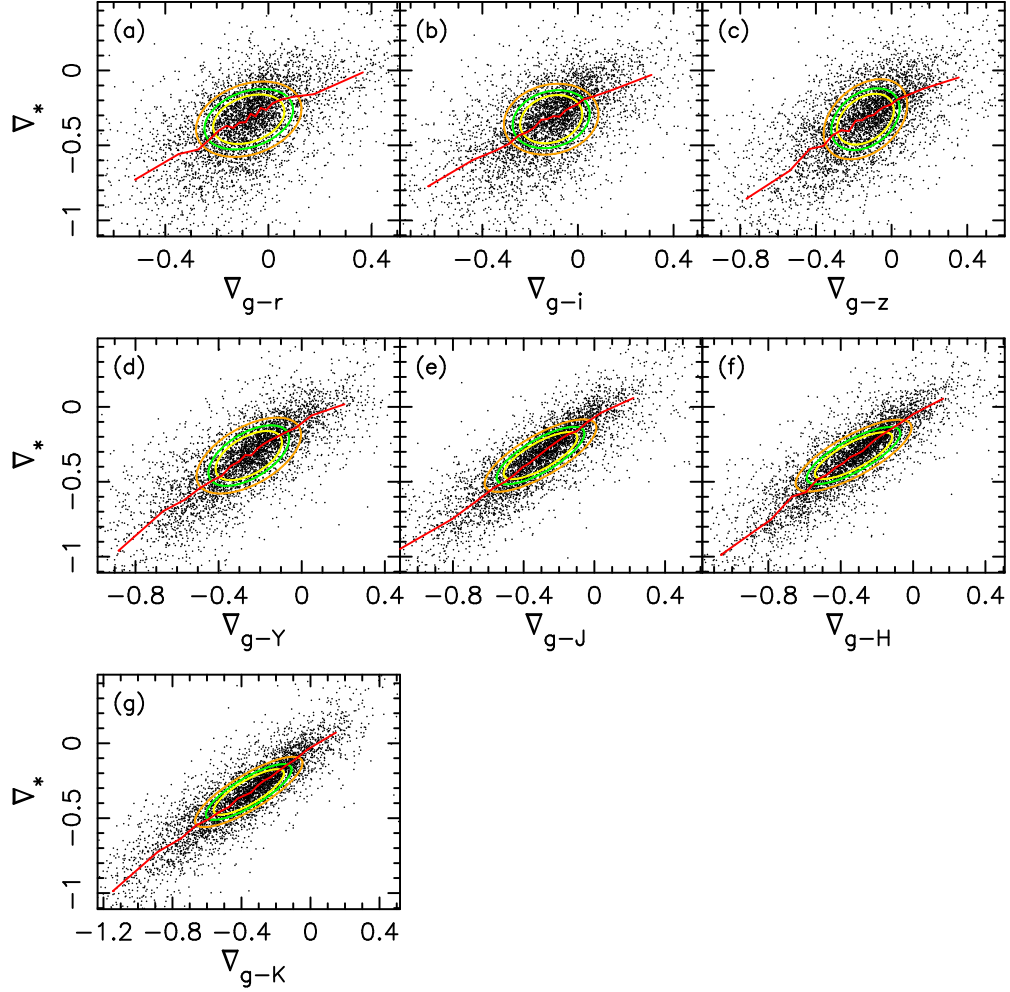


Fig. 7.— Correlation of the effective color gradient,  $\nabla_*$ , with the  $g - X$  color gradients,  $\nabla_{g-X}$ . From left to right, and top to bottom, the  $X$  ranges from  $g$  through  $K$ . For each panel, the red curve is obtained by median binning the  $\nabla_*$  wrt the corresponding color gradient, while the ellipses plot the typical measurement error contours that correspond to the median, 25- and 75-percentile uncertainties on  $\nabla_*$ .

### 7.3. Systematics in $\nabla_\star$

We examine how sensitive  $\nabla_\star$  is to varying the set of utilized wavebands. This is shown in Fig. 8, where we compare the  $\nabla_\star$  measured with optical+NIR and only optical bands. These two values of  $\nabla_\star$  are linearly related, indicating that optical data alone can still provide a reliable estimate of the *effective* color gradient. This is consistent with the fact that  $\nabla_\star$  is not affected by the age-metallicity degeneracy (influencing the optical more than the optical+NIR gradients) and is also proportional to each of the color gradients. On the other hand, the slope of the correlation between  $\nabla_\star$  (optical) and  $\nabla_\star$  (optical+NIR) is significantly greater than one at  $2.00 \pm 0.03$ . This reflects the reduced statistical uncertainty on  $\nabla_\star$  when incorporating the NIR information. This is further shown in Fig. 9 where we compare the histograms of  $\nabla_\star$  obtained using optical and optical+NIR data. The width of the  $\nabla_\star$  distribution is significantly larger when using optical *wrt* optical+NIR data. Also, a small offset in the peak of the two distributions is present. These results are quantified in Tab. 4 where we report the statistics, i.e. the peak ( $\mu$ ) and width ( $\sigma$ ) as estimated using the bi-weight estimator (Beers et al. 1990), for different samples and stellar population models. In the same Table, we also report the median uncertainty,  $\sigma_\star^{err}$ , as well as the intrinsic width,  $\sigma_\star^i$ , defined in the same way as the quantity  $\sigma^i$  in Sec. 5. From these data we conclude that for the optical+NIR sample, the peaks of the  $\nabla_\star$  distributions are consistent for different stellar population models, i.e. the  $\nabla_\star$  estimated from optical+NIR is model-independent. In contrast, when using only optical data, a significant systematic difference is present between the peak values of different models, though this difference is quite small ( $< 0.02$ ) *wrt* the absolute peak value of  $\nabla_\star$ . Furthermore, in agreement with Fig. 9, we see that  $\sigma$  is significantly larger when using optical data ( $\sigma \sim 0.4$ ) as opposed to using optical+NIR data ( $\sigma \sim 0.25$ ), i.e.  $\nabla_\star$  is affected by significantly larger uncertainties (by a factor of  $\sim 1.6$ ) when using only optical data. Finally, the peak values of the optical and optical+NIR  $\nabla_\star$  are slightly different, in the sense that the *effective* color gradients are on average more negative by  $\sim 0.06$  for the optical+NIR than for the optical samples. The differences in  $\mu$  might be due to the different shapes of the optical and optical+NIR  $\nabla_\star$  distributions, rather than some intrinsic difference. In fact, as seen in Fig. 9, the distribution of  $\nabla_\star(\text{optical})$  is clearly asymmetric.

The robustness of  $\nabla_\star$ ,  $\nabla_Z$  and  $\nabla_t$  with respect to the adopted stellar population model is illus-

Table 4. Statistics of the *effective* color gradients.

model	optical+NIR sample				optical sample			
	$\mu$	$\sigma$	$\sigma_\star^{err}$	$\sigma_\star^i$	$\mu$	$\sigma$	$\sigma_\star^{err}$	$\sigma_\star^i$
BC03	$-0.283 \pm 0.007$	$0.246 \pm 0.005$	0.163	0.184	$-0.219 \pm 0.004$	$0.407 \pm 0.002$	0.377	0.152
M05	$-0.286 \pm 0.007$	$0.246 \pm 0.005$	0.164	0.182	$-0.209 \pm 0.003$	$0.388 \pm 0.002$	0.355	0.157
CB10	$-0.296 \pm 0.007$	$0.254 \pm 0.005$	0.181	0.178	$-0.235 \pm 0.004$	$0.436 \pm 0.003$	0.406	0.160
BC03 $_{\tau=1\text{Gyr}}$	$-0.291 \pm 0.008$	$0.257 \pm 0.005$	0.162	0.200	$-0.225 \pm 0.004$	$0.417 \pm 0.002$	0.390	0.147

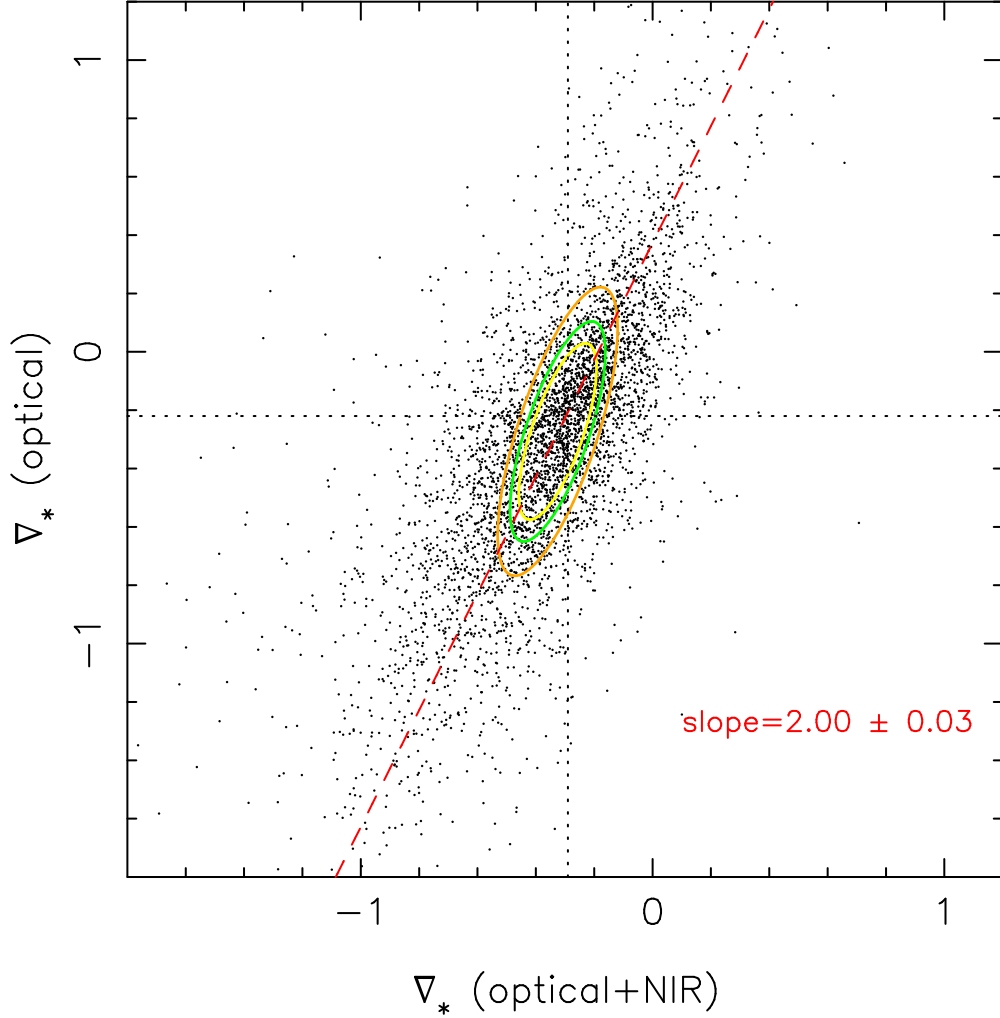


Fig. 8.— Comparison of the effective color gradient derived using either optical or optical+NIR wavebands. The dashed red line shows the orthogonal best-fitting relation between the two  $\nabla_*$  estimates. The slope of the relation is reported in the lower-right corner of the plot. The horizontal and vertical dotted lines mark the peaks of the distribution of  $\nabla_*$  for the optical and optical+NIR data, respectively. The ellipses plot the typical measurement error contours that correspond to the median, 25- and 75-percentile uncertainties on the optical+NIR  $\nabla_*$ . The ellipses are constructed by assuming, for simplicity, that the covariance term of the errors is proportional to that of the data themselves.

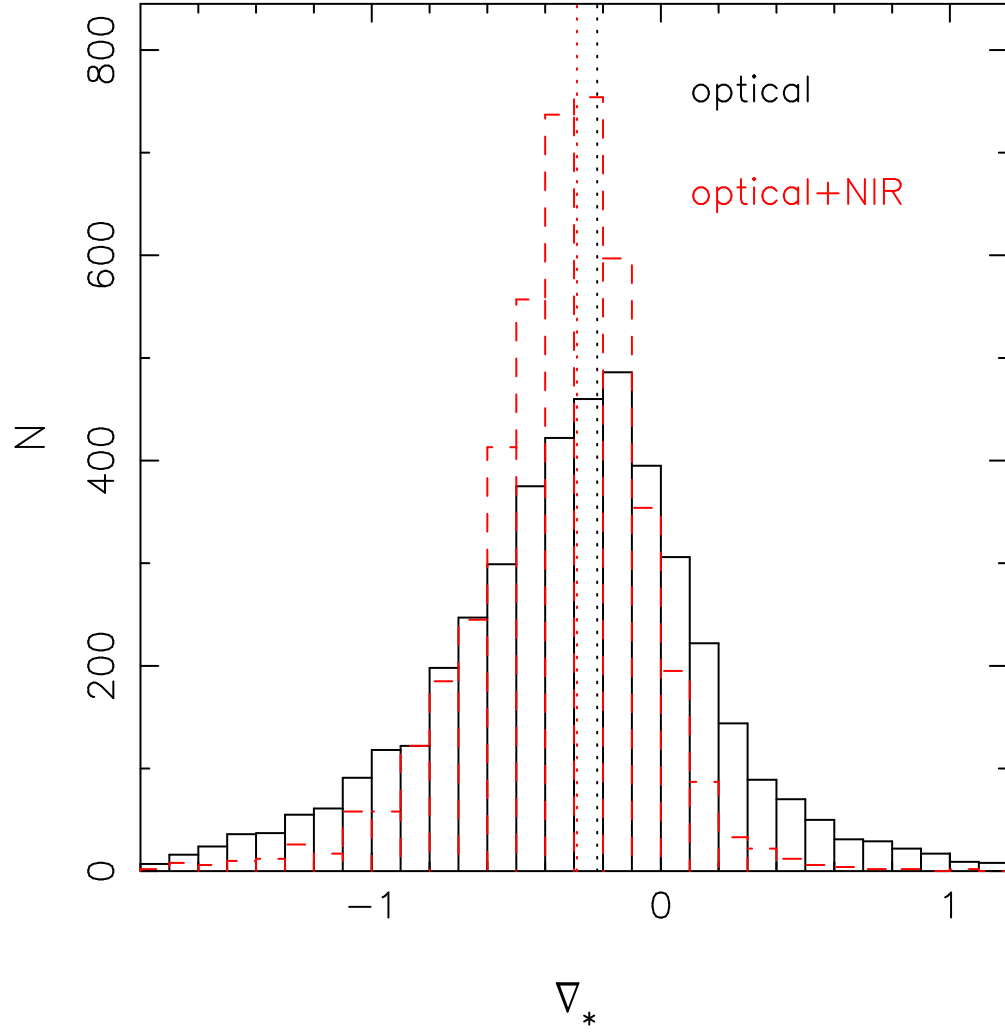


Fig. 9.— Comparison of the distribution of effective color gradients, obtained using either optical (black) or optical+NIR (red) data. The peaks of the two distributions are marked by the vertical dotted lines. Note how the distribution becomes narrower when including the NIR wavebands.

trated in Fig. 10, where we compare the  $\nabla$ ’s obtained using the optical+NIR sample of ETGs for BC03 and M05. We see that the scatter in  $\nabla_\star$  is significantly reduced in comparison to that for  $\nabla_Z$  or  $\nabla_t$ . As noted above,  $\nabla_\star$  is model-independent, while this is obviously not the case for  $\nabla_Z$  and  $\nabla_t$ . This gives extra support to using  $\nabla_\star$  as a useful and robust representation of the radial gradients of stellar population properties in galaxies.

## 8. Dependence of the effective color gradient on galaxy parameters

From Table 4 we see that the stellar population gradients exhibit significant intrinsic dispersion, motivating an analysis of the correlations of  $\nabla_\star$  versus other galaxy parameters. We study correlations of  $\nabla_\star$  with several photometric quantities (Sec. 8.1), different estimates of galaxy mass (Sec. 8.2), and spectroscopic parameters like central velocity dispersion and stellar population indicators like age, metallicity and  $[\alpha/Fe]$  abundance ratio (Sec. 8.3). Because of the large statistical uncertainty on individual measures of stellar population gradients, we bin the data and analyze trends with the mean  $\nabla_\star$ . In each case, we verified that changing the number of galaxies in each bin does not affect our results. The results presented in the following subsections refer to  $\nabla_\star$  computed using the BC03 SSP models. Similar findings hold when considering other stellar population models described in Sec. 7.

### 8.1. Effective gradients vs. photometric properties

We bin  $\nabla_\star$  with respect to the following photometric parameters:  $r$ - and  $K$ -band effective half-light radii, ( $R_{e,r}$  and  $R_{e,K}$ );  $r$ - and  $K$ -band total magnitudes ( $^{0.07}M_r$  and  $^{0.07}M_K$ ), obtained through a PSF-convolved Sersic modeling of the galaxy image; logarithmic median Sersic index ( $\langle \log n \rangle$ ); median axis ratio ( $\langle b/a \rangle$ ); the  $a_4$  parameter, which characterizes the galaxy isophotal shape (boxiness -  $a_4 < 0$  and diskyness -  $a_4 > 0$ , see Paper I); the optical-NIR color index ( $r - K$ ) and the median PSF fitting  $\chi^2$  ( $\chi^2_{\text{PSF}}$ , Fig. 11). For each galaxy, median values are computed using data at the available wavebands, i.e. *griz* and *grizYJHK*. We adopted the  $r$ - and  $K$ -band radii and magnitudes as representative of the sizes and luminosities of galaxies in the optical and NIR spectral regions, respectively. The  $r - K$  color index is estimated using 2DPHOT total galaxy magnitudes. Each bin includes the same number of galaxies, i.e.  $N = 200$  ETGs for the optical+NIR sample and  $N = 2000$  ETGs for the optical sample.

Fig. 11 shows the relations between  $\nabla_\star$  and the photometric quantities listed above. Panels (a) and (c) show that  $\nabla_\star$  changes significantly with the  $r$ -band effective radius and  $r$ -band total absolute magnitude in the sense that larger and more optically luminous ETGs have stronger (more

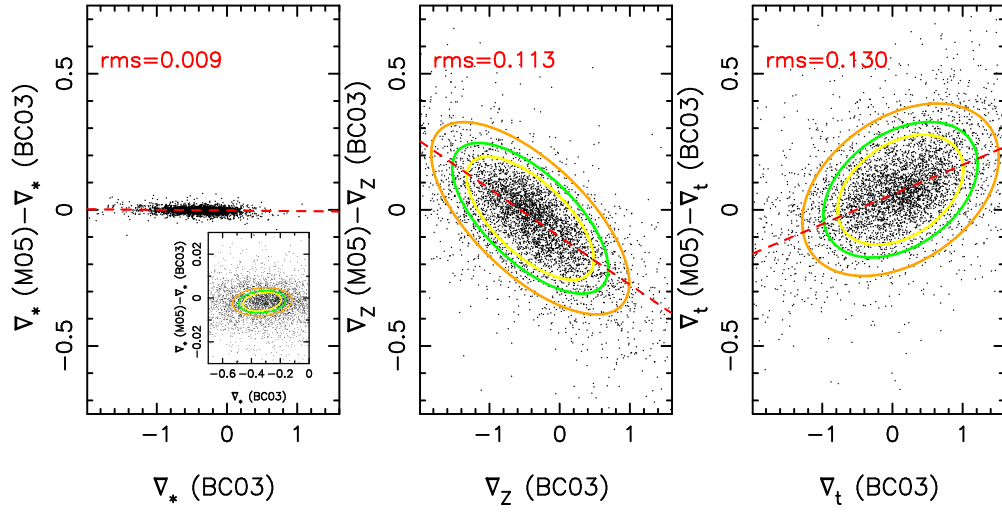


Fig. 10.— Comparison of effective color (left), metallicity (middle) and age gradients (right) derived by using M05 and BC03 SSP models. Each panel plots the gradient difference in the sense of M05-BC03 as a function of BC03 gradients. The red dashed lines are the orthogonal best-fitting relations. The ellipses plot the typical measurement error contours that correspond to the median, 25- and 75-percentile uncertainties on the x-axis variables. The covariance terms of the errors are derived as for Fig. 8. The left inset panel zooms into the center of the distribution to make the error ellipses visible.

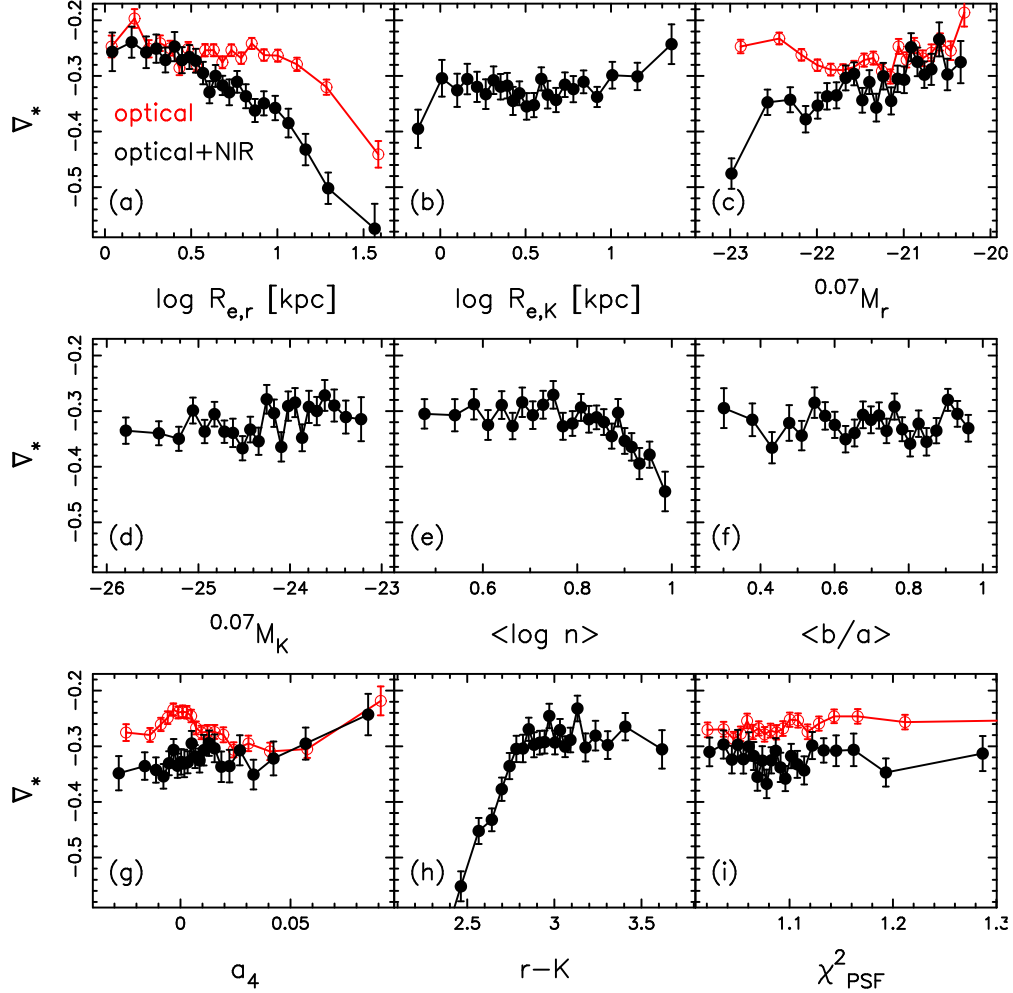


Fig. 11.— Dependence of effective stellar population gradients on galaxy structural parameters. Each plot has been obtained by binning the  $\nabla_*$  with respect to a given quantity  $p$ . The following quantities are plotted: the  $r$ -band effective radius (panel a),  $K$ -band effective radius (panel b),  $r$ -band absolute magnitude (panel c),  $K$ -band absolute magnitude (panel d), logarithmic median of the *grizYJHK* Sérsic indices (panel e), median of the *grizYJHK* axis ratios (panel f), the median of the  $a_4$  parameters in the *gri* passbands (panel g),  $r - K$  color index (panel h), median of the PSF modeling  $\chi^2_{PSF}$  in the *grizYJHK* passbands (panel i). For each panel, the circles are the median  $\nabla_*$  in different bins of  $p$ . Error bars are  $1\sigma$  standard errors on the medians. The circles are connected by solid lines. The ETG sample with optical+NIR data is plotted in black. For panels (a), (c), (g), and (i), the binning is also done for the optical sample of ETGs (red color).

negative) effective color gradients. This result is somewhat expected as a more negative  $\nabla_\star$  implies that bluer (either less metal rich or younger) stars in the galaxy are preferentially distributed towards the galaxy periphery. We note that the trend with  $^{0.07}M_r$  is weaker than that with  $R_{e,r}$ . When we restrict ourselves to only optical data the trends with radius and magnitude are less pronounced (see below). Moreover,  $\nabla_\star$  has no dependence on radius or luminosity when we use  $K$ -band (Panels b and d). This finding is of particular interest, as the NIR light follows more closely the stellar mass distribution than the optical light. It implies that for bright ETGs the effective color gradient does not vary significantly along the stellar mass sequence. A mild correlation exists between  $\nabla_\star$  and Sersic index, as shown in Panel (e). For  $\log n > 0.75$  ( $n > 5.6$ ) ETGs with higher  $n$  tend to have stronger effective color gradients, likely because galaxies with higher  $n$  have higher luminosity due to the (optical) luminosity–Sersic index relation of ETGs (Caon, Capaccioli, & D’Onofrio 1993). Panel (f) shows no trend whatsoever of  $\nabla_\star$  with axis ratio while with the boxy/disky parameter  $a_4$ , shown in Panel (g), a weak correlation is present especially when optical+NIR data is used. In panel (h) we show that a strong correlation exists between  $\nabla_\star$  and total galaxy colors. For  $r - K < 2.9$ , galaxies with bluer colors also tend to have stronger gradients. This is not a spurious result arising from the correlation of galaxy colors and magnitudes. In fact, the color-magnitude relation implies that brighter galaxies should have redder colors. This, together with the trend of  $\nabla_\star$  with  $^{0.07}M_r$ , would produce a trend opposite to that seen in Panel (h). Moreover, as shown in Paper I, no significant correlation is found between total magnitudes and total (rather than aperture) galaxy colors. Finally, Panel (i) probes possible systematics in color gradient estimates related to the PSF modeling. It shows that  $\nabla_\star$  is not correlated with the  $\chi^2$  from fitting the galaxy image with a PSF convolved Sérsic light distribution. Hence, our PSF models are accurate enough to provide, on average, unbiased  $\nabla_\star$  estimates.

In summary, we find that the effective color gradient in (bright) ETGs do not correlate with (NIR) luminosities and galaxy radii, while a correlation exists with galaxy colors. The former finding is further investigated in the next section, where we analyze the trend of  $\nabla_\star$  with galaxy mass. The correlation of  $\nabla_\star$  with colors is further studied in Sec. 8.3, where we bin  $\nabla_\star$  with respect to the stellar population parameters of ETGs.

The lack of correlation between  $\nabla_\star$  and  $R_{e,K}$  (Panel b of Fig. 11) deserves further comments. In Paper II we show that the ratio of optical ( $g$ -band) to NIR ( $K$ -band) effective radii,  $R_{e,g}/R_{e,K}$  decreases as a function of  $R_{e,K}$ , with the largest galaxies having  $R_{e,g}/R_{e,K} \sim 1$  (see Fig. 7 of Paper II). This variation implies that the slope of the Kormendy relation for ETGs increases from  $g$  through  $K$ . A similar result, at optical wavebands ( $g - r$ ), has been recently reported by Roche, Bernardi, and Hyde (2010). Using the ratio of optical radii as a proxy for the color gradient, the decrease of  $R_{e,g}/R_{e,K}$  with  $R_{e,K}$  implies that larger galaxies should have shallower gradients (see also Tortora et al. 2010), in contrast with the lack of correlation in Panel b of Fig. 11. However, color gradients are determined not only from the ratio of effective radii but also from that



of the Sersic indices. In fact, the variation of the surface brightness profile between two wavebands is determined from both  $R_e$  and  $n$ . Fig. 12 plots the logarithmic binned ratio of  $g$  to  $K$ -band Sersic indices,  $\log n_g/n_K$ , as a function of  $\log R_{e,K}$ . We find that  $n_g/n_K$  decreases as a function of  $R_{e,K}$ , i.e. larger galaxies are more concentrated in the NIR than lower- $R_{e,K}$  systems. This compensates for the trend of  $R_{e,g}/R_{e,K}$  with  $R_{e,K}$ , making  $\nabla_\star$  nearly constant with NIR radius. Thus there is no inconsistency between the lack of correlation in Panel b of Fig. 11 and the correlation shown in Fig. 7 of Paper II.

As mentioned above, we find that color gradients exhibit a complex behavior with galaxy luminosity. When estimated from optical+NIR color gradients,  $\nabla_\star$  becomes more negative as the optical magnitude becomes brighter. On the contrary, for the optical sample of ETGs, i.e. when  $\nabla_\star$  is estimated from  $\nabla_{g-r}$ ,  $\nabla_{g-i}$ , and  $\nabla_{g-z}$ , this steepening disappears, and  $\nabla_\star$  does not vary with  $M_r$  (Panel c of Fig. 11). The reason for the different behavior of  $\nabla_\star$ , when estimated using optical vs. optical+NIR data is illustrated in Fig. 13, where we plot the median color gradient,  $\nabla_{g-X}$ , as a function of the optical magnitude for all the available wavebands ( $X = rizYJHK$ ). The trends of  $\nabla_{g-X}$  with  $^{0.07}M_r$  are modeled with second-order polynomials (dashed curves in the Figure). The most remarkable feature is that the color gradient variation with magnitude depends on the waveband. The  $\nabla_{g-r}$  gradient exhibits a double-valued behavior, becoming flatter in both more and less luminous galaxies. For  $\nabla_{g-z}$ , the double-valued behavior disappears and the  $\nabla$  decreases monotonically as a function of  $^{0.07}M_r$ . At redder wavebands, the trend reverses, and  $\nabla_{g-X}$  becomes a monotonically increasing function of  $^{0.07}M_r$ . As shown in Fig. 7, the effective color gradient is proportional to each of the individual color gradients from which it is estimated. When using optical data alone,  $\nabla_\star$  mainly reflects the behavior of  $\nabla_{g-r}$ ,  $\nabla_{g-i}$ , and  $\nabla_{g-z}$ . As a result,  $\nabla_\star$  exhibits no strong variation with luminosity, similar to the double-valued behavior of  $\nabla_{g-r}$ . When  $\nabla_\star$  is estimated from optical+NIR data, the optical-NIR gradients dominate the trend, with  $\nabla_\star$  an increasing function of  $^{0.07}M_r$ . The main conclusion is that the behavior of color gradients with luminosity depends on the waveband where the luminosity is estimated (Panels c and d of Fig. 11), as well as the wavebands used to estimate the gradient itself. This complex dependence may explain, at least partly, the discrepant results found in the literature about the relation between color gradients and luminosity (mass). For instance, Peletier et al. (1990) first reported a surprising lack of correlation between color gradients and galaxy luminosity, noting that brightest ellipticals do not exhibit less steep gradients, as expected if they were the debris of repeated mergers of lower mass systems. de Propris et al. (2005) also reported no correlation between the size of the color gradients and galaxy luminosity. Tamura & Ohta (2003) found that color gradients in cluster ETGs become steeper (more negative) in brighter galaxies. The same result was found by Balcells & Peletier (1994) for the bulges of spiral galaxies. On the other hand, La Barbera et al. (2005) found that color gradients do not depend on galaxy luminosity, and Choi et al. (2007) found that optical color gradients are essentially constant over a wide range of galaxy luminosity, with a weak trend of

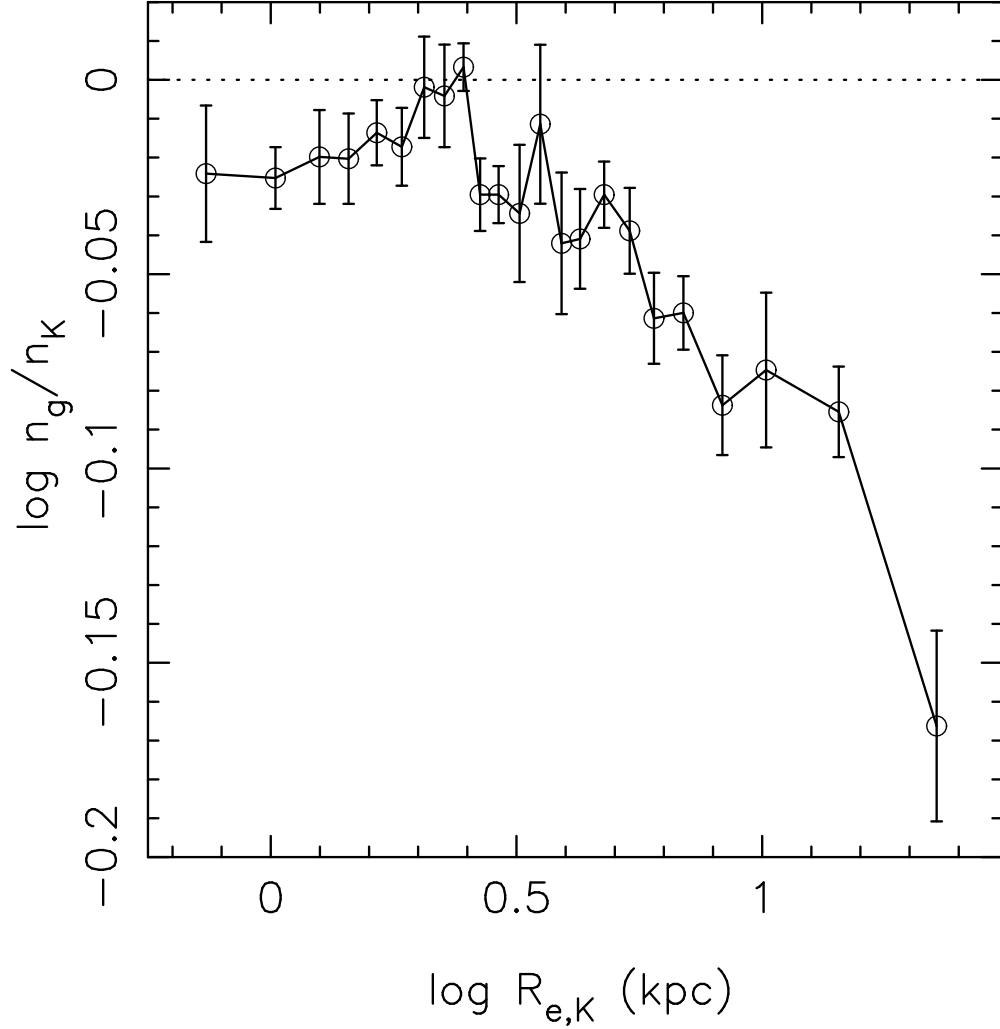


Fig. 12.— Logarithmic ratio of  $g$  to  $K$ -band Sersic indices as a function of  $\log R_e$  in  $K$ -band. The solid line connects the data-points obtained by median binning the distribution of  $\log n_g/n_K$  with respect to  $\log R_{e,K}$ , with each bin including the same number ( $N=200$ ) of points. The trend implies larger galaxies to have a profile shape more concentrated in the NIR than in the optical (i.e. lower  $n_g/n_K$ ). The dotted line marks zero Sersic index ratio. Error bars denote the  $1\sigma$  errors on the median in each bin.

becoming flatter at both fainter and brighter magnitudes. Recently, Roche, Bernardi, and Hyde (2010, hereafter RBH10), using the ratio of  $g$ - to  $r$ -band effective radii from the SDSS as a proxy for the color gradient, also found that ETGs with intermediate luminosity have stronger gradients than those at low and high luminosities, in agreement with the double-valued behavior we observe for  $\nabla_{g-r}$ .

## 8.2. Effective color gradient vs. galaxy mass

Fig. 14 plots the median  $\nabla_\star$  as a function of galaxy stellar ( $M_\star$ ) and dynamical ( $M_{dyn}$ ) mass. The binning is performed as in Fig. 11, with each bin having the same number of galaxies. To quantify the dependence of  $\nabla_\star$  on mass, we perform linear least-squares fits of  $\nabla_\star$  with respect to  $M_\star$  and  $M_{dyn}$ , with the slopes reported in the figure. We find no trend of the effective color gradient with mass. In particular, the slope of  $\nabla_\star$  vs.  $M_{dyn}$  is consistent with zero at the  $1.5\sigma$  significance level, while the slope of  $\nabla_\star$  vs.  $M_\star$  is consistent with zero at  $\sim 0.5\sigma$ . For  $M_{dyn} < 2 \times 10^{11} M_\odot$ , the  $\nabla_\star$  becomes more negative than at higher mass, but this effect might not be real, as in this mass regime, the SPIDER sample is incomplete due to the  $r$ -band magnitude selection (see Fig. 1). We verified that the trend with stellar mass remains unchanged when using different stellar population models (e.g. CB10) to perform the SED fitting (Sec. 3.1).

## 8.3. Effective color gradient vs. velocity dispersion and stellar population properties

Fig. 15 plots the median effective color gradient,  $\nabla_\star$ , as a function of central velocity dispersion, age, metallicity, and  $\alpha$ -enhancement, for both the optical and optical+NIR samples. For the optical, the plot of  $\nabla_\star$  vs.  $\log \sigma_0$  seems to suggest a double-valued behavior, with  $\nabla_\star$  reaching a minimum around  $\log \sigma_0 \sim 2.2$ . However, this is not confirmed by the optical+NIR data, where no trend appears. This result supports the findings of Secs. 8.1 and 8.2, that  $\nabla_\star$  is not driven by galaxy mass. On the contrary, we find a strong dependence of  $\nabla_\star$  on stellar population properties, i.e. the age,  $[Z/H]$ , and  $[\alpha/Fe]$ . In order to quantify these trends, we perform a robust linear fit of  $\nabla_\star$  as a function of each of the three parameters, minimizing the sum of absolute residuals in  $\nabla_\star$ . The uncertainties on fitting coefficients are estimated by the width of their distribution among 1000 iterations, where the median  $\nabla_\star$  in each bin are shifted according to their error bars, and the fitting process is repeated. The slope and offset of the best-fit lines are reported in Tab. 5. From Panel (b), we see that the effective color gradient is flat for galaxies with older stellar populations. The trend is statistically significant for both the optical and optical+NIR samples, with the slopes of  $\nabla_\star$  vs.  $Age$  relations greater than zero at  $\sim 3$  and  $\sim 9\sigma$ , respectively. We note that galaxies with ages younger than  $\sim 4$  Gyr seems not to follow the same trend as galaxies with older ages. As discussed

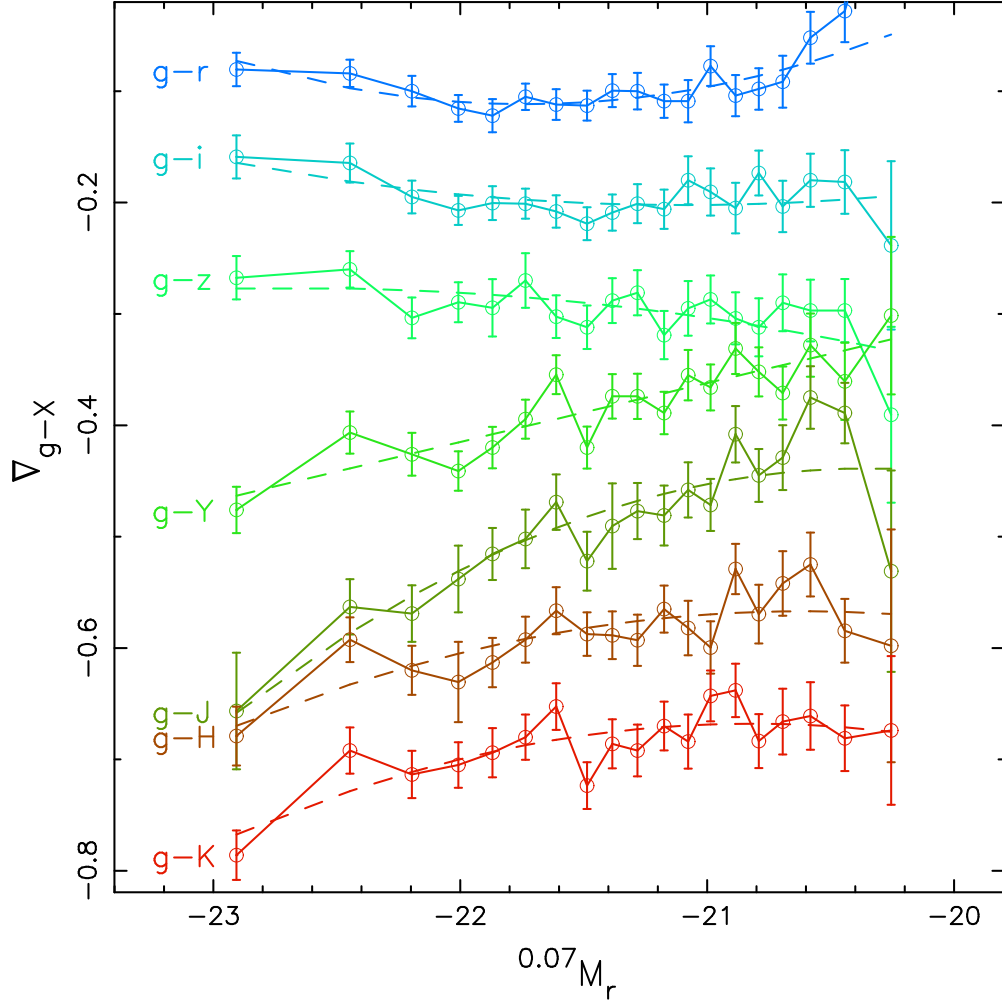


Fig. 13.— Median color gradient,  $\nabla_{g-X}$ , with  $X = rizYJHK$ , as a function of r-band absolute magnitude,  $^{0.07}M_r$ . Error bars denote  $1\sigma$  standard errors on the medians. The dashed lines are obtained by an second-order polynomial fitting of  $\nabla_{g-X}$  versus  $^{0.07}M_r$ , with  $\nabla_{g-X}$  as dependent variable. Different colors correspond to different wavebands, from  $g$  through  $K$  (top to bottom), as indicated by the labels on the left part of the plot. For better displaying the different curves, the  $\nabla_{g-X}$  are re-normalized to have median values of  $-0.1, -0.2, -0.3, -0.4, -0.5, -0.6, -0.7$ , from  $g$  through  $K$ . The actual medians are given by the peak values in Tab. 2.

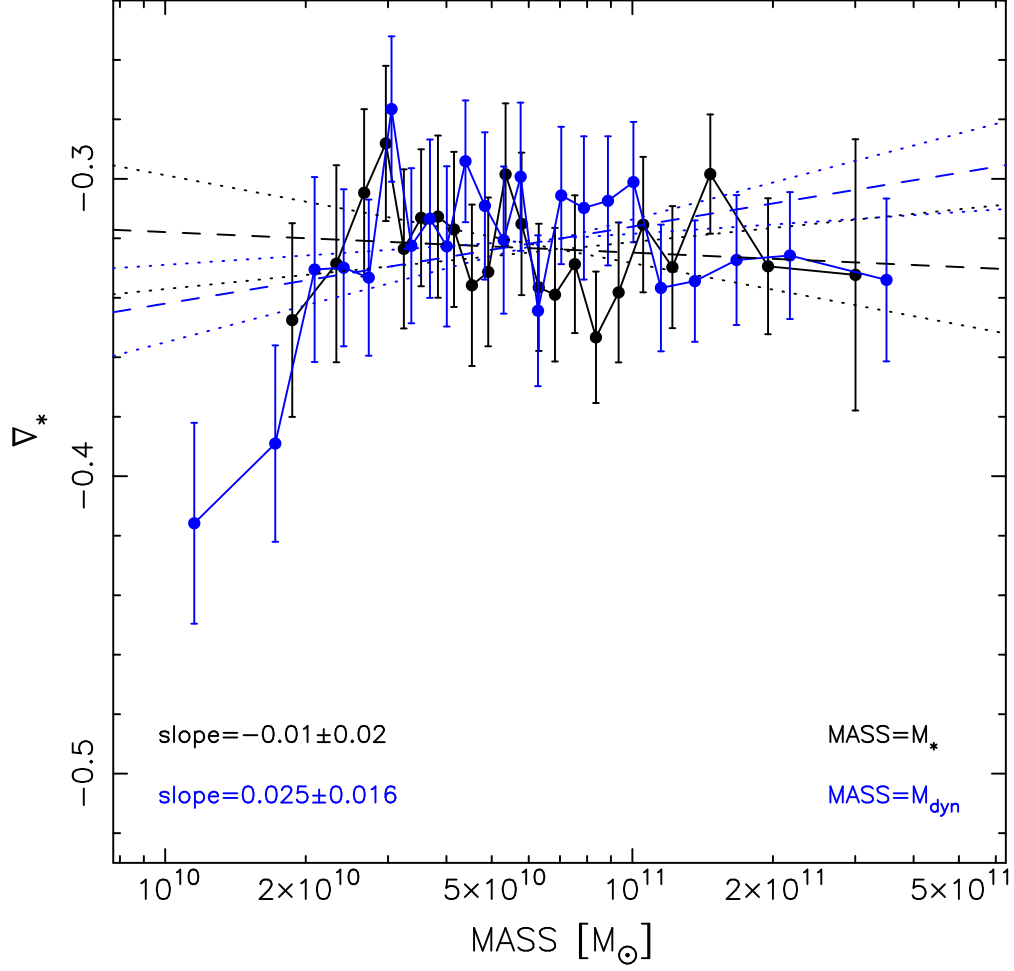


Fig. 14.— Correlation of the median *effective* stellar population gradient,  $\nabla_*$ , with stellar (black) and dynamical (blue) mass, for the optical+NIR sample of ETGs. Error bars denote  $1\sigma$  uncertainties on the median value in each bin. Each bin includes the same number of galaxies ( $N = 200$ ). Dashed lines mark the best-fitting relations, with the corresponding slopes being reported in the lower-left corner of the plot. The dotted lines define  $1\sigma$  confidence contours on the best-fit lines.

below, this inversion in the trend of  $\nabla_\star$  with  $Age$  is caused by galaxies with faint spiral-like morphological features and less accurate structural parameters. The behavior of  $\nabla_\star$  with metallicity is less clear. For the optical sample, the slope of the  $\nabla_\star$  vs.  $[Z/H]$  best-fit relation is larger than zero at over  $7\sigma$ . However, the trend is only weakly detected in the optical+NIR sample, where the slope is only marginally larger than zero, at  $\sim 2.2\sigma$ . We find that  $\nabla_\star$  strongly depends on the  $\alpha$ -enhancement parameter, in the sense that galaxies with larger  $[\alpha/Fe]$  also have shallower effective color gradients. The slope of the best-fitting line is significantly different from zero, at more than  $5\sigma$ , for both the optical and optical+NIR samples.

As discussed in Paper I, the SPIDER sample of ETGs is affected by a small contamination from late-type galaxies with a prominent bulge component. To analyze the impact of this contamination, we define a purer sample of ETGs, where contamination is reduced to at most 5 %. To analyze if the trends of  $\nabla_\star$  with stellar population properties are affected by the presence of late-type contaminants, we define two subsamples of ETGs, by matching the optical and optical+NIR samples with the lower contamination sample of Paper I. We also select only galaxies with better quality structural parameters, by removing objects whose two-dimensional fitting  $\chi^2$  in any of the available wavebands is larger than 1.25 (see Paper I). The optical and optical+NIR subsamples include 3,928 and 31,523 ETGs, respectively. Fig. 16 plots the same trends as in Fig. 15 but for the better quality subsamples. The coefficients of the best-fitting lines of  $\nabla_\star$  vs. age, metallicity, and enhancement, are reported in Tab. 6. The better quality subsamples exhibit trends fully consistent with those obtained for the full samples. In the case of  $\nabla_\star$  vs. age, we do not find that galaxies with younger ages ( $< 4$  Gyr) have flatter gradients, as found for the full samples.

A further issue is that of the fixed aperture size (1.5'' SDSS fiber radius) where the stellar population properties are measured. Because of radial gradients in stellar population properties, this fixed aperture size might produce a correlation of the estimated  $Age$ ,  $[Z/H]$ , and  $[\alpha/Fe]$ , parameters with galaxy radius. Since the  $\nabla_\star$ 's correlate with the (optical)  $R_e$  (see Panel a of Fig. 11), the aperture effect might also bias the correlation of the  $\nabla$ 's with  $Age$ ,  $[Z/H]$ , and  $[\alpha/Fe]$ . However, as shown in App. B, the variation of  $R_e$  along  $\sigma_0$ ,  $Age$ ,  $[Z/H]$ , and  $[\alpha/Fe]$ , is negligible with respect to the full range of  $R_e$  values (Panel a of Fig. 11), implying that the trends in Fig. 15 are not affected at all by the aperture effect.

Table 5. Coefficients of the linear fit of  $\nabla_\star$  versus stellar population properties.

Property	optical+NIR sample		optical sample	
	offset	slope	offset	slope
$\log Age (Gyr)$	$-0.529 \pm 0.058$	$0.227 \pm 0.063$	$-0.714 \pm 0.050$	$0.498 \pm 0.055$
$[Z/H]$	$-0.321 \pm 0.007$	$0.225 \pm 0.100$	$-0.263 \pm 0.004$	$0.430 \pm 0.057$
$[\alpha/Fe]$	$-0.239 \pm 0.016$	$-0.733 \pm 0.125$	$-0.174 \pm 0.010$	$-0.785 \pm 0.086$

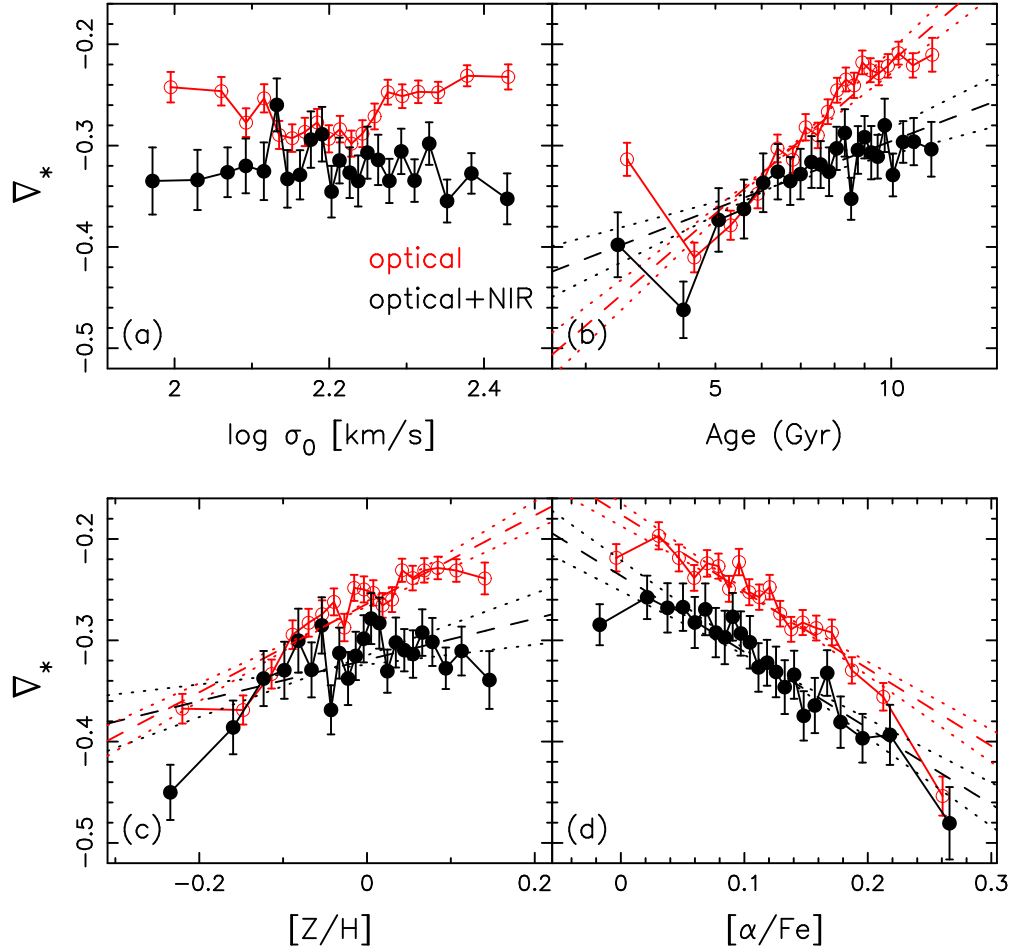


Fig. 15.— The same as Fig. 11 but for the spectroscopic parameters. From left to right and top to bottom, the median  $\Delta_*$  are plotted as a function of the following quantities: the central velocity dispersion (panel a), the luminosity-weighted age (panel b), the luminosity-weighted metallicity (panel c), and the luminosity weighted  $[\alpha/Fe]$  abundance ratio (panel d). The optical+NIR and optical samples of ETGs are plotted with black and red colors, respectively, as shown in the lower-right corner of panel (a).

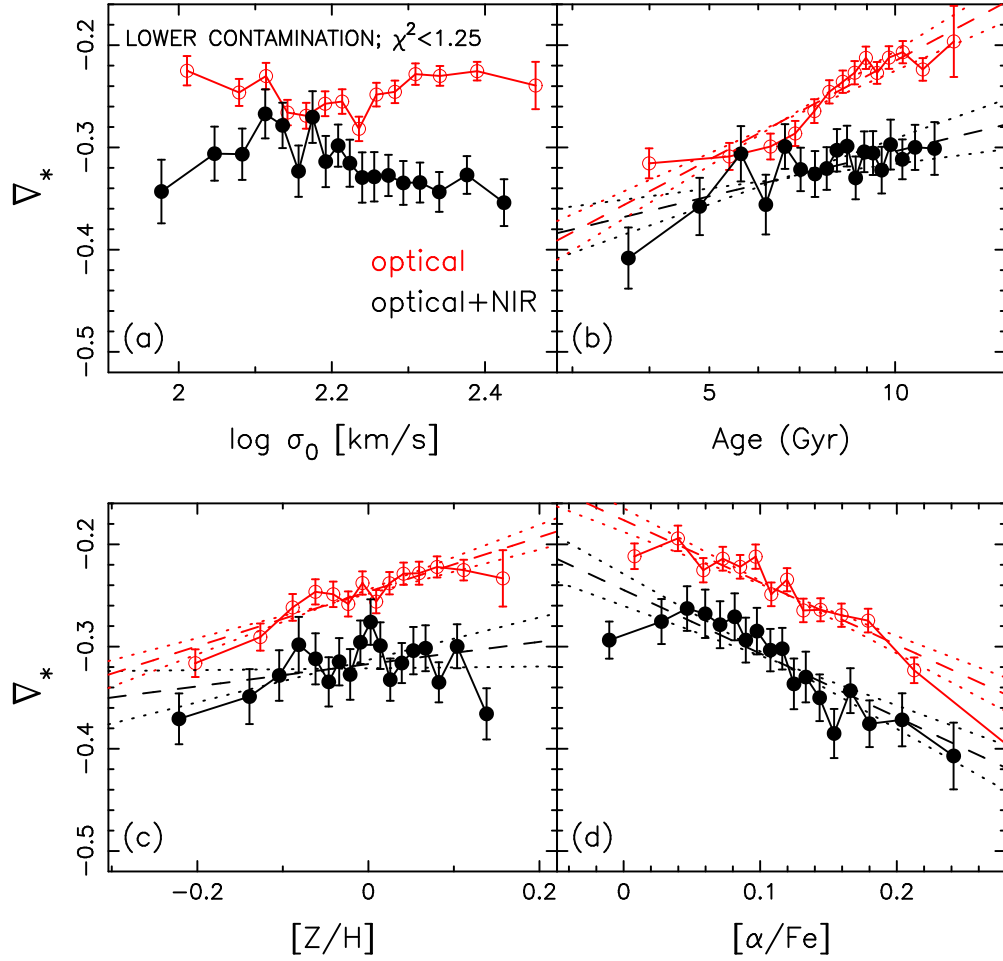


Fig. 16.— The same as Fig. 15 but for the optical+NIR and optical samples of ETGs with lower contamination from galaxies with faint spiral-like morphological features, and lower value of the two-dimensional fitting  $\chi^2$  in r-band ( $\chi^2 < 1.5$ ).

Table 6. The same as Tab. 5 for the samples with lower contamination and better quality of the structural parameters.

Property	optical+NIR sample		optical sample	
	offset	slope	offset	slope
$\log \text{Age (Gyr)}$	$-0.465 \pm 0.062$	$0.159 \pm 0.067$	$-0.539 \pm 0.046$	$0.325 \pm 0.050$
$[Z/H]$	$-0.319 \pm 0.008$	$0.121 \pm 0.101$	$-0.246 \pm 0.005$	$0.269 \pm 0.059$
$[\alpha/Fe]$	$-0.244 \pm 0.017$	$-0.626 \pm 0.130$	$-0.174 \pm 0.012$	$-0.621 \pm 0.094$



## 9. Age versus metallicity gradients in ETGs

In order to separate the contribution of age and metallicity to  $\nabla_\star$ , we restrict the analysis to the optical+NIR sample of ETGs, as optical data alone are completely ineffective at disentangling the two components (see Sec. 6.2). First, we analyze the statistics of the distributions of age and metallicity gradients (Sec. 9.1). Sec. 9.2 deals with the trends of  $\nabla_t$  and  $\nabla_Z$  with respect to different proxies of galaxy mass, as well as stellar population parameters. In Sec. 9.3, the same trends are analyzed separately for low- and high-mass galaxies. In App. D, we also discuss some possible sources of bias in the trends of age and metallicity gradients, such as the role of internal reddening gradients in ETGs.

### 9.1. Statistics of age and metallicity gradients

In Tab. 7, we report the peak of the distributions of age ( $\mu_{\nabla_t}$ ) and metallicity ( $\mu_{\nabla_Z}$ ) gradients for all the stellar population models described in Sec. 7. In agreement with previous works (e.g. Peletier et al. 1990; Tamura & Ohta 2003, 2004; La Barbera et al. 2003), we find that color gradients imply the presence of a negative metallicity gradient in ETGs ( $\nabla_Z < 0$ ), with the outer stellar populations being less metal-rich than the inner ones. The peak value of  $\nabla_Z$  spans the range of  $-0.45$  to  $-0.3$ , depending on the stellar population model. In agreement with our previous work (LdC09), we find that the peak  $\nabla_t$  is significantly greater than zero, i.e. ETGs have on average younger stars in the center than the outskirts.  $\nabla_t$  ranges from  $0.05$  to  $0.2$ , being significantly larger than zero for all models. Hence, as discussed in LdC09, the existence of a small, but significantly positive age gradient is a robust (model-independent) result. From the values of  $\nabla_Z$  and  $\nabla_t$  we see that, for all models, metallicity is the main driver of color gradients.

Table 7. Peak values of the distributions of radial gradients in age ( $\nabla_t$ ) and metallicity ( $\nabla_Z$ ) of ETGs.

model	$\mu_{\nabla_Z}$	$\mu_{\nabla_t}$
<i>BC03</i>	$-0.401 \pm 0.021$	$0.130 \pm 0.023$
<i>M05</i>	$-0.417 \pm 0.017$	$0.198 \pm 0.025$
<i>CB10</i>	$-0.309 \pm 0.010$	$0.052 \pm 0.012$
<i>BC03<math>_{\tau=1Gyr}</math></i>	$-0.456 \pm 0.023$	$0.134 \pm 0.019$

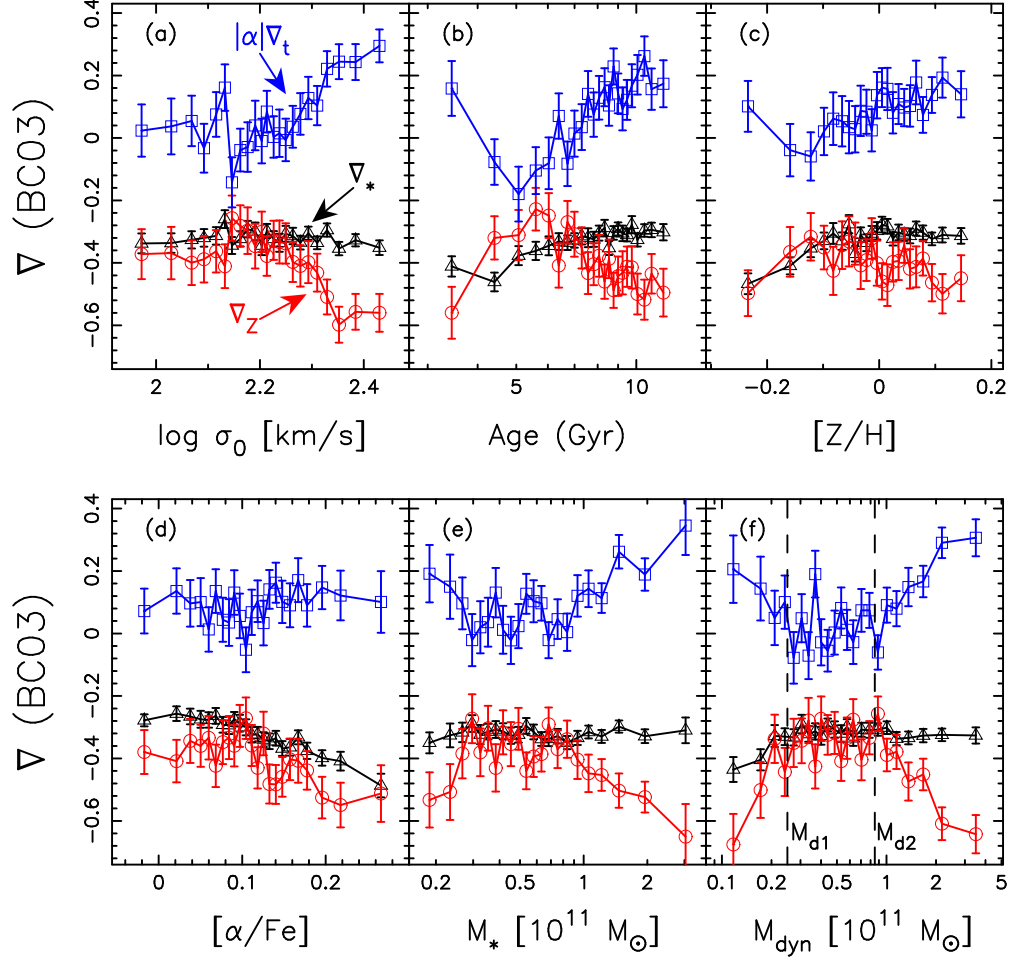


Fig. 17.— Median values of the age (blue) and metallicity (red) gradients in ETGs as a function of (a) central velocity dispersion, (b-d) age, metallicity, and  $[\alpha/Fe]$ , parameters, and (e-f) stellar and dynamical masses. The plots refer to the optical+NIR sample of ETGs. Error bars denote  $1\sigma$  standard errors on the medians. For each bin of a given quantity, the median effective color gradient,  $\nabla_*$ , is also plotted in black color. Age gradients are multiplied by the factor  $\alpha$ , defined in Sec. 7, so that, for each bin, the effective color gradient can be approximately obtained by summing up the age and metallicity gradients in that bin (see Eq. 17). The vertical dashed lines in panel (f) mark the  $M_{dyn}$  used to define the *low-* ( $M_{d1} \leq M_{dyn} \leq M_{d2}$ ) and *high-mass* ( $M_{dyn} > M_{d2}$ ) subsamples of ETGs (see the text).

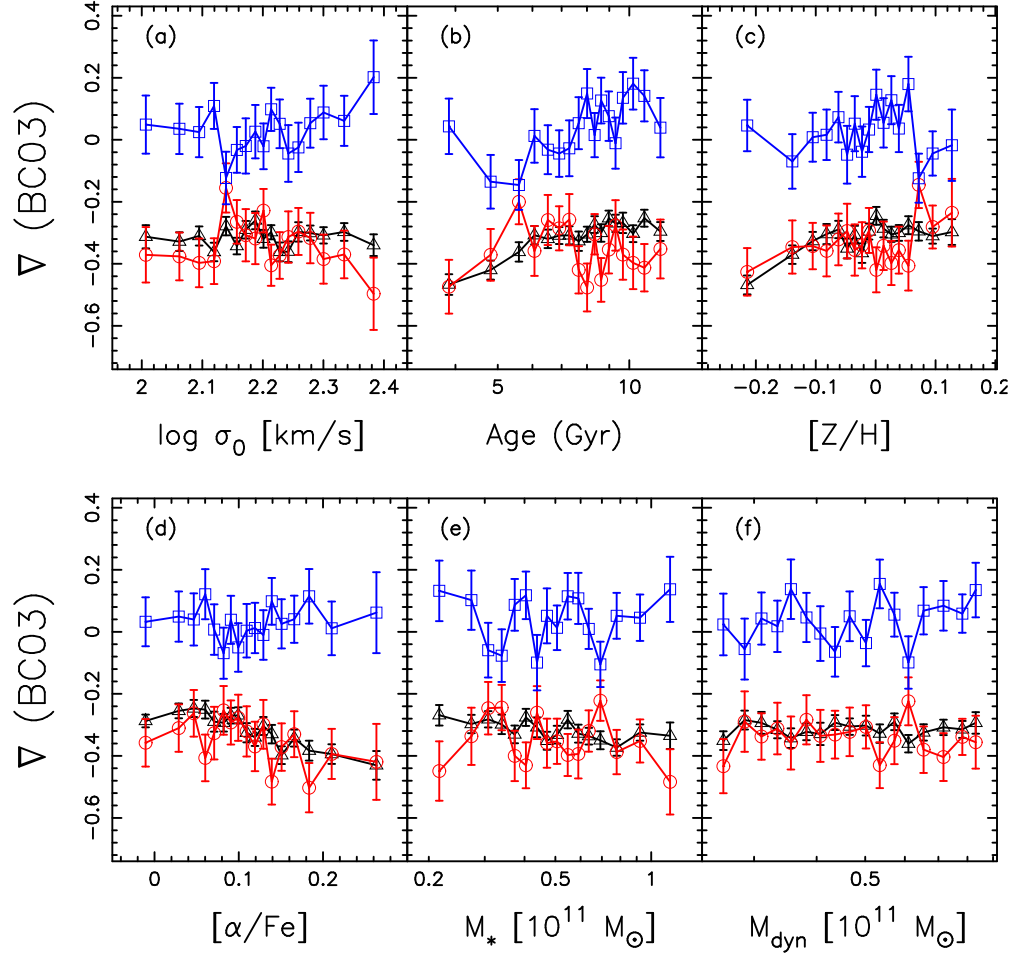


Fig. 18.— The same as Fig. 17 but plotting only galaxies in the *low-mass* bin ( $2.5 \times 10^{10} M_\odot \leq M_{\text{dyn}} \leq 8.5 \times 10^{10} M_\odot$ ).

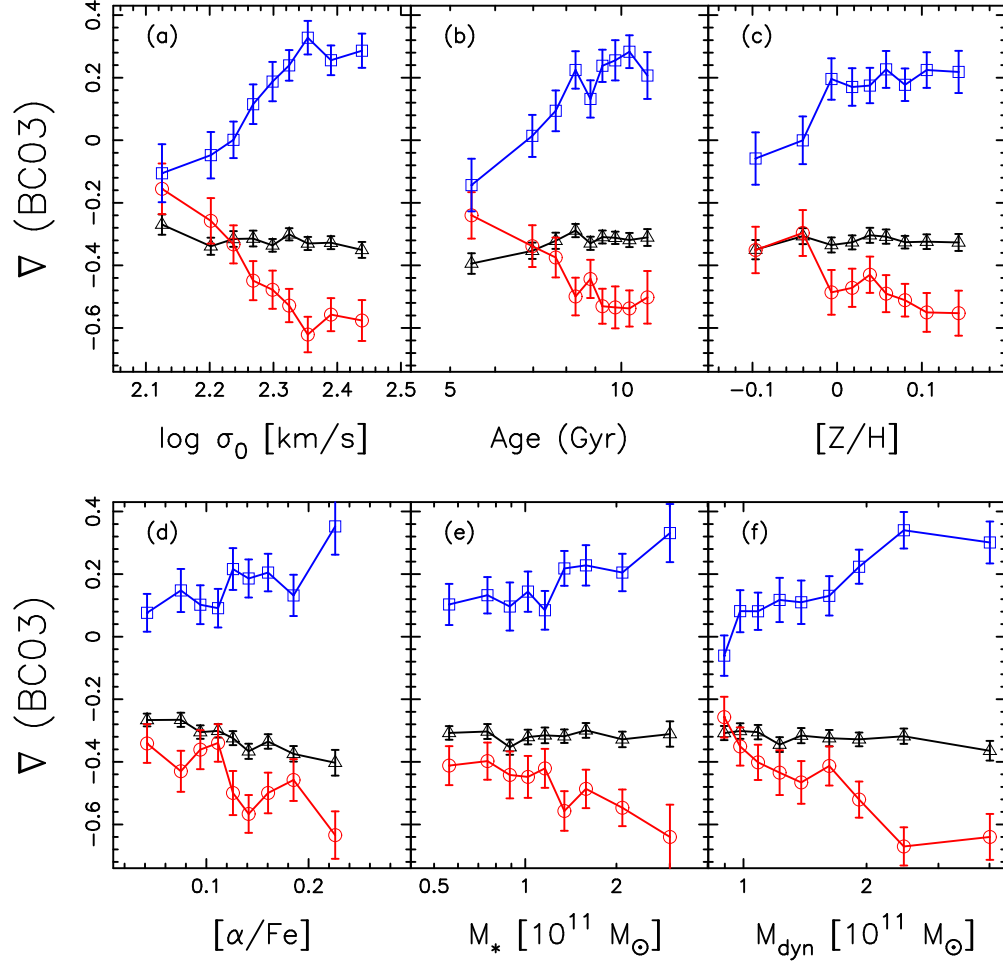


Fig. 19.— The same as Fig. 17 but plotting only galaxies in the *high-mass* bin ( $M_{dyn} > 8.5 \times 10^{10} M_\odot$ ).

## 9.2. Trends of age and metallicity gradients

Fig. 17 plots the median  $\nabla_Z$  (red circles) and  $\nabla_t$  (blue squares) in different bins of stellar population parameters (age, metallicity, and enhancement), velocity dispersion, stellar and dynamical mass. For each bin of a given quantity, we also show the median  $\nabla_*$  in that bin (black triangles).  $\nabla_*$ ,  $\nabla_Z$  and  $\nabla_t$  are estimated using BC03 SSP models. Age gradients are multiplied by the absolute value of the  $\alpha$  parameter (see Sec. 7), so that, for each bin, the sum of age and metallicity gradients gives, approximately<sup>5</sup>,  $\nabla_*$  in that bin (see Eq. 16). This allows us to analyze the relative contribution of age and metallicity to the trends of color gradients *wrt* the different quantities:

### 9.2.1. Trends with mass proxies

For *massive* galaxies, i.e.  $\log \sigma_0 \gtrsim 2.2$  ( $\sigma_0 \sim 160 \text{ km s}^{-1}$ ),  $M_\star \gtrsim 6 \times 10^{10} M_\odot$ , and  $M_{\text{dyn}} \gtrsim 9 \times 10^{10} M_\odot$ , the lack of correlation between  $\nabla_*$  and either  $\sigma_0$ ,  $M_\star$ , or  $M_{\text{dyn}}$  (see Secs. 8.2 and 8.3) is the result of opposing variations of metallicity and age gradients *wrt* such quantities. The  $\nabla_Z$  *decreases* while the  $\nabla_t$  *increases* as the mass proxy increases. The two trends cancel each other in the resulting color gradients. The origin of this opposite behavior is visible in Fig. 13. More luminous (massive) galaxies have flatter optical-optical color gradients (e.g.  $\nabla_{g-r}$ ) and steeper optical-NIR gradients than lower mass systems. Because of the age–metallicity degeneracy, a flatter  $\nabla_{g-r}$  may be due either to a positive age gradient in concert with a negative metallicity gradient, or an intrinsically weaker metallicity gradient. The latter case is excluded by the optical-NIR gradients, as this would make the  $\nabla_{g-K}$  flatten with mass, while we observe the opposite trend. Fig. 17 also shows that low- (relative to high-) mass galaxies exhibit different trends. For  $\log \sigma_0 \lesssim 2.2$  and  $M_\star \lesssim 6 \times 10^{10} M_\odot$ , no significant correlation of  $\nabla_Z$  and  $\nabla_t$  with mass proxy is seen, while for low- $M_{\text{dyn}}$  objects ( $< 9 \times 10^{10} M_\odot$ ) a more complex behavior is observed. To illustrate this, we define two characteristic dynamical masses,  $M_{d1} = 2.5 \times 10^{10} M_\odot$  and  $M_{d2} = 8.5 \times 10^{10} M_\odot$ , marked by the vertical dashed lines in Panel (f) of Fig. 17. For  $M_{\text{dyn}} \gtrsim M_{d2}$  down to  $M_{\text{dyn}} \sim M_{d1}$ , there is no significant correlation of  $\nabla_Z$  and  $\nabla_t$  with  $M_{\text{dyn}}$ , while for  $M_{\text{dyn}} \lesssim M_{d1}$  the metallicity gradient tends to *decrease*, while the age gradient tends to *increase*, as  $M_{\text{dyn}}$  decreases. However, in this mass regime the SPIDER sample becomes incomplete because of the *r*-band magnitude selection (see Sec. 2). We find that all the above trends are essentially unchanged regardless of the stellar population models used to estimate the age and metallicity gradients (see Sec. 7).

---

<sup>5</sup>For each galaxy,  $\nabla_*$  is equal to the sum of age and metallicity gradients, according to Eq. 16. On the other hand, the values of  $\nabla_*$ ,  $\nabla_t$ , and  $\nabla_Z$  in a given bin do not satisfy exactly Eq. 16, as they are obtained by computing the median value of the distributions of  $\nabla_*$ ,  $\nabla_t$ , and  $\nabla_Z$  in that bin.

### 9.2.2. Trends with age

For galaxies older than  $\sim 5$  Gyr, we find that  $\nabla_Z$  decreases, while  $\nabla_t$  increases as a function of the *Age* parameter. The trend of  $\nabla_t$  is stronger than that of  $\nabla_Z$ , making the color gradient,  $\nabla_\star$ , increase with *Age* (see Sec. 8.3). For the M05 and  $BC03_{\tau=1\text{Gyr}}$  models, the behavior of  $\nabla_t$  and  $\nabla_Z$  with *Age* is the same as for BC03 SSP models. On the other hand, for CB10, we find no significant variation of  $\nabla_Z$  with *Age*, while  $\nabla_t$  still increases with the *Age*. This confirms that the trend of color gradients with age, for  $\text{Age} \gtrsim 5$  Gyr, are mainly because of  $\nabla_t$ . For galaxies with  $\text{Age} < 5$  Gyr, the trends of  $\nabla_Z$  and  $\nabla_t$  reverse. Lower ages imply more negative (positive) metallicity (age) gradients. Even in this case, the  $\nabla_t$  dominates the trend, and the resulting color gradient increases as the *Age* decreases. This result holds for all the different stellar population models.

### 9.2.3. Trends with metallicity

For galaxies more metal-rich than  $[Z/H] \sim -0.12$ , the  $\nabla_Z$  tends to decrease, while the  $\nabla_t$  tends to increase as metallicity increases. The two trends cancel each other producing no variation of the median color gradient,  $\nabla_\star$ , as a function of the  $[Z/H]$  parameter, consistent with the  $\nabla_\star$ – $[Z/H]$  slope reported in Tab. 6 for the optical+NIR sample of ETGs. The trends of  $\nabla_Z$  and  $\nabla_t$  seem to reverse at low metallicity, i.e.  $[Z/H] \lesssim -0.12$ , similar to that observed for *Age*. In this regime, the variation of color gradient with  $[Z/H]$  is dominated by  $\nabla_Z$ , which becomes more negative as  $[Z/H]$  decreases. We found the behavior of  $\nabla_t$  and  $\nabla_Z$  with  $Z/H$  to be independent of the adopted stellar population model.

### 9.2.4. Trends with the enhancement

In contrast to the trends with age and metallicity, we do not find any significant variation of  $\nabla_t$  with  $[\alpha/Fe]$ . Fig. 17 reveals that the strong correlation of  $\nabla_\star$  with enhancement is because of the metallicity gradient decreasing with  $[\alpha/Fe]$ .

## 9.3. Low- and high-mass ETGs

Since the trend of age and metallicity gradients *wrt* different mass proxies depends on the range of galaxy mass, we bin the sample of ETGs according to  $M_{\text{dyn}}$ , and analyze the trends of  $\nabla_Z$  and  $\nabla_t$  in each bin. We define two bins, including *low*- ( $M_{d1} < M_{\text{dyn}} < M_{d2}$ ), and *high*-mass ( $M_{\text{dyn}} \geq M_{d2}$ ) galaxies, where  $M_{d1}$  and  $M_{d2}$  are defined above. Although the sample of

ETGs becomes incomplete at  $M_{dyn} \lesssim 3 \times 10^{10} M_{\odot}$ , we adopt a slightly lower mass limit of  $M_{dyn} \sim 2.5 \times 10^{10} M_{\odot}$ , as this is approximately the  $M_{dyn}$  at which the trend of  $\nabla_t$  and  $\nabla_Z$  with mass changes behavior (see Panel f of Fig. 17).

Figs. 18 and 19 are the same as Fig. 17, but plot only galaxies in the low- and high-mass bins, respectively. In order to quantify the trends of  $\nabla_t$ ,  $\nabla_Z$ , and  $\nabla_{\star}$  wrt a given parameter, we fit each trend with a linear relation, minimizing the sum of absolute residuals of median gradients (see Sec. 8.1). The slopes and their uncertainties are reported in Tabs. 8 and 9 for the low- and high-mass bins, respectively. From Figs. 18 and 19, as well as Tabs. 8 and 9, we see that:

- *Low-mass.* The *effective* color gradient,  $\nabla_{\star}$ , does not show any significant correlation with either  $\sigma_0$  or  $M_{dyn}$ , while it tends to marginally decrease with stellar mass, as the  $\nabla_{\star}-M_{\star}$  slope in Tab. 8 is less than zero ( $-0.12 \pm 0.05$ ) at the  $2.2 \sigma$  confidence level. No significant trend of  $\nabla_Z$  and  $\nabla_t$  is detected wrt any mass proxy ( $M_{dyn}$ ,  $M_{\star}$ , and  $\sigma_0$ ). On the other hand, for stellar population parameters, we find that  $\nabla_{\star}$  strongly correlates with *Age* and  $[\alpha/Fe]$ . The *effective* color gradient increases for larger *Age*, and becomes more negative as the  $[\alpha/Fe]$  increases. The slopes of the  $\nabla_{\star}-Age$  and  $\nabla_{\star}-[\alpha/Fe]$  linear fits differ from zero at more than  $4 \sigma$ , proving that the trends are highly significant. The  $\nabla_{\star}$  also tends to increase with metallicity, but the slope of the  $\nabla_{\star}-[Z/H]$  fit is larger than zero at only  $2.2 \sigma$ . As noted above, the trend of  $\nabla_{\star}$  with *Age* is mainly due to  $\nabla_t$ , while that with  $[\alpha/Fe]$  is driven by  $\nabla_Z$ .
- *High-mass.* For high-mass galaxies, the *effective* color gradient does not vary significantly with *Age*, metallicity nor with any mass proxy. In fact, the slopes of the correlations involving  $\nabla_{\star}$  in Tab. 9 are all consistent with zero at less than  $2 \sigma$ . For the  $[\alpha/Fe]$ , there is a significant trend of  $\nabla_{\star}$  decreasing as the enhancement increases. The slope of the  $\nabla_{\star}-[\alpha/Fe]$  linear fit ( $-0.84 \pm 0.2$ ) differs from zero at over  $4 \sigma$ , and is consistent with that obtained for low-mass ETGs ( $-0.68 \pm 0.17$ , see Tab. 8) and for the entire sample ( $-0.73 \pm 0.13$ , see Tab. 5). For all quantities, we find anti-correlated variations of  $\nabla_Z$  and  $\nabla_t$ , which cancel each other in the trends of  $\nabla_{\star}$ . For  $[\alpha/Fe]$ , the metallicity gradient dominates, resulting in the strong correlation of  $\nabla_{\star}$  and  $[\alpha/Fe]$ .

From Figs. 17, 18 and 19, we see that positive age gradients in ETGs are more associated with high rather than low mass galaxies. At high mass, the age gradient strongly increases as a function  $\sigma_0$ ,  $M_{dyn}$ , and to a lesser extent with stellar mass, while these trends are not observed for low-mass galaxies. However, for both low- and high-mass,  $\nabla_t$  becomes significantly positive for galaxies older than  $\sim 7$  Gyr. This implies that age gradients in ETGs are mainly driven by mass, and only secondarily by *Age*. Panel (b) of Fig. 17 also shows that for *Age*  $< 5$  Gyr, the trend of  $\nabla_t$  with *Age* reverses: the younger the age, the more positive the age gradient becomes. Consistent with the downsizing picture (Cowie et al. 1996), galaxies at *Age*  $< 5$  Gyr are low-mass systems, as shown

by the inversion in the  $\nabla_t$ -*Age* trend being observed only for the low-mass bin (Panel b of Fig. 18).

Stellar population parameters, such as *Age*, metallicity, and enhancement, are known to correlate with proxies of galaxy mass, such as velocity dispersion and stellar mass (see e.g. Thomas et al. 2005; Nelan et al. 2005; Gallazzi et al. 2006). Since for high-mass galaxies we find that internal gradients correlate with both mass and stellar population properties, a natural question is if these trends are just because of the correlation among stellar population properties and mass. In order to address this issue, we apply a correction procedure that *removes* the correlations of each  $\nabla$  quantity with mass from all the trends in Figs. 18 and 19. The procedure is illustrated in Fig. 20, where we show how the trends of the  $\nabla$ 's *wrt* to  $[Z/H]$  are corrected, for galaxies in the high-mass bin:

- i. First, we model the  $\nabla$ 's- $M_{dyn}$  trends with third order polynomials in  $M_{dyn}$  (dashed curves in the top panel);
- ii. We compute the median  $M_{dyn}$  in each bin of  $[Z/H]$  (mid panel). As expected from the  $[Z/H]$ -mass correlation (e.g. Thomas et al. 2005), the mass increases as  $[Z/H]$  increases;
- iii. In each bin of  $[Z/H]$ , using the corresponding median  $M_{dyn}$ , we calculate the expected values of  $\nabla_*$ ,  $\nabla_Z$ , and  $\nabla_t$  from the best-fit polynomials;
- iv. The expected  $\nabla$ 's in each  $[Z/H]$  bin are subtracted from the measured  $\nabla$  in that bin; the subtracted values are re-normalized, by suitable additive terms, to the medians of the  $\nabla_*$ ,  $\nabla_Z$ , and  $\nabla_t$  distributions (bottom panel in Fig. 20). Comparing top and bottom panels in Fig. 20 illustrates how the correction procedure (partly) removes the correlations of  $\nabla_*$ ,  $\nabla_Z$ , and  $\nabla_t$  with  $[Z/H]$ .

We apply this correction scheme for both low- and high-mass ETGs, modeling the  $\nabla$ 's- $M_{dyn}$  trends (point i. above) independently for each case. We obtain the following results:

- *High-mass.* Fig. 21 exhibits the correlations of  $\nabla_*$ ,  $\nabla_Z$ , and  $\nabla_t$ , with different quantities, for high-mass galaxies ( $M_{dyn} \geq M_{d2}$ ), *after removing* the  $\nabla$ 's- $M_{dyn}$  trends. By construction, the procedure removes the correlations of the  $\nabla$ 's with  $M_{dyn}$  (Panel f). However, it does not impact the trends involving stellar population properties. This is because such trends are due to the  $\nabla - \sigma_0$  correlations (rather than  $\nabla$ 's- $M_{dyn}$ ). This is shown in Fig. 22, where we repeat the entire procedure by removing the  $\nabla$ 's- $\sigma_0$  trends. The  $\nabla$ 's- $\sigma_0$  corrections remove all the trends, with the remarkable exception of the correlations among  $\nabla_*$  ( $\nabla_Z$ ) and the enhancement. A linear fit to the  $\nabla_*$ - $[\alpha/Fe]$  trend in Fig. 22 gives a slope of  $-0.8 \pm 0.2$ , still fully consistent with that of the uncorrected trend ( $-0.84 \pm 0.19$ , see Tab. 9).



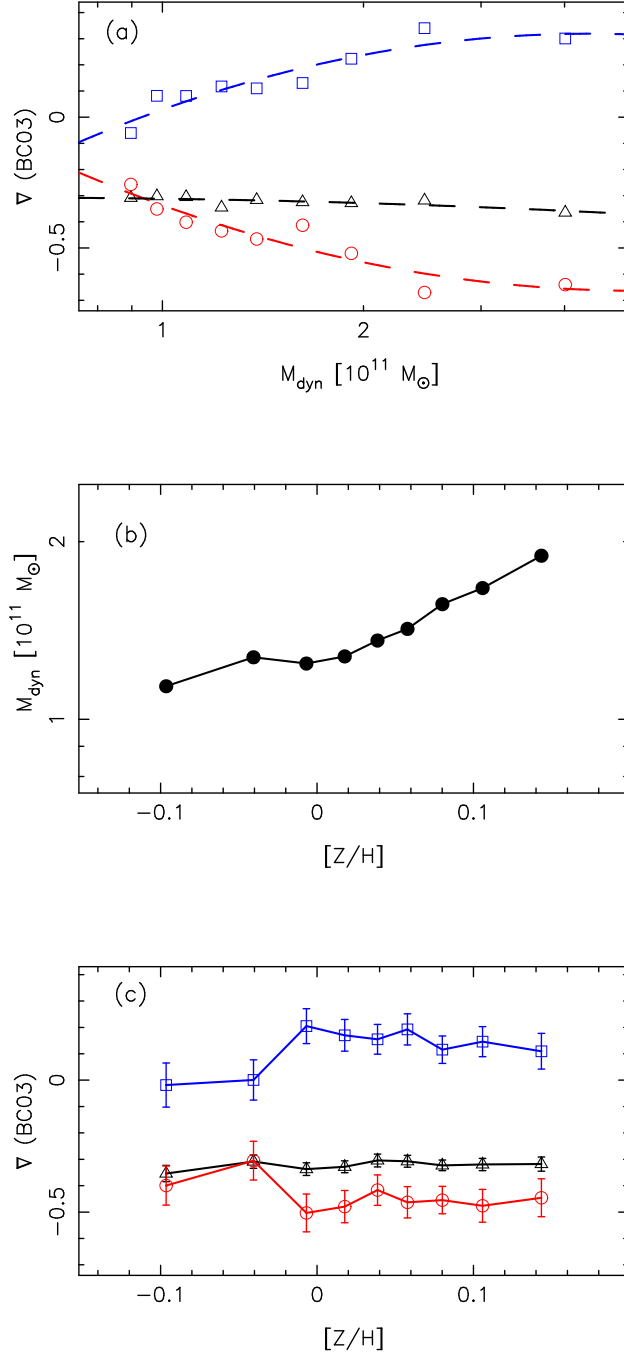


Fig. 20.— Example of the correction procedure adopted to remove the correlation among the  $\nabla$ 's and dynamical mass from the trends of  $\nabla_{\star}$ ,  $\nabla_Z$ , and  $\nabla_t$ , wrt galaxy parameters (Figs.18 and 19). Top panel plots the  $\nabla$ 's as a function of  $M_{\text{dyn}}$  for high-mass galaxies. Different symbols are the same as in panel (f) of Fig. 19. Dashed curves are third-order polynomial fits to the data. The mid panel plots the median value of  $M_{\text{dyn}}$  in different bins of metallicity,  $[Z/H]$ . Metallicity bins as the same as for panel (b) of Fig. 19. The bottom panel shows the results of the correction procedure: for each metallicity bin, the polynomial fits are used to estimate the expected  $\nabla$ 's in that bin. The expected  $\nabla$ 's are subtracted from the data-points in the top panel. The resulting values are re-normalized, by suitable additive terms, to match the median values of the  $\nabla_{\star}$ ,  $\nabla_Z$ , and  $\nabla_t$  distributions.

– *Low-mass*. In the mass range of  $M_{d1}$  to  $M_{d2}$ , there is no variation of  $\nabla_\star$  with velocity dispersion or dynamical mass. Hence, the correlations between gradients and stellar population parameters can not arise from age, metallicity, and enhancement varying with mass. However, at a given  $\sigma_0$ , the stellar population parameters are correlated with each other, with age being anti-correlated with both metallicity and enhancement (Graves et al. 2009). To account for this, we re-derive the trends between the  $\nabla$ ’s and other parameters by removing the correlations with the *Age*. The procedure is the same as that adopted to remove the  $\nabla$ ’s- $M_{dyn}$  and  $\nabla$ ’s- $\sigma_0$  correlations for high-mass galaxies (see above). Fig. 23 shows the same plots as Fig. 18, but after the  $\nabla$ ’s-*Age* trends are removed. We see that this correction does not affect significantly the correlations of the  $\nabla$ ’s *wrt* metallicity and enhancement. In particular, after the correction is applied, a linear fit of  $\nabla_\star$  *wrt*  $Z/H$  gives a slope of  $0.29 \pm 0.12$ , fully consistent with that of  $0.33 \pm 0.15$  reported in Tab. 8. For  $\nabla_\star$  versus  $[\alpha/Fe]$ , the slope is  $-0.59 \pm 0.15$ , still consistent with that in Tab. 8 ( $-0.84 \pm 0.19$ ). It follows that, for low-mass systems, all the correlations of internal gradients with stellar population parameters are independent of each other, i.e. the gradients exhibit a genuine correlation with each single parameter (in particular age and enhancement).

## 10. Summary

In this paper, we examined a sample of 4,546 ETGs with *grizYJHK* data available. We consider an ETG to be a bulge-dominated galaxy with a passive spectrum in its central region (within the SDSS fiber). As such, the results obtained here do not apply exclusively to ellipticals, but to S0 galaxies and galaxies with a red central bulge (although the effect of late-type contaminants is expected to be negligible, see Secs. 3.3 and 8.3). However, there is no a priori reason to expect that the formation mechanisms and evolutionary pathways are the same for all sub-classes of what we

Table 8. Slopes of the linear fits of median  $\nabla_t$  (col. 2),  $\nabla_\star$  (col. 3), and  $\nabla_z$  (col. 3), as a function of different galaxy parameters. Each line in the table corresponds to a different parameter, as reported in col. 1. The slopes refer to the sample of ETGs in the *low-mass* bin.

	$\nabla_t$	$\nabla_\star$	$\nabla_z$
$\log \sigma_0$	$0.18 \pm 0.25$	$0.050 \pm 0.104$	$-0.16 \pm 0.24$
<i>Age</i> (Gyr)	$0.59 \pm 0.25$	$0.406 \pm 0.091$	$-0.10 \pm 0.21$
$[Z/H]$	$-0.02 \pm 0.30$	$0.338 \pm 0.151$	$0.33 \pm 0.27$
$[\alpha/Fe]$	$0.16 \pm 0.37$	$-0.681 \pm 0.165$	$-0.48 \pm 0.38$
$M_\star [10^{11} M_\odot]$	$-0.01 \pm 0.17$	$-0.111 \pm 0.055$	$-0.05 \pm 0.15$
$M_{dyn} [10^{11} M_\odot]$	$0.19 \pm 0.16$	$0.009 \pm 0.068$	$-0.13 \pm 0.16$

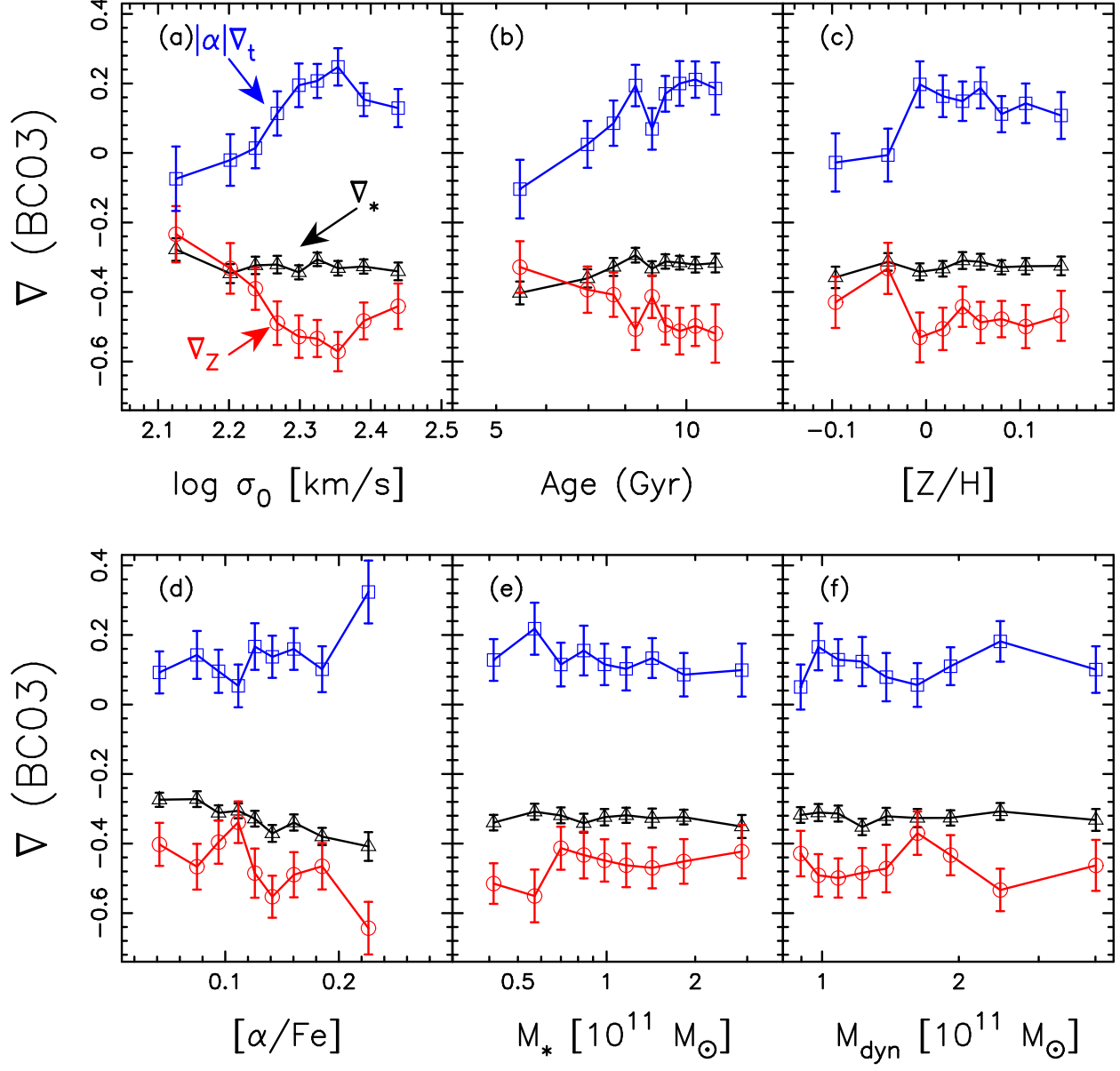


Fig. 21.— The same as Fig. 19 but correcting the  $\Delta$  in each panel for the correlations with dynamical mass.

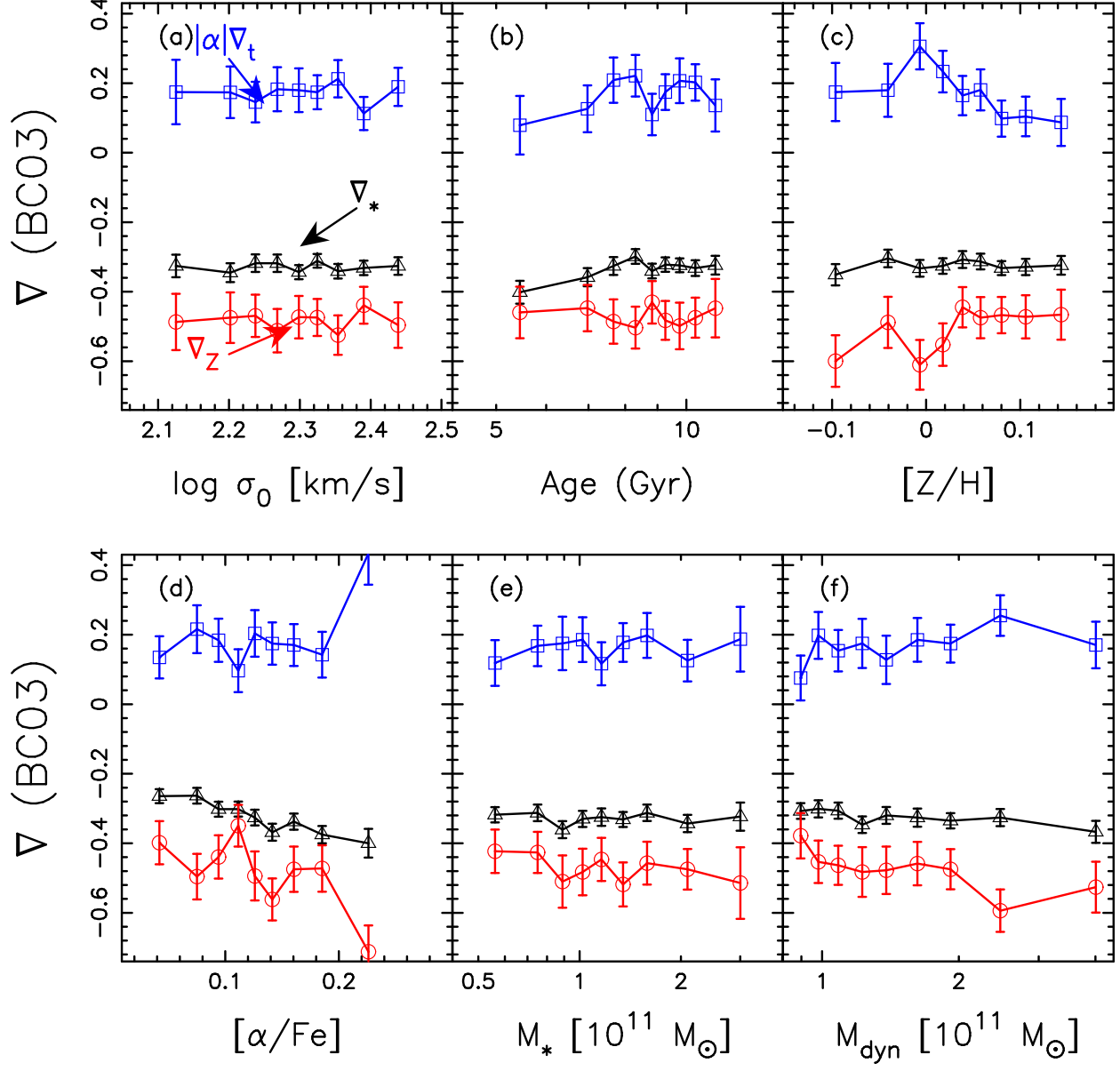


Fig. 22.— The same as Fig. 19 but correcting the  $\nabla$  in each panel for the correlations with  $\sigma_0$ . Note how the correction removes all the correlations but those with the  $\alpha$ -enhancement.

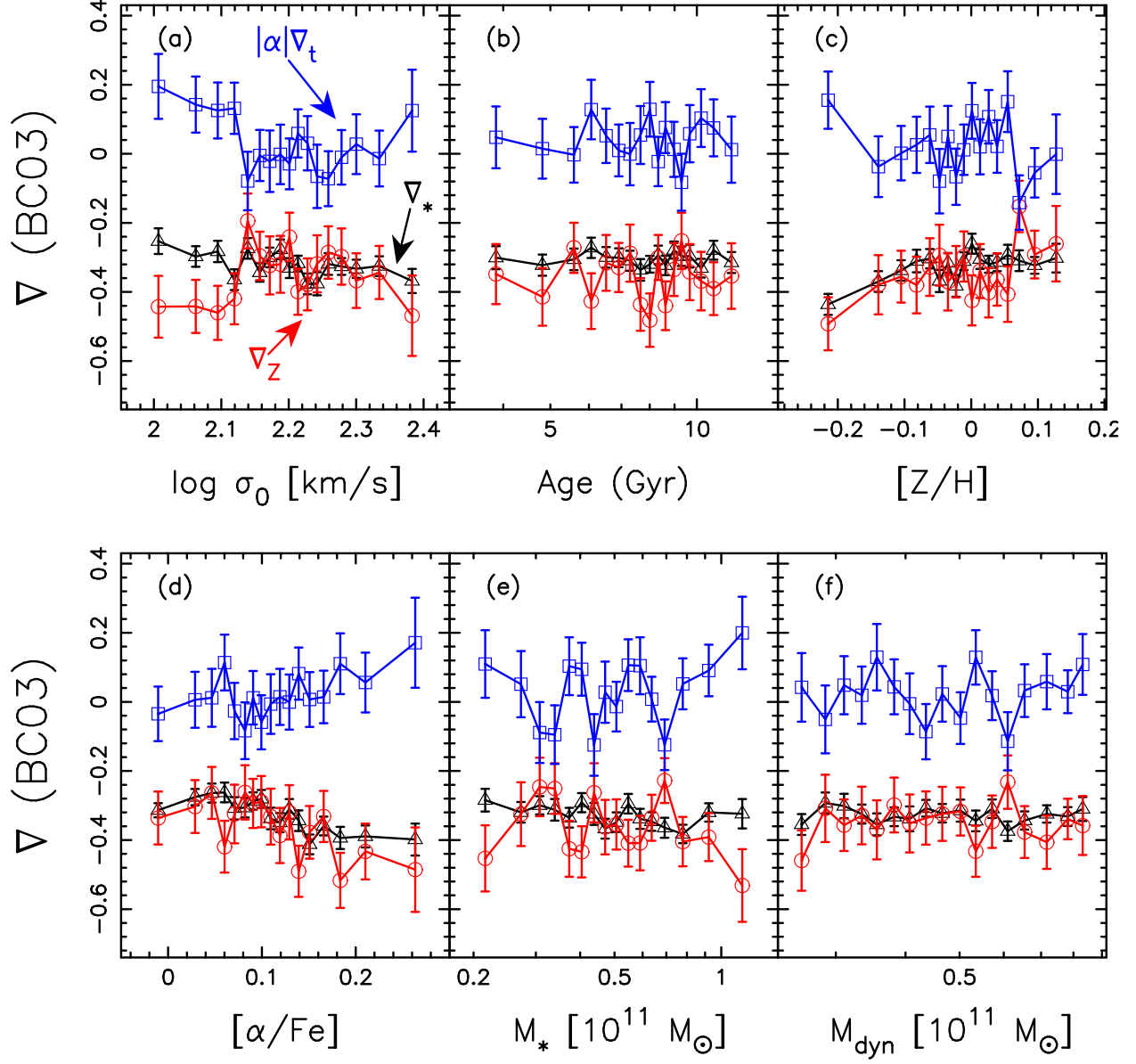


Fig. 23.— The same as Fig. 18 but correcting the  $\nabla$  in each panel for the correlations with the *Age* parameter.

call ETGs.

We measured structural parameters in all wavebands and stellar population indicators from the spectra. We describe a new approach to constrain age and metallicity gradients from the color information. Also, we define an effective color gradient,  $\nabla_{\star}$ , that uses all the color terms provided by the photometric data and investigate its dependence on several parameters like age, metallicity, mass and  $[\alpha/Fe]$ . Although the estimate of stellar population parameters (Sec. 3.3) and that of stellar masses and age/metallicity gradients rely on different stellar population models (BC03 vs. MILES), we find that all trends shown here remain unchanged when using a variety of population synthesis models to infer the gradients and estimate stellar masses. In the following we summarize our main findings:

- 1) We present a new scheme to quantify stellar population gradients from color gradients. We introduce an effective color gradient,  $\nabla_{\star}$ , which reflects all contributions from the optical+NIR colors.  $\nabla_{\star}$  correlates well with all color gradients measured independently (as expected) and is model independent, while  $\nabla_Z$  and  $\nabla_t$  (i.e. the metallicity and age gradients) are not.
- 2) For photometric properties, we find that  $\nabla_{\star}$  has a mild correlation with the Sersic index; does not change at all with the axis ratio; and strongly correlates with total galaxy color - systems with bluer colors tend to have more negative  $\nabla_{\star}$ . Using optical+NIR data we also find that larger and more luminous ETGs have more negative  $\nabla_{\star}$ 's, although if we restrict ourselves to only  $K$ -band data,  $\nabla_{\star}$  shows no dependence on radius or luminosity.
- 3) For galaxies more massive than  $M_{dyn} > 8.5 \times 10^{10} M_{\odot}$ , the age gradient increases, while the metallicity gradient decreases as functions of mass, age, metallicity, and enhancement. The trends cancel each other in the color gradient, with the exception of those for the enhancement: the color gradient decreases as a function of  $[\alpha/Fe]$ . All trends are a consequence of the correlations of the  $\nabla$ 's *wrt* both velocity dispersion and  $[\alpha/Fe]$ . These parameters are the main drivers of the internal age, metallicity, and color gradients in massive ETGs.

Table 9. The same as Tab. 8 but for galaxies in the *high-mass* bin.

	$\nabla_t$	$\nabla_{\star}$	$\nabla_Z$
$\log \sigma_0$	$1.51 \pm 0.24$	$-0.193 \pm 0.129$	$-1.53 \pm 0.31$
$Age(Gyr)$	$1.54 \pm 0.33$	$0.229 \pm 0.132$	$-1.05 \pm 0.30$
$[Z/H]$	$1.26 \pm 0.42$	$0.006 \pm 0.165$	$-0.98 \pm 0.37$
$[\alpha/Fe]$	$1.00 \pm 0.54$	$-0.756 \pm 0.190$	$-1.36 \pm 0.45$
$M_{\star}[10^{11} M_{\odot}]$	$0.26 \pm 0.13$	$-0.020 \pm 0.052$	$-0.26 \pm 0.13$
$M_{dyn}[10^{11} M_{\odot}]$	$0.56 \pm 0.15$	$-0.082 \pm 0.060$	$-0.55 \pm 0.15$

- 4) For less massive galaxies,  $2.5 \times 10^{10} M_{\odot} \leq M_{\text{dyn}} \leq 8.5 \times 10^{10} M_{\odot}$ , no strong correlation of age, metallicity, and color gradients is detected *wrt* mass. However, color gradients strongly correlate with stellar population parameters, and these correlations are independent of each other.
- 5) In both mass regimes, there is a strong anti-correlation between the color gradient and  $\alpha$ -enhancement, that originates from the metallicity gradient decreasing with  $[\alpha/Fe]$ . This could result from the star formation and metallicity enrichment being regulated by the interplay between the input of energy from supernovae, and the temperature and pressure of the hot X-ray gas in ETGs.
- 6) In both mass regimes, positive age gradients are associated with old galaxy ages ( $> 5 - 7$  Gyr). For galaxies younger than  $\sim 5$  Gyr, mostly at low-mass, the age gradient tends to be anti-correlated with the Age parameter, with more positive gradients at younger ages.

We have studied the correlation of color gradients in ETGs with intrinsic galaxy properties, using an extensive sample, with excellent photometric and spectroscopic data over a broad wavelength baseline, and state-of-the-art analysis methods. However, even with such tools and data at our disposal, it remains difficult to gain substantive insight into the details of how galaxies actually form. The diagnostic value of color gradients will only become fully apparent when model predictions become sufficiently specific to realize the full potential of the high quality observational data and methods developed to estimate color gradients.

### A. The $\alpha$ -MILES models

The  $\alpha$ -MILES SSP models are constructed as described in Cervantes et. al. (2007), using both empirical and theoretical stellar libraries. The empirical libraries, like MILES (Sanchez-Blazquez et al. 2006), contain spectra of stars in the solar neighborhood, but mostly lack bulge-stars, with non-solar abundance ratios. Hence, they do not allow a detailed spectral modeling of metal-rich, alpha-enhanced systems, such as bright ETGs. The  $\alpha$ -MILES models complement the empirical libraries, in the non-solar abundance regime, with the synthetic library of Coelho et al. (2005), consisting of high-resolution synthetic stellar spectra covering a wide range of stellar atmosphere's parameters. The Coelho et al. (2005) library covers both solar and alpha-enhanced mixtures in a wide baseline, from 3000 Å to 1.4  $\mu\text{m}$ , superseding previous versions by Barbuy et al. (2003), in the wavelength range 4600-5600 Å, and Zwitter et al.(2004), in the range 7653-8747 Å. The resulting  $\alpha$ -enhanced models consist of SED's covering the same spectral range (3525 – 7500 Å), with the same spectral resolution (2.3 Å), as the (solar abundance) MILES library. The  $\alpha$ -MILES consists of 1,170 SSPs, corresponding to: twenty-six ages from 1 to 18 Gyr; five  $[Z/H]$  from

–1.28 to +0.2, and nine  $[\alpha/Fe]$  abundance ratios from –0.2 to +0.6. From this set of models, we run STARLIGHT by extracting a sub-set of 176 SSPs (see Sec. 3.3).

According to our tests, these preliminary alpha-enhanced models are clearly more efficient in fitting the ETG’s spectra *wrt* to the solar-scale counterparts. For a subsample of 1,000 ETGs in the SPIDER sample, we have compared the quality of the STARLIGHT spectral fitting when using either solar-abundance or  $\alpha$ -MILES SSPs. The fitting quality is measured, for each galaxy, by using: (1) the reduced  $\chi^2$  of the fitting,  $\chi^2/N_{\lambda_{eff}}$ , where  $N_{\lambda_{eff}}$  is the number of  $\lambda$  values used in the fit minus the number of fitting parameters; and (2) the percentage mean deviation,  $\langle dev \rangle$ , over all the fitted pixels between the input and synthetic spectrum. The  $\langle dev \rangle$  is computed by taking the mean of  $|Obs_{\lambda} - Syn_{\lambda}|/Obs_{\lambda}$ , where  $Obs_{\lambda}$  and  $Syn_{\lambda}$  are the fluxes of the observed and synthetic spectrum at a given wavelength  $\lambda$ , over the spectral interval 4320-6800 Å. We found that the reduced  $\chi^2$  decreases by 0.1 when using the alpha-enhanced models. The improvement in fit quality is illustrated in Fig. 24. Left panel shows, as an example, the synthetic spectra obtained for a given ETG, in a small spectral interval including the *Mgb* and *Fe5270* features, when using either solar (blue) or  $\alpha$ -MILES (red) models. Although both models well describe the *Fe*, only the  $\alpha$ -MILES synthetic spectrum (red) is able to reproduce also the *Mg* region. Right panel of Fig. 24 compares the  $\langle dev \rangle$  parameters between solar and alpha-enhanced synthetic spectra. The  $\alpha$ -MILES models provide a mean percentage deviation smaller than that obtained from the solar models by a factor of  $\sim 2$ .

As a further test, we compared the solar MILES models with the  $\alpha$ -MILES models having  $[\alpha/Fe] = 0$  (i.e., we compared the models which use the empirical stellar spectra with those using synthetic ones, in the regime where both models should give the same answer). Fig. 25 plots the distribution of luminosity-weighted  $[\alpha/Fe]$ , obtained by running STARLIGHT with a *basis* of  $\alpha$ -MILES SSPs on different solar-MILES SSP models (see Sec. 3.3). We considered a total of 84 solar models with a variety of ages (in 21 steps from 1 to 17.8 Gyr) and metallicities ( $[Z/H] = -0.68, -0.38, 0., 0.2$ ). For each solar model, STARLIGHT was run with a *basis* of 220  $\alpha$ -MILES SSP models, covering the same range in age and metallicity as for the analysis of SDSS spectra (Sec. 3.3), and  $[\alpha/Fe] = -0.2, 0, +0.2, +0.4, +0.6$ . The distribution of luminosity-weighted  $[\alpha/Fe]$  in Fig. 25 is sharply peaked around zero, with a width less than  $\sim 0.01$ , proving the consistency of solar- and  $\alpha$  models for the case of solar abundance ratio.

## B. Aperture corrections and color gradients.

Since the  $\nabla_{\star}$ ’s correlate with the (optical)  $R_e$  (see Panel a of Fig. 11), the fixed size of SDSS spectra might affect the correlation of the  $\nabla$ ’s with *Age*,  $Z/H$ , and  $[\alpha/Fe]$ . To address this issue, we show in Fig. 26 the median galaxy effective radius in different bins of  $\sigma_0$ , *Age*,  $Z/H$ , and  $[\alpha/Fe]$ ,



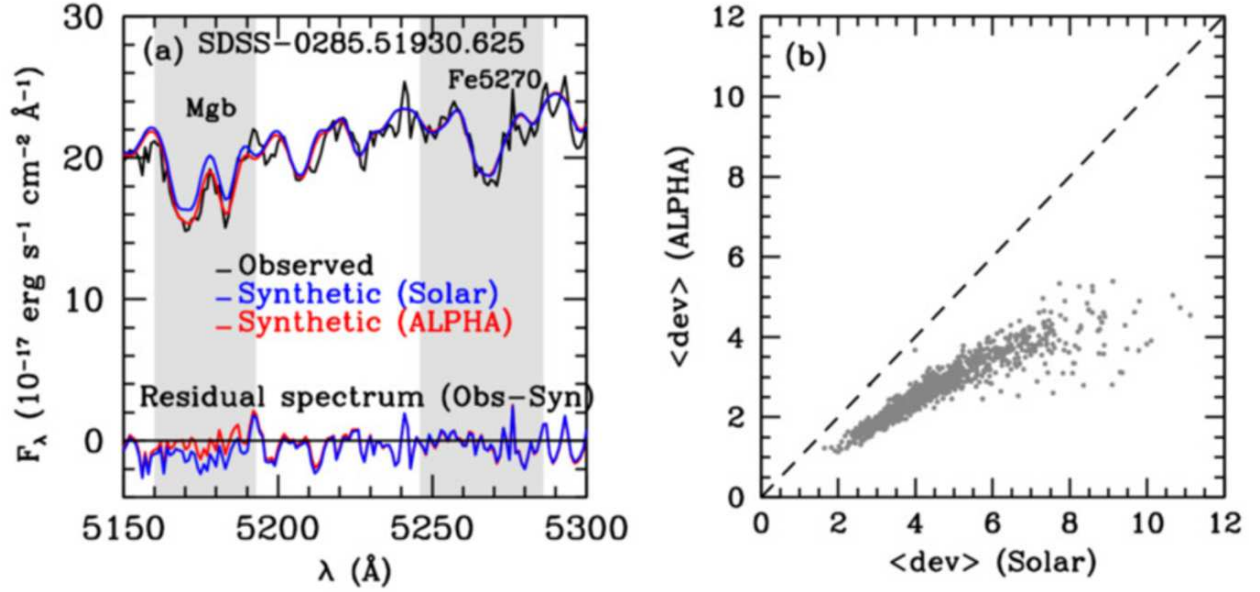


Fig. 24.— Performance of solar-abundance and  $\alpha$ -MILES models to model the spectra of bright ETGs. (a) The spectrum of one ETG is shown, as example, in black color over a small spectral interval, including both *Mgb* and *Fe5270* features (gray bands in the plot). The *Mgb* index is well reproduced only by the alpha-enhanced models (red), as also seen in the residual spectrum (lower part of the plot). (b) Comparison of the mean percentage deviation,  $\langle \text{dev} \rangle$ , between the solar-abundance and  $\alpha$ -MILES synthetic spectra produced by STARLIGHT for a subsample of 1,000 ETGs in the SPIDER (see the text). The percentage deviation decreases by a factor of  $\sim 2$  when using the  $\alpha$ -enhanced models.

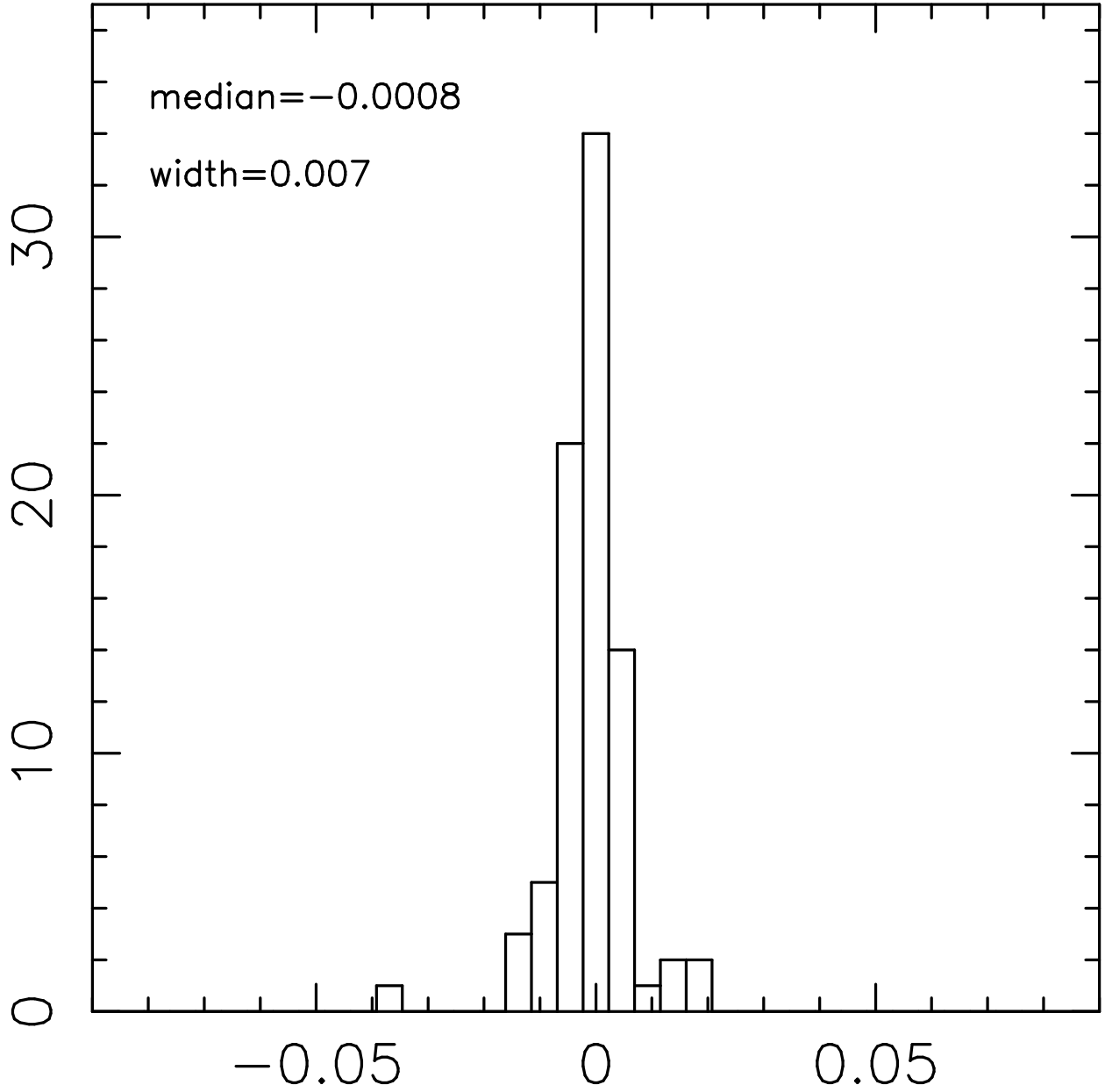


Fig. 25.— Comparison of solar MILES models with  $\alpha$ -MILES models having solar abundance ratio ( $[\alpha/Fe] = 0$ ). The Figure plots the distribution of luminosity-weighted  $[\alpha/Fe]$ , obtained by running STARLIGHT on SSP models from the solar MILES library, with a variety of ages and metallicities (see the text). The central and width values of the distribution are reported in the upper-left corner of the plot. Notice how the distribution is narrowly peaked around zero, proving the consistency of both sets of models for  $[\alpha/Fe] = 0$ .

for the optical+NIR sample of ETGs. Red and black colors correspond to r- and K-band effective radii. As expected, some correlations exist between the  $R_e$  and the spectroscopic parameters. In particular, the effective radius increases in galaxies with larger metallicity and  $\alpha$ -enhancement. However, one can notice that the range of variation in  $R_e$  amounts to only 0.1 – 0.2 dex, i.e. much smaller than the range of  $\sim 1.5$  dex spanned by the optical and NIR effective radii (see Panel a of Fig. 11). In the case of  $[\alpha/Fe]$  (Panel d of Fig. 26), the optical  $R_e$  changes from  $\sim 0.55$  dex at  $[\alpha/Fe] \sim 0$  to  $\sim 0.7$  dex at  $[\alpha/Fe] \sim 0.26$ . From Fig. 11, we see that the corresponding variation of  $\nabla_\star$  is completely negligible, implying that the aperture effect is not affecting at all the correlations exhibited in Fig. 15.

### C. Derivatives of SSP magnitudes with respect to age and metallicity

We describe here how the colors available for the SPIDER sample can be parametrized in terms of age and metallicity of stellar population models. We adopt the Bruzual & Charlot (2003) (BC03) models.

Fig. 27 exhibits the magnitudes of a simple stellar population model, normalized to a total mass of one solar mass in stars, as a function of its age,  $t$ , for the *grizYJHK* wavebands of the SPIDER dataset. The *griz* and *YJHK* magnitudes are given in the AB and Vega systems, respectively. In order to describe the colors of ETGs, we consider relatively old ages, spanning the range of 5 to 13.5 Gyrs. Different metallicities are also displayed in the range of 0.2 to 2.5 times solar ( $Z_\odot$ ). Fluxes are computed with the BC03 code, convolving the SDSS and UKIDSS throughput curves with the model SEDs. In the optical passbands, the magnitude is essentially a linear function of  $\log t$ . This is consistent with the fact that the flux of a simple stellar population is expected to change as  $t^{-\alpha}$ , where  $\alpha$  depends on the metallicity of the stellar population and the slope of the IMF (Tinsley 1973). In the NIR passbands, the power-law approximation is less accurate, particularly at the lower age end. In order to calculate the color derivatives with respect to age and metallicity, for each waveband we fitted the corresponding magnitudes with a two-dimensional polynomial in  $\log t$  and  $\log Z$ . As shown in Fig. 27, a polynomial of degree eight reproduces model magnitudes very accurately. The rms of the fits are smaller than 0.01 mag in all the bands. Estimating fluxes using a composite stellar population with exponential star formation rate (SFR) and an e-folding time of 1 Gyr as a function of age and metallicity provides essentially similar results. Given the polynomial coefficients for each band, the computation of the color's derivatives is straightforward for any combination of  $t$  and  $Z$ .

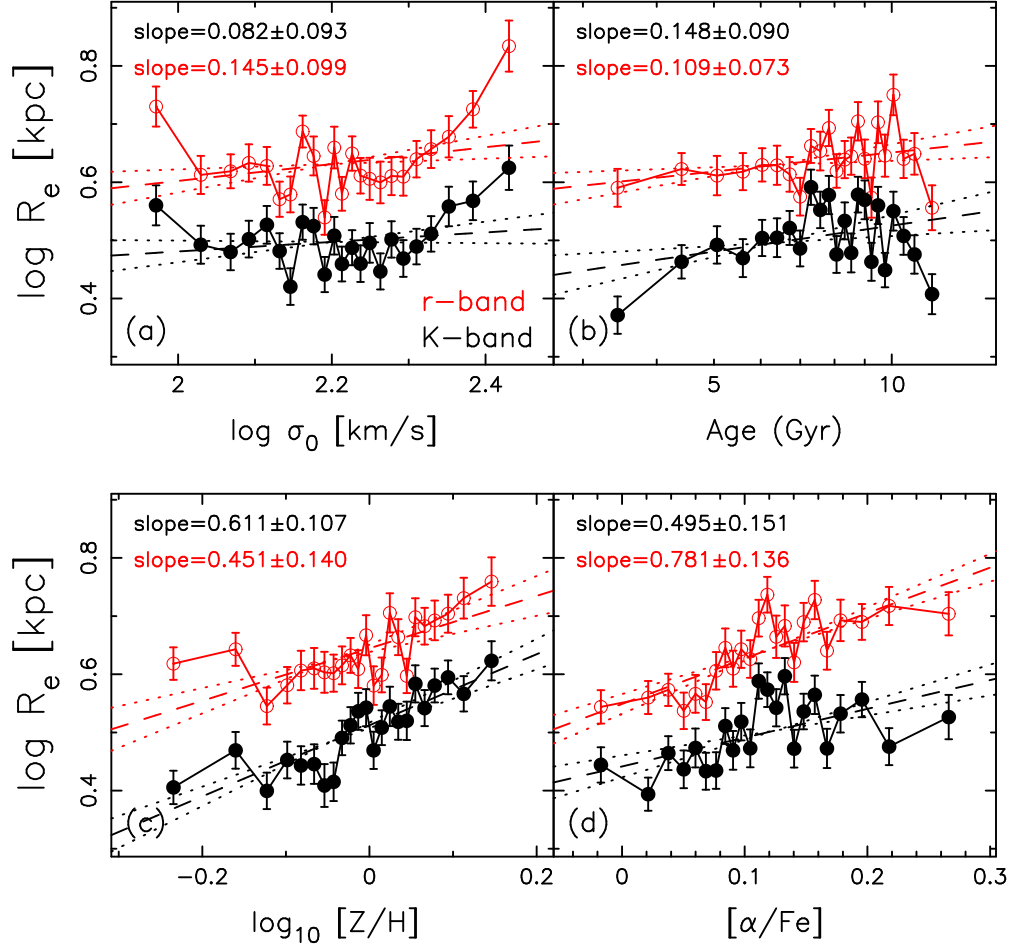


Fig. 26.— Logarithmic median effective radius as a function of central velocity dispersion (Panel a), age (Panel b), metallicity (Panel c), and  $\alpha$ -enhancement (Panel d). Black and red colors refer to  $K$ - and  $r$ -band effective radii. Error bars denote  $1\sigma$  standard error on the medians. Each trend is modeled by a linear fit, shown as a dashed line. The dotted lines mark the  $\pm 1\sigma$  uncertainties on the fitted lines. The slopes of the fits and the corresponding  $1\sigma$  uncertainties are reported in the left-upper corner of each panel.

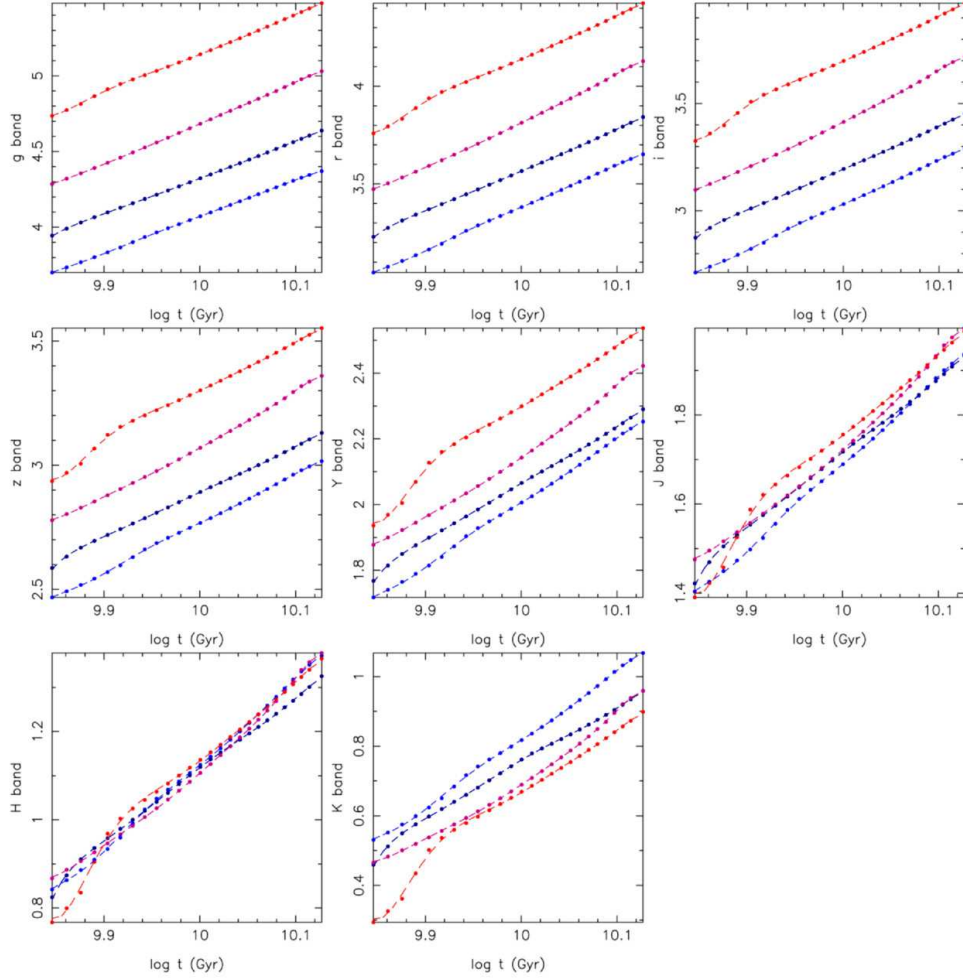


Fig. 27.— Magnitudes of simple stellar population models from BC03 as a function of their formation epoch,  $t$ . The models are normalized to a total mass of  $1 M_{\odot}$  (one solar mass) in stars. The griz and YJHK magnitudes are computed in the AB and Vega systems, i.e. the photometric systems of SDSS and UKIDSS, respectively (see Paper I). Different colors denote different metallicities. The color become bluer from higher to lower metallicity. Four metallicities are plotted:  $Z = 0.2, 0.4, 1.0, 2.5 Z_{\odot}$ . Dashed lines show the result of fitting magnitudes as a function of age and metallicity with two-dimensional polynomials of degree eight.

#### D. Possible sources of bias in the $\nabla$ 's.

The existence of radial gradients of absorption indices in ETG's spectra (e.g.  $Mgb$  and  $H_\beta$ ) implies that internal color gradients are likely driven by a variation of age and metallicity inside galaxies, consistent with our assumption in Eq. 12. However, as argued by Silva & Wise (1996) and Wise & Silva (1996), radial gradients in internal reddening might also contribute significantly to the observed color gradients. In such case, one would naturally expect a correlation to exist between the gradient and the amount of dust, with stronger gradients in more dust-obscured galaxies. Although a detailed analysis of the dust distribution in ETGs is certainly beyond the scope of the present paper, we can evaluate if internal reddening might affect significantly our findings on the correlation among gradients and stellar population properties (Sec. 9). As a rough estimate of the *total* amount of internal reddening, we use the color excess,  $E(B - V)$ , obtained for each galaxy by the SED fitting procedure (Sec. 8). Fig. 28 plots the median  $\nabla_\star$  for the different  $E(B - V)$  (see Tab. 1). A clear correlation is detected, in the sense that steeper gradients are found at higher extinctions. The trend is mostly because of galaxies at high  $E(B - V)$  ( $\geq 0.3$ ), with these objects amounting to less than 10% of the entire ETG's sample. We conclude that internal reddening might contribute significantly to color gradients only for a minor fraction of galaxies. Also, we find that selecting galaxies with  $E(B - V) \leq 0.2$ , for which the variation of color gradients with internal reddening is insignificant, does not change at all the trends shown in Fig. 17.

Another possible source of concern is that color derivatives in Eq. 12 are estimated by stellar population models reshifted at the median redshift,  $z = 0.0725$ , of the SPIDER sample, hence neglecting the effect of  $k$  and evolutionary corrections on color gradients. In order to see if this approximation impacts our results, we select only ETGs from the optical+NIR sample in a narrower redshift range of  $z = 0.0625$  to  $0.0825$ , leading to a subsample of 1,984 galaxies. For this subsample, the peaks of the  $\nabla_\star$ ,  $\nabla_i$ , and  $\nabla_Z$  distributions amount to about  $-0.31$ ,  $0.126$ , and  $-0.43$ , respectively, fully consistent with that obtained for the entire sample (see Tab. 2). Also, the trends shown in Fig. 17 turned out not to be affected by this selection.

We would like to thank the anonymous referee for his/her constructive report, which definitely helped improving parts of this paper. We thank the staffs in charge of the cluster computers at the INPE-LAC (Sao José dos Campos, Brazil), H.C. Velho, and the staffs at INAF-OAC (Naples, Italy), Dr. A.Grado and F.I.Getman, for keep running the systems smoothly. We have used data from the 4th data release of the UKIDSS survey, which is described in detail in Warren et al. (2007). The UKIDSS project is defined in Lawrence et al. (2007). UKIDSS uses the UKIRT Wide Field Camera (WFCAM; Casali et al, 2007). The photometric system is described in Hewett et al (2006), and the calibration is described in Hodgkin et al. (2009). The pipeline processing and science archive are described in Irwin et al (2009, in prep) and Hambly et al (2008). UKIDSS data have been an-

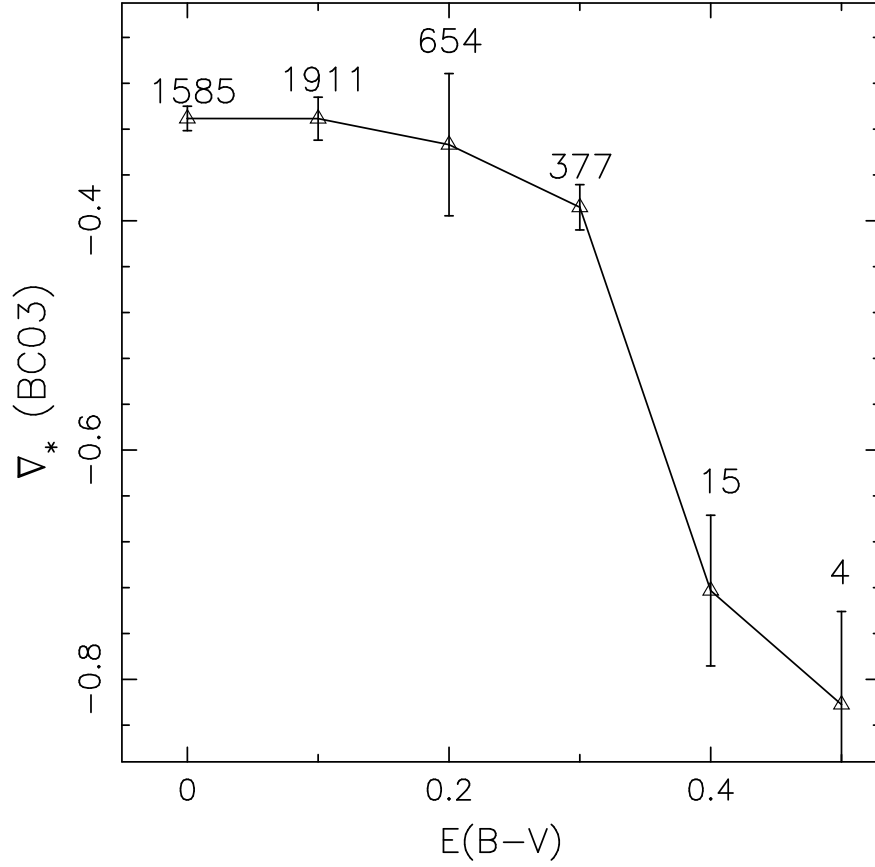


Fig. 28.— Medians of the effective color gradient,  $\nabla_*$ , as a function of the amount of reddening,  $E(B - V)$ , in ETGs. The plot is obtained for the optical+NIR sample of ETGs. Error bars denote  $1 \sigma$  uncertainties on median values. The numbers of ETGs for different  $E(B - V)$  are reported above the corresponding error bars in the plot. Most of the galaxies (91%) have  $E(B - V) \leq 0.2$ , for which the variation of  $\nabla_*$  with color excess is smaller than  $\sim 0.02$ .

alyzed using the Beowulf system at INAF-OAC (Cascone et al. 2002). Funding for the SDSS and SDSS-II has been provided by the Alfred P. Sloan Foundation, the Participating Institutions, the National Science Foundation, the U.S. Department of Energy, the National Aeronautics and Space Administration, the Japanese Monbukagakusho, the Max Planck Society, and the Higher Education Funding Council for England. The SDSS Web Site is <http://www.sdss.org/>. The SDSS is managed by the Astrophysical Research Consortium for the Participating Institutions. The Participating Institutions are the American Museum of Natural History, Astrophysical Institute Potsdam, University of Basel, University of Cambridge, Case Western Reserve University, University of Chicago, Drexel University, Fermilab, the Institute for Advanced Study, the Japan Participation Group, Johns Hopkins University, the Joint Institute for Nuclear Astrophysics, the Kavli Institute for Particle Astrophysics and Cosmology, the Korean Scientist Group, the Chinese Academy of Sciences (LAMOST), Los Alamos National Laboratory, the Max-Planck-Institute for Astronomy (MPIA), the Max-Planck-Institute for Astrophysics (MPA), New Mexico State University, Ohio State University, University of Pittsburgh, University of Portsmouth, Princeton University, the United States Naval Observatory, and the University of Washington.

## REFERENCES

- Adelman-McCarthy, J. K., et al. 2008, *ApJS*, 175, 297
- Balcells, M., & Peletier, R.F. 1994, *AJ*, 107, 135
- Beers, T.C., Flynn, K., Gebhardt, K. 1990, *AJ*, 100, 32
- Bell, E. F., McIntosh, D. H., Katz, N., Weinberg, M. D. 2003, *ApJS*, 149, 289
- Bernardi, M., Sheth, R.K., Annis, J. 2003a, *AJ*, 125, 1849
- Blanton, M.R., Lin, H., Lupton, R.H., Maley, F.M., Young, N., Zehavi, I., Loveday, J. 2003, *AJ*, 125, 2276
- Brinchmann, J., & Ellis, R. S. 2000, *ApJL*, 536, L77
- Bruzual, G., & Charlot, S. 2003, *MNRAS*, 344, 1000 (BC03)
- Bundy, K., Ellis, R. S., & Conselice, C. J. 2005, *ApJ*, 625, 621
- Calzetti, D., Armus, L., Bohlin, R. C., Kinney, A. L., Koornneef, J., & Storchi-Bergmann, T. 2000, *ApJ*, 533, 682
- Cantiello, M. et al. 2005, *ApJ*, 634, 239



- Caon, N., Capaccioli, M., & D’Onofrio, M. 1993, MNRAS, 265, 1013
- Casali, M., Adamson, A., Alves de Oliveira, C., et al. 2007, A&A, 467, 777
- Cascone, E., Grado, A., Pavlov, M., Capasso, G. 2002, SPIE, 4848, 328
- Cervantes, J.L., Coelho, P., Barbuy, B., and Vazdekis, A. 2007, Proceedings IAU Symposium No. 241 ‘Stellar Populations as Building Blocks of Galaxies’, A. Vazdekis and R.F. Peletier, eds, 167
- Chabrier, G. 2003, PASP, 115, 763
- Choi, Y.Y., Park, C., Vogeley, M.S. 2007, ApJ, 658, 884
- Cid Fernandes, R., González Delgado, R.M., Storch-Bergmann, T., Martins, L.P., Schmitt, H. 2005, MNRAS, 356, 270
- Clemens, M.S., et al. 2009, MNRAS, 392, 35
- Coelho, P., Barbuy, B., Melendez, J., Schiavon, R.P., and Castilho, B.V. 2005, A&A, 443, 735
- Cole, S., et al. 2001, MNRAS, 326, 255
- Coppola, G., La Barbera, F., Capaccioli, M. 2009, PASP, 121, 437
- Cowie, L.L., Songaila, A., Hu, E.M., Cohen, J.G. 1996, AJ, 112, 839
- De Lucia, G., Springel, V., White, S.D.M., Croton, D., Kauffmann, G. 2006, MNRAS, 366, 499
- de Propris, R., et al. 2005, MNRAS, 357, 590
- D’Onofrio, M., et al. 2008, ApJ, 685, 875
- Ferreras, I., et al. 2005, ApJ, 635, 243
- Ferreras, I., et al. 2009, ApJ, 635, 243
- Gallazzi, A., et al. 2006, MNRAS, 370, 1106
- Gómez, P.L., Nichol, R.C., Miller, C.J., et al. 2003, ApJ, 584, 210
- Gonzalez, J.J. 1993, Ph.D. thesis, Univ. California
- Goudfrooij, P. et al. 1994, A&AS, 104, 179
- Goudfrooij, P. & de Jong, T. 1995, A&AS, 298, 784

- Graves, G.J., Faber, S.M., & Schiavon, R.P. 2009, *ApJ*, 698, 1590
- Hambly, N.C., Collins, R.S., Cross, N.J.G., et al. 2008, *MNRAS*, 384, 637
- Hewett, P.C., Warren, S.J., Leggett, S.K., Hodgkin, S.T. 2006, *MNRAS*, 367, 454
- Hogg, D.W., Blanton, M.R., Brinchmann, J., et al. 2004, *ApJ*, 601, 29
- Ilbert, O., et al. 2009, *ApJ*, 690, 1236
- Jørgensen, I., Franx, M., & Kjaergaard, P. 1996, *MNRAS*, 280, 167
- Jørgensen, I. 1999, *MNRAS*, 306, 607
- Kauffmann, G., & Charlot, S. 1998, *MNRAS*, 297, L23
- Kobayashi, C. 2004, *MNRAS*, 347, 740
- Kuntschner, H., Smith, R.J., Colless, M., Davies, R.L., Kaldare, R., Vazdekis, A. 2002, *MNRAS*, 337, 172
- La Barbera, F., et al. 2003, *A&A*, 409, 21
- La Barbera, F., de Carvalho, R.R., Gal, R.R., Busarello, G., Merluzzi, P., Capaccioli, M., Djorgovski, S.G. 2005, *ApJ*, 626, 19
- La Barbera, F., et al. 2008, *PASP*, 120, 681
- La Barbera, F., Busarello, G., Merluzzi, P., de la Rosa, I.G., Coppola, G., Haines, C.P. 2008, *ApJ*, 689, 913
- La Barbera, F., & de Carvalho, R.R. 2009, *ApJ*, 699, 76L
- La Barbera, F., de Carvalho, R.R., de la Rosa, I.G., Lopes, P.A.A., Kohl-Moreira, J.L., Capelato, H.V. 2010, *MNRAS*, in press (*arXiv0912.4547L*; Paper I)
- La Barbera, F., de Carvalho, R.R., de la Rosa, I.G., Lopes, P.A.A. 2010, *MNRAS*, in press (*arXiv0912.4558L*; Paper II)
- Lawrence, A., Warren, S.J., Almaini, O., et al. 2007, *MNRAS*, 379, 1599
- Maraston, C. 2005, *MNRAS*, 362 799 (M05)
- Marigo, P., & Girardi, L. 2007, *A&A*, 469, 239
- Menanteau, F., et al. 2001, *MNRAS*, 322, 1

- Mehlert, D. et al. 2000, A&AS, 141, 449
- Menanteau, F., et al. 2004, ApJ, 612, 202
- Michard, R. 1999, A&A, 137, 245
- Nelan, J.E., et al. 2005, ApJ, 632, 137
- Peletier, R.F. et al. 1990, A&A, 233, 62
- Poggianti, B.M., Bridges, T.J., Mobasher, B., et al. 2001, ApJ, 562, 689
- Poggianti, B.M., Bridges, T.J., Carter, D., et al. 2001, ApJ, 563, 118
- Roche, N., Bernardi, M., Hyde, J. 2010, MNRAS, submitted (arXiv:0911.0044)
- Saglia, R.P., et al. 2000, A&A, 360, 911
- Salim, S., et al. 2005, ApJL, 619, L39
- Salim, S., et al. 2007, ApJS, 173, 267
- Schlegel, D., Finkbeiner, D.P., & Davis, M. 1998, ApJ, 500, 525 (SFD98)
- Silva, D.R., & Wise, M.W. 1996, ApJ, 457, 15
- Sorrentino, G., Antonuccio-Delogu, & V., Rifatto, A. 2006, A&A, 460, 673
- Suh, H. et al. 2010, ApJS, 187, 374
- Tamura, N., Kobayashi, C., Arimoto, N., Kodama, T., Ohta, K. 2000, AJ, 119, 2134
- Tamura, N., Ohta, K. 2000, AJ, 120, 533
- Tamura, N., Ohta, K. 2003, AJ, 126, 596
- Tamura, N., Ohta, K. 2004, MNRAS, 355, 617
- Terlevich, A.I., Forbes, D.A. 2002, MNRAS, 330, 547
- Thomas, D., et al. 2005, ApJ, 621, 673
- Tinsley, B.M. 1973, ApJ 186, 35
- Tortora, C., Napolitano, N.R., Cardone, V.F., Capaccioli, M., Jetzer, P., Molinaro, R. 2010, MNRAS, in press (arXiv1004.4896T)

- Trager, S.C., Faber, S.M., Worthey, G., González, J.J. 2000, *AJ*, 120, 165
- Treu, T., Stiavelli, M., Casertano, S., Møller, P., Bertin, G. 1999, *MNRAS*, 308, 1037
- van Dokkum, P.G., Stanford, S.A. 2003, *ApJ*, 585, 78
- Vazdekis, A., Sánchez-Blázquez, P., Falcón-Barroso, J., et al. 2010, *MNRAS*, 404, 1639
- Warren, S.J., Hambly, N.C., Dye, S., et al. 2007, *MNRAS*, 375, 213
- White, S.D.M. 1980, *MNRAS*, 191, 1
- Wise, M.W., & Silva, D.R. 1996, *ApJ*, 461, 155
- Worthey, G., Trager, S.C., Faber, S.M. 1995, *ASPC*, 86, 203
- Wu, H., et al. 2005, *ApJ*, 622, 244